/
Article / Book Information

( )	
Title(English)	Study on probing technique for dielectric measurement at millimeter-wave frequencies
( )	
Author(English)	Ryo Sakamaki
( )	: ( ), : , : 11327 , :2019 9 20 , : , : , , , ,
Citation(English)	Degree:Doctor (Academic), Conferring organization: Tokyo Institute of Technology, Report number: 11327 , Conferred date:2019/9/20, Degree Type:Course doctor, Examiner:,,,,,
( )	
Type(English)	Doctoral Thesis

ミリ波帯における 誘電体材料評価技術の研究

Study on probing technique for dielectric measurement at millimeter-wave frequencies

（東京工業大学大学院博士課程論文）

学　　　院	：	物質理工学院
系	：	材料
研　究　生	：	坂　巻　亮
指　導　教　官	：	鶴　見　敬　章
		武　田　博　明

二〇一九年八月

Abstract

This study proposes a precision probing technique and a dielectric measurement method at millimeter-wave (mmW) frequencies up to 300 GHz. The proposed probing technique analyzes measured electrical signal to determine position of a radio-frequency probe automatically without using microscope observation. Thus, the probing technique improve repeatability in the probe position because it can avoid impacts of a resolution of microscope and operator's art-of-measurement. Further, the proposed dielectric measurement method generates a resonator in a transmission line by contacting the probe in the middle of the transmission line. The dielectric measurement method has two of unique features. One is that, the method doesn't require to prepare any resonator before the measurement because the resonator used for the measurement is generated in the transmission line on site. Second, accuracy in size of the resonator is determined by accuracy of probe positioning, which is generally finer than working accuracy of conventional resonators. These features allow the measurement adopted even in the frequency range up to 300 GHz. Further, the method can realize "in-situ" dielectric permittivity measurement, which is expected as a practical testing technology for a planar-circuit on inhomogeneous substrate.

The use of the mmW frequencies for novel communication technologies, and problems of present dielectric measurement techniques are described in Chapter 1. Chapter 2 presents the precision probing technique to reduce the variation of probe position. The probing technique can proceed fully automatically without direct observation by an operator. The probe positioning accuracy was improved to 1 μm by using the proposed precision probing technique. Chapter 3 demonstrates universality of the probing technique. The probing technique was demonstrated with transmission lines and an attenuator in the frequency range up to 340 GHz. Measurement repeatability of on-wafer S-parameter measurement was greatly improved by using the proposed probing technique for all of the devices. Chapter 4 demonstrates the new dielectric measurement method in the frequencies range up to 300 GHz. Evaluated dielectric permittivity and loss tangent were corresponded to dielectric dispersion calculated by a conventional phonon model of alumina. Chapter 5 demonstrates in-situ effective permittivity measurement by using a transmission line and an attenuator device, which do not include any resonator components. The evaluation results were corresponded each other. This result indicates that the technique can evaluated inhomogeneity

of substrate material just below actual RF devices. The proposed dielectric measurement method is expected to be used in actual circuit testing processes for circuit fabricators. Chapter 6 describes contributions of the study for human societies and academic knowledges. This study treated knowledges of device engineering to solve the problems of material science. The study bridges research fields between material science and device engineering. The combination of academic fields originates new research themes and improve efficiency in development of industrial products. The proposed dielectric measurement method can address the problem in others novel dielectric measurement methods. Thus, it is expected as a powerful tool for development of "Beyond 5G" communication technologies.

概要

　　本研究では、300 GHz に至るミリ波帯で利用可能な高精度なプローブ制御技術と、それを応用した新しい誘電体材料の評価技術を開発した。開発したプローブ制御技術は、従来技術の顕微手法と異なり、実際に測定される電気信号を解析することで、プローブ位置を自動的に決定することができる。そのため、顕微鏡の解像度や作業者依存性といった外乱要因を避けることができるため、プローブ位置の再現性を高めることができる。また、開発した誘電体材料の評価技術では、高周波プローブを伝送線路の中ほどに接触させることにより、その場で共振を発生させる事で材料評価を行なう。開発した評価技術は 2 つの大きな特徴がある。1 つはその場で共振を発生させるため、事前に共振器を準備する必要がない事である。もう 1 つは、共振器の寸法精度はプローブの位置制御精度で決まる事である。前者はその場材料計測技術を実現するものであり、実用デバイスの検査技術として応用可能である。後者は、従来の共振法では共振器の寸法精度の限界から困難であった、300 GHz に至るミリ波帯での材料評価を実現させる事ができる。

　　第 1 章では、先端通信技術におけるミリ波帯の利用状況と、従来の材料評価技術の問題点ついて述べる。特に 100〜300 GHz 付近の次世代通信技術の開発が始まっているが、その帯域における適切な低損失材料の評価手法が存在しない事が課題である。そこで、本研究では当該帯域で利用できる高周波プローブを利用した新しいデバイスの評価技術と誘電体材料の評価手法を提案する。

　　まず、第 2 章では、プローブの接触位置を高精度の制御する技術を開発した。従来技術では目視及び手動でプローブの接触位置を決定するため、その位置決め精度は 10 μm 程度であった。開発した制御技術では、測定される電気信号を解析することでプローブ位置を決定する。そのため、顕微鏡の解像度の影響や作業者依存性を避けることができ、1 μm 精度でプローブの接触位置を制御する事ができる。

　　次に、第 3 章では第 2 章で開発した高精度プローブ制御技術をサブミリ波に至る周波数帯での適用性や、スクリーン印刷によって作成した金属配線といった特殊なデバイスに対する適用性について検証を行なった。その結果、それらの周波数やデバイスといった条件下でも、プローブ制御技術は利用可能であることを明らかにした。以降の第 4 章から第 6 章では、この高精度なプローブ制御技術を応用した技術を開発した。

　　第 4 章では、開発したプローブの制御技術を用いた誘電体材料の評価を実証した。開発したプローブ位置の制御技術を用いることによって、測定再現性が大幅に向上し、平衡平板型共振器法といった従来手法と比較して十分な信頼性を確保することができた。さらに、測定精度の評価も行なうことで、開発した技

術の測定能力を明らかにした。さらに測定精度は描いた電極の寸法とその精度に強く依存する事を明らかにした。開発した誘電特性の評価技術を用いて、高周波デバイスの基板材料として広く利用されるアルミナの評価を行なったところ、従来のフォノンによる誘電分散モデルで得られた誘電特性と、測定精度の範囲内で一致する結果を得ることができた。これにより、開発した材料評価手法の妥当性を実証することができた。

　　第5章では開発した材料評価法による、実用的な高周波デバイスを用いた、『その場』実効比誘電率の評価を実証した。共振器の構造を有さない整合した伝送線路と減衰器を用いて実効誘電率の評価を行なったところ、双方の測定結果は一致した。この結果から、開発した材料評価手法が実用デバイスの実効誘電率の評価手法としても有効であることを実証した。

　　第 6 章では本研究の社会及び学問における位置づけについて述べる。本研究は材料工学の課題に対してデバイス工学の知見を用いて取り組んだ。そのため、双方の学問を橋渡しする研究である事を示した。また、橋渡しを行なうことで、新しい研究課題を創出や産業におけるデバイス開発速度の促進など、産業及び学問に対して寄与できる事を示した。本研究で開発した開発したプローブ位置の制御技術と誘電体材料の評価技術は、昨今議論が開始された次世代通信技術で利用されるデバイスや材料の評価法として有効であり、産業社会への波及効果も期待する事ができる。

Contents

Chapter 1   Introduction

1.1   Communication technologies and transformation of substrate material

1.1.1   Use of millimeter-wave frequencies

Communication technologies, such as broadcasting and mobile communications, have become essential for modern-day society. Fourth generation (4G) communication technology, which includes Long Term Evolution (LTE), uses several frequency bands with the frequencies ranging from 0.45 GHz to 3.6 GHz. The frequency band in the range of 0.3 GHz – 3 GHz is generally called the "platinum band" because of the favorable propagation characteristics for commercial wireless communications. In addition, unlicensed use of the frequency band in the range of 3.1 – 10.6 GHz is approved for high speed communications in limited personal space [1,2]. However, as shown in Figure 1.1, the frequency resource in the microwave frequency band has been practically exhausted, because this frequency range is already occupied by various communication objectives. Furthermore, not only exhaustion of the frequency resource, but also high-speed communication requires the use of higher microwave and millimeter-wave (mmW) frequencies, which are ranged from 10 GHz to 300 GHz [3]. For example, WiGig, which is the high-speed and short-range wireless communication technology, uses the frequency of 60 GHz. Automotive radars use the frequency of 76 GHz.

Recently, fifth-generation (5G) communication has particularly attracted attention in the electrical communication research field [2]. 5G communication uses the frequency band in the range of 3.7 GHz – 28 GHz. With the increase of frequency, free-space loss and straightness of electrical wave lead to the degradation of the communication quality.

Various techniques have been developed for 5G communication, including massive multiple-input multiple-output (MIMO), distributed base station, and beam-forming [4]. Massive MIMO systems use antenna arrays with a few hundred antennas to compensate the free-space loss. Then, the radiated energy is focused into small regions in space by using coherent superposition of the waves emitted from the array antennas. These techniques are known as "beam-forming." Massive MIMO technology has significantly changed the requirements for the communication devices. Distributed antennas in massive MIMO systems allow using smaller and less powerful amplifiers; however, the antennas should be highly integrated. Linear 50-W amplifiers are generally used in conventional antenna systems. These amplifiers can be replaced by inexpensive amplifiers with the output power in the mW range. On the other hand, additional base stations are required to avoid the influence of non-transparent obstructions. Therefore, power efficient and integrated antenna systems are strongly required for the 5G communication.

International standardization of the 5G communication technology is accelerating toward the actualization in 2020. At the same time, some research communities start discussing "beyond-5G" communication technologies [5], which will employ 140-GHz, 240-GHz, and 340-GHz bands [6]. Recently, several studies have demonstrated radio frequency (RF) components that operate in the frequency range of $100 - 340$ GHz [7-10]. Thus, device design techniques for the mmW-frequency band are essential for the development of accurate and reliable devices. Figure 1.2 shows a schematic illustration of the electronic device development process. First, the specification of a target device is drawn up. Then, the circuit structure is designed to satisfy the specification. Next, the designed prototype is fabricated and evaluated. The obtained data is analyzed to find defects and transmit the obtained information back to the circuit design. Then, the procedure is repeated until the target device meets the specifications. As will be described

in section 1.2.1, the complexity of circuit design increases with the increase of the operating frequency; therefore, it is hard to acquire the desired device properties in a single trial. Thus, the accurate evaluation and analysis techniques that allow to identify design and production flaws are essential, especially at mmW frequencies [11]. Therefore, the study discusses the evaluation and analysis techniques at the mmW frequencies.

Coaxial lines and rectangular waveguides are generally used as transmission lines to connect the telecommunication facilities. However, improvements in the communication technology require miniaturization of RF devices. Therefore, planar circuits, such as microstrip waveguides (MSTL) and co-planer waveguides (CPW), can be used as the alternatives of coaxial lines and rectangular waveguides [12]. Thus, the use of planar circuits at the mmW frequencies is one of the trends in this research field.

1.1.2 Demand for planar circuits and ceramics substrate

Figure 1.3 shows the cross sections of different planar circuits. The dashed lines in the figure represent electric field. These planar circuits consist of the conductive metal layer on a dielectric substrate. Dimensions of the conductor are designed to achieve the target characteristic impedance by using equations in section 1.2.1. Table 1.1 lists the representative substrate materials and their properties.

Table 1.1   Representative substrate materials and their properties [12]

Material	ε_r	$\tan\delta$
Al_2O_3	9.8	0.0001
Sapphire	9.4	0.0001
Quartz glass	3.78	0.0001
BeO	6.3	0.006
TiO_2	85	0.004
BaT_4O_9	37	0.0005
Zirkonate	20-40	0.0002
GaAs	12.9	0.002
Si	11.9	0.015

Ferrite	9-16	0.001
PTFE	2.1	0.0003
Polyolefin	2.32	0.0007

Ceramic materials not only have higher strength and heat tolerance, but also exhibit lower dielectric loss than other materials. Thus, ceramic materials are used for high-reliability circuits. As was described in the previous section, power-efficient systems are strongly required for the "beyond 5G" technology. Ceramics are expected to be a good candidate because of their low dielectric loss, which is important for power-efficient systems. Furthermore, higher operating frequencies require finer fabrication of metallization to reduce reflection and loss of a circuit. Lithography is one of the precision fabrication techniques for conductive metallization. However, organic materials cannot be used for the lithography process, because the substrate has to be heated to approximately 400 ℃ in the fabrication process. Thus, ceramic substrates are increasingly used at the mmW frequencies. Impedance Standard Substrates (ISS), which requires high reliability and stability to provide reference impedance in on-wafer measurements, generally use Al_2O_3 as a substrate material [13]. National Institute of Standards and Technology, which administers the measurement standards in the United States, provides the reference impedance standard called "RM8130" for the frequencies up to 40 GHz. RM8130 employs quartz glass as the substrate material, which has significantly lower dielectric loss then Al_2O_3 [14-17]. On the other hand, the improvement of low-temperature co-fired ceramic (LTCC) technology allows its usage in RF products. LTCC technology can realize high-density high-precision three-dimensional circuits by sintering stacked green sheets with conductor circuits on the surface of the sheets. In conventional solid-state synthesis, ceramics typically require being heated to 1300 ℃ in the sintering process, which is higher than the melting points of general conductive metals. Therefore, only high melting point metals, such as W and Mo, can be used as the metallization on the stacked green sheets, despite those metals are

relatively poor conductors. LTCC technology successfully decreases the sintering temperature to less than 900 ℃ by employing ceramics-glass composite materials. Thus, highly-conductive metals, such as Ag and Cu, whose melting points are 1173 ℃ and 961 ℃, respectively, can be used as the conductors [18]. Therefore, LTCC technology is widely used in RF circuit fabrication in the mmW-frequency band, because it requires higher integration and better conductive properties [19-22]. For example, waveguide-to-microstrip transitions and antennas can be fabricated using LTCC technology [10].

Therefore, ceramic materials are expected to be widely used in mmW devices. Thus, the investigation of ceramics properties at the mmW frequencies is necessary to comply with the requirements of modern technology.

1.2   Importance of material characterization for circuit design

As was described in the previous section, device fabrication and evaluation processes suffer from the fabrication errors, such as inaccurate determination of circuit dimensions or dielectric properties. In this chapter, first, the circuit design theory is described. Then, the importance of dielectric measurements is discussed.

1.2.1   Traditional microwave theories for circuit design [12]

The fundamental theory of circuit design is described in this section. The wavelength of an electromagnetic (EM) signal shortens when the signal is transmitted in a dielectric material, because dielectric materials store the EM energy in their body. The EM wavelength can be expressed as shown in equation (1). As shown in Figure 1.3, various types of planar circuits have been established in the past. Triplate circuits can be used for Transverse Electric Magnetic (TEM) wave propagation; however, other circuits support quasi-TEM propagation because of the asymmetric structure in the cross-section of the circuits. In this study, MSTL and CPW circuits are examined. For

instance, the effective dielectric constant of a CPW circuit can be approximately estimated by equation (2), where ε_r is the dielectric constant of a substrate.

$$\lambda_e = \frac{\lambda_0}{\sqrt{\varepsilon_{eff}}} \tag{1}$$

$$\varepsilon_{eff} = \frac{\varepsilon_r + 1}{2} \tag{2}$$

By using these equations, optimal circuit design can be developed. For example, the length of a $\lambda/2$-resonator can be determined from these equations. However, the equation (2) is known to produce a certain level of error in an estimated value. Thus, more detailed analysis is sometimes required for the circuit design [23-29]. Dynamic and static analyses are often adopted in this case. Dynamic analysis is based on EM simulations, and static analysis is based on a simplified circuit modeling. In this study, the static analysis is mainly described to provide the understanding of the basic concepts of the dielectric measurements. In static analysis, assuming that the effective dielectric constant is 1, the capacitance per unit length (C_0) and its actual value (C') are estimated by conformal mapping method. Non-uniform dielectric properties in the cross-section are transformed to ideal parallel-plate model with some virtual domains in the conformal mapping, as shown in Figure 1.4. The ratio of the domain areas is defined by the filling factor $q_\varepsilon = b_\varepsilon/b$. The effective permittivity of the parallel plate capacitor is calculated as:

$$\varepsilon_{r,eff} = \frac{C'}{C_0} = \frac{C'_\varepsilon + C'_{air}}{C_0} = \frac{\left(\varepsilon_r \varepsilon_0 b_\varepsilon/a\right) + \left(\varepsilon_0 b_{air}/a\right)}{\left(\varepsilon_0 b/a\right)} \tag{3}$$

$$= 1 + \frac{\varepsilon_r b_\varepsilon}{b} - \frac{b_\varepsilon}{b} = 1 + q_\varepsilon \left(\varepsilon_r - 1\right) \tag{4}$$

where ε_r is the dielectric constant of the substrate, ε_0 is the permittivity of free space, and a is the thickness of the capacitor. The filling factor q_ε is calculated as:

$$q_\varepsilon = \left(\varepsilon_{r,eff} - 1\right)/\left(\varepsilon_r - 1\right) \tag{5}$$

The modified conformal mapping method adopts rectangular-domain modeling instead of a simple parallel-plate capacitor. The Wheeler and Schneider equations express the effective dielectric constant of a MSTL circuit by the modified conformal mapping method. According to the Schneider equation, the effective permittivity of MSTL is expressed as:

$$\varepsilon_{eff} = \frac{\varepsilon_r + 1}{2} + \frac{\varepsilon_r - 1}{2}F \tag{6}$$

$$F = \left\{1 + \left(10\,h/w\right)\right\}^{-0.5} \tag{7}$$

where h is the thickness of the dielectric substrate and w is the width of the conductor, as shown in Figure 1.5(a). Characteristic impedance of MSTL is expressed as:

$$Z_c = \frac{Z_0}{\sqrt{\varepsilon_{eff}}} \tag{8}$$

$$Z_0 = 30\ln\left[1 + \frac{4h}{W_0}\left\{\frac{8h}{W_0} + \sqrt{\left(\frac{8h}{W_0}\right)^2 + \pi^2}\right\}\right] \tag{9}$$

where W_0 is the effective width of the transmission line, assuming the thickness of the strip line is zero. W_0 is expressed as a sum of the actual width W and correction factor ΔW; t is the thickness of the conductor.

$$W_0 = W + \Delta W \tag{10}$$

$$\Delta W = \frac{t}{h}\ln\frac{4e}{\sqrt{\left(\frac{t}{h}\right)^2 + \frac{1}{\pi^2\left(\frac{W_0}{t} + 1.1\right)^2}}} \tag{11}$$

The effective dielectric permittivity of CPW (Figure 1.5(b)) is expressed as:

$$\varepsilon_{r,eff} = \frac{\varepsilon_r - 1}{2} \frac{K(k')}{K(k)} \frac{K(k_1)}{K(k_1')} \tag{12}$$

$$K(k) = \int_0^{\pi/2} \frac{1}{\sqrt{1 - k^2 \sin^2 \theta}} d\theta \tag{13}$$

$$k = \frac{W}{d} \tag{14}$$

$$k_1 = \frac{\sinh(\pi W / 4h)}{\sinh(\pi d / 4h)} \tag{15}$$

$$Z_c = \frac{Z_{c,0}}{\sqrt{\varepsilon_{r,eff}}} \tag{16}$$

$$k' = \sqrt{1 - k^2} \tag{17}$$

$$Z_{c,0} = \frac{\zeta_0}{4} \frac{K(k')}{K(k)} \tag{18}$$

$$\zeta_0 = \sqrt{\frac{\mu_0}{\varepsilon_0}} \tag{19}$$

where μ_0 is the permeability of vacuum and $K(x)$ represents the elliptic integral of the first kind. These expressions are often used for the circuit design. Generally, a circuit should be designed to match Z_c with 50 Ω or 75 Ω. Figure 1.6 shows the estimated characteristic impedance with varied circuit dimension. According to equations (12) and (17), ε_r is an important parameter to determine Z_c. Therefore, precise determination of ε_r is essential to match a circuit to the target impedance.

1.2.2　Present dielectric measurement techniques

Figure 1.7 shows the dielectric measurement methods and their applicable range of frequencies and dielectric losses [30]. An optimal measurement method should be selected with considering the measurement frequency range and estimated dielectric properties of

the material under test (MUT). The details of each dielectric measurement method are described below.

Parallel-plate capacitance method is widely used in the frequency range up to 10 MHz [31-33]. Figure 1.8 shows a schematic illustration of this measurement method. A pair of conductor layers are fabricated on MUT to form a parallel-plate capacitor. After the preparation, complex impedance of the capacitor is measured by an impedance analyzer. The measured impedance data can be analyzed by the equivalent circuit analysis. Various models are proposed for the analysis [34,35]. Debye model is one of the representative models for the analysis of dipole polarization [36,37]. Parallel plate capacitor technique is widely used for the evaluation of bulk and thin film dielectric materials [38,39]. Frequency response analyzer (FRA) are also used for measurements instead of impedance analyzers in the frequency range up to 1 kHz. FRA are often used to evaluate the chemical response of energy storage devices [40-44].

Resonator methods are widely used for the dielectric measurements of low-loss materials with dielectric loss less than 10^{-2}. Figure 1.9 shows schematic illustrations of the cavity resonator method [45-47]. This method requires a cavity for measurements. As the cavity can be treated as a waveguide, transverse electric (TE) or transverse magnetic (TM) modes can propagate in the cavity. The resonant frequency of the cavity is determined by its size. Quality factor (Q) of the resonance is influenced by resistivity of the surface of the cavity, not only a purely contribution of the resonance in the cavity. The unwanted contributions can be eliminated by comparing two measurements. First, the measurement without MUT is conducted as an unloaded condition. After that, the measurement with MUT is conducted as a loaded condition. Difference between the two measurements is calculated as described in Ref.45 to extract the complex dielectric permittivity. In the approximate description, the shift of the resonant frequency is related to the dielectric permittivity, and the change in the 3-dB bandwidth is related to the

dielectric loss. Not only cavities, but also split cylinders [48,49] and circular disks [50-52] are used as the resonators for the dielectric measurements.

Reflection and transmission (R/T) method can be used for high-loss ($\tan\delta > 10^{-2}$) dielectric measurements. Coaxial lines and waveguides are often used as the transmission lines [53-55]. Figure 1.10 schematically shows the R/T method. Complex dielectric permittivity can be analyzed from the reflection and transmission coefficients via the EM model of the measurement. However, MUT should be pelletized to be installed into a waveguide. Working inaccuracy causes the dominant impact on the measurement results. The free-space method also belongs to the R/T methods. Figure 1.11 shows an illustration of the free space method. A pair of antennas are used for this measurement. MUT is set in the middle between the antennas. The free space method can evaluate complex permittivity without any pelletization. This feature enables measurements even in the 300-GHz [56-58].

THz time-domain spectroscopy (TDS) is widely used for dielectric measurements in the THz range [59-64]. THz-TDS utilizes a coherent pulsed laser source for the measurements. Ti-sapphire laser source is typically used as the THz emitter (Figure 1.12). The bandwidth of the THz emitter is typically up to 5 THz. The laser beam is split by an optical divider. One of the beams serves as the incident signal to the MUT, and the other is the reference signal. The output signal is detected by an electrooptic (EO) crystal, such as a ZnTe crystal. The detected output signal is compared with the reference signal. Then, the attenuation and time shift of the incident signal at MUT can be extracted. Complex permittivity can be calculated via the reflective indexes.

Fourier transform infrared reflectometer (FT-IR) is commonly used for the dielectric measurements at optical frequencies. FT-IR utilizes non-coherent sources, which is different from the THz-TDS. FT-IR uses the magnitude of the output signal for the calculation of the dielectric permittivity using Kramers–Kronig relations [65].

Other various dielectric measurement techniques are presented in references [66-68].

1.3   Current problems with dielectric measurements

1.3.1   Absence of a dielectric measurement method at 300 GHz

The representative dielectric measurement techniques are described above. As this study focuses on dielectric measurements in the mmW frequencies, the FT-IR and parallel-capacitance methods are not applicable. Since the free-space method can be used only for high-loss materials, such as organic substrates, it cannot be applied for low-loss ceramic materials. On the other hand, the cavity and circular-disk resonator methods are applicable to the low-loss dielectric measurements. However, although these methods are expected to provide accurate measurements, the limitations due to resonator manufacturing and test fixture inaccuracies, which may reach several hundred microns, cause limitations of the measurement frequency range. Thus, they are still difficult to apply to higher mmW frequencies, such as 300 GHz. In this respect, ring resonator method has an advantage in the accuracy of the resonator dimensions, because such resonators can be fabricated by the lithography process, which is generally more accurate than mechanical working process [69-71]. The accurate evaluation of the dielectric loss can be realized by combining measurements with EM simulations. T-junction resonator can be also used instead of a ring resonator [72]. However, the measurement methods experience the following difficulties: first, the electrical length and width of a strip-line are longitudinally extended by a fringing field at the open end, and its impact cannot be neglected at the mmW frequencies; second, a smaller-sized ring resonator at the mmW frequencies generates the mutual inductance effect in the resonator itself [70,73]. Therefore, the ring resonator method also has difficulties in applying to the mmW frequencies.

Over the past year, several dielectric measurement techniques which are adopted in the frequency above 110 GHz have been proposed [74,75]. D. F. Williams reported

dielectric permittivity measurements in the frequency range up to 700 GHz by using on-wafer thru-reflect-line (TRL) calibration method [76]. Although the TRL calibration method was originally used for the calibration of vector network analyzer (VNA) systems, it can extract dielectric permittivity by an additional calculation process [77-86]. However, dielectric measurement by TRL calibration is not effective for low-loss dielectric because it belongs to R/T method. Further, the reference also states that poor measurement repeatability of on-wafer measurements impairs the reliability of the evaluated dielectric properties [87,88].

1.3.2   Impacts of inhomogeneity of material

Regarding material properties, inhomogeneous dielectric properties are harmful for the circuit quality. Electrical properties of a circuit become sensitive to a slight change in the dielectric properties of a substrate at the mmW frequencies. As was described in the previous section, progress in material fabrication technologies, such as LTCC, allowed the use of new materials for the higher integration of circuits. However, these circuit technologies require examination of the material inhomogeneity to find defects in the fabricated circuits. For instance, LTCC has a problem of homogeneity because of the diffusion of conductor metal in the sintering process [89]. Even though conventional dielectric measurement techniques, such as cavity resonator method, can be expected to provide accurate measurement, they cannot provide information about inhomogeneity because they assume the homogeneity of specimens. In this respect, the resonator method with planar circuits, such as stripline and ring resonators, can be used for investigating inhomogeneity because they can provide the dielectric property of a circuit substrate around the resonator fabricated on the substrate [22,69,72]. The length of a $\lambda/2$ resonator at 100 GHz is 1.5 mm; thus, the stripline resonator method can realize local dielectric measurement at a resolution of several millimeters. However, since the measurement

methods have the difficulties as described in the previous section 1.3.1, the conventional techniques cannot be applied for a circuit substrate with actual RF devices on it. Therefore, the dielectric properties of bulk ceramics in same lot production, but without any device on them, are unavoidably used as reference values for investigating actual RF devices. However, clear conclusions cannot be obtained in this case owing to the inhomogeneity of substrates. Thus, in-situ local dielectric measurement is highly required for the detailed investigation of defects in fabricated devices.

1.4 Theory of vector network analyzer calibration and measurement

1.4.1 Overview of vector network analyzer calibration [83−86]

Calibration of VNA system is the process extracting systematic error from measurement. Another words, the calibration is the process to compensate parasitic impedance of cable, test fixture, and VNA itself. This section describes briefly explanation about VNA calibration.

Figure 1.13 shows a schematic illustration of structure of 2-port VNA. RF signal is generated from a high frequency signal source, and transmitted through a switch and a directional coupler to an output port. The other port is also connected to a directional coupler, switch, and 50 Ω termination. Output port can be changed by turning the switch. The coupler is connected to a power meter. Therefore, power of incident wave and reflected wave can be separately measured. S-parameter can be calculated from the measured complex power. However, since the switch and the couplers have non-ideal coupling in actual measurement, S-parameter is difficult to be calculated without any error-correction. VNA measurement assumes error boxes to compensate systematic error of measurement system as shown in figure 1.14. The figure indicates 8 terms error model. The error boxes X and Y, which are 2×2 S-parameter matrix, are put at both side of the

DUT. The error boxes are expressed in the equations (1) and (2), where e_{ij} indicates the error term. The error term can be treated as S-parameter matrix of the error box.

$$X = \begin{bmatrix} e_{00} & e_{01} \\ e_{10} & e_{11} \end{bmatrix} \tag{1}$$

$$Y = \begin{bmatrix} e_{22} & e_{23} \\ e_{32} & e_{33} \end{bmatrix} \tag{2}$$

Generally, cascade matrix (*T*-parameter) is used for the calculation as shown in the equation (3).

$$\begin{bmatrix} T_{11} & T_{12} \\ T_{21} & T_{22} \end{bmatrix} = \frac{1}{S_{21}} \begin{bmatrix} S_{12}S_{21} - S_{11}S_{22} & S_{11} \\ -S_{22} & 1 \end{bmatrix} \tag{3}$$

Using the equation (3), each error box and is transformed as:

$$T_X = \frac{1}{e_{10}} \begin{bmatrix} e_{00}e_{11} - e_{01}e_{10} & e_{00} \\ -e_{11} & 1 \end{bmatrix} \tag{4}$$

$$T_Y = \frac{1}{e_{32}} \begin{bmatrix} e_{22}e_{33} - e_{23}e_{32} & e_{22} \\ -e_{33} & 1 \end{bmatrix} \tag{5}$$

According to figure 1.13, relation in incident waves are expressed as:

$$\begin{bmatrix} b_0 \\ a_0 \end{bmatrix} = T_X \begin{bmatrix} a_1 \\ b_1 \end{bmatrix} \tag{6}$$

$$\begin{bmatrix} a_1 \\ b_1 \end{bmatrix} = T_{DUT} \begin{bmatrix} b_2 \\ a_2 \end{bmatrix} \tag{7}$$

$$\begin{bmatrix} b_2 \\ a_2 \end{bmatrix} = T_Y \begin{bmatrix} a_3 \\ b_3 \end{bmatrix} \tag{8}$$

Substituting (7) and (8) to (6), then:

$$\begin{bmatrix} b_0 \\ a_0 \end{bmatrix} = T_X T_{DUT} T_Y \begin{bmatrix} a_3 \\ b_3 \end{bmatrix} \tag{9}$$

Thus, evaluated T-parameter T_M is expressed as:

$$T_M = T_X T_{DUT} T_Y = \frac{1}{e_{10}e_{32}} \begin{bmatrix} -\Delta x & e_{00} \\ -e_{11} & 1 \end{bmatrix} T_{DUT} \begin{bmatrix} -\Delta y & e_{22} \\ -e_{33} & 1 \end{bmatrix} \tag{10}$$

$$\Delta x = e_{00}e_{11} - e_{01}e_{10} \tag{11}$$

$$\Delta y = e_{22}e_{33} - e_{23}e_{32} \tag{12}$$

Thus, actual *T*-parameter of DUT (T_{DUT}) is expressed as:

$$T_{DUT} = T_X{}^{-1}T_M T_Y{}^{-1} = (e_{10}e_{32}) \begin{bmatrix} -\Delta x & e_{00} \\ -e_{11} & 1 \end{bmatrix}^{-1} T_M \begin{bmatrix} -\Delta y & e_{22} \\ -e_{33} & 1 \end{bmatrix}^{-1} \tag{13}$$

According to the equations (10) and (13), seven of the error terms, e_{00}、 e_{11}、 Δx、

e_{22}、 e_{33}、 Δy、 $e_{10}e_{32}$ should be solved to establish the error correction of measurement

system. It is therefore seven of S-parameter measurements are required for determination of the error terms. The process to determine the error terms is called as "calibration".

1.4.2 Thru-Reflect-Line calibration [77−86]

This section briefly describes the theory of TRL calibration. More detail information of the calibration is described in Supplemental "TRL calibration". TRL calibration uses three of standards for the measurement. Since four of measurements, S_{11}, S_{21}, S_{12}, and S_{22}, can be conducted with a single standard, totally 12 of measurements can be conducted with 3 of standards. Thus, some of the property of the standards are not necessary to be known. The 3 of standards are selected according to following rules in TRL calibration.

1)   4 of S-parameter are known.
2)   Reflection coefficients S_{11}, S_{22} need not to be known, but adequately large, and $S_{11}=S_{22}$.
3)   Reflection coefficients S_{11}, S_{22} are known.

In TRL calibration, each standard is assigned as 1) THRU, 2) REFLECT, and 3) LINE. Typically, a THRU standard is 1 ps transmission line, a REFLECT standard is open or short devices, and a LINE standard is also a transmission line, but its length is longer than a THRU standard. By using the equations in the Supplemental "TRL calibration", each error term can be calculated.

1.5   Recent studies on on-wafer measurement

1.5.1   Accuracy of on-wafer measurement

As described in the section 1.3.2, the ring or strip-line resonator methods are good tools to investigate on inhomogeneity of MUT in microwave frequencies. On-wafer measurement system is good candidate for evaluation of planar circuit. Figure 1.15 shows the image of a typical on-wafer measurement system, which is often used for the

evaluation of planar circuits. The measurement system consists of the VNA and RF probe. The probe tips contact the pad of the device to evaluate the S-parameters. Various probe models are commercialized with different geometries of a probe tip and connectors. Generally, a single RF probe has multiple probe tips, which are individually assigned as a signal tip or ground tip, and each of the tips simultaneously contacts the signal line or ground line of the CPW. Although ground-signal-ground (GSG) probes, which have the signal tip between the two ground tips, are often used for evaluation, signal-ground (SG) and ground-signal (GS) probes are also used for the evaluation of slot lines. In addition, ground-signal-ground-signal-ground (GSGSG) probes, which have two signal tips sandwiched between the ground tips, are also commercialized [90,91]. The probe position is manually controlled by a probe station. The probe station has a microscope to observe probe tips. An operator makes the probe touching a pad of the target device while observing the probe tip. However, highly degrees of freedom in determination of probe position cause highly operator dependence in on-wafer measurement [92,93]. Variation in probe position over 10 μm in worst case.

1.5.2　Present researches on on-wafer measurement

Accurate on-wafer measurement technique has been discussed in elsewhere. Some reports indicate that definition of the standards is one of the important factors for realization of accurate measurement. In analogy with coaxial system, deviations in Short-Open-Load-Thru (SOLT) standard definitions from the ideal values, such as deviation of load standard from 50 ohms, and poly-nominal frequency dependence of load inductance, are two of the error contributors in SOLT calibration. Accurate definition of standard has been studied by both of experimental and simulation approaches [94−96]. On the other hand, TRL calibration does not require any standard definitions because it based on self-calibration algorithm.　It is therefore the TRL calibration potentially realizes accurate

calibration. However, TRL calibration assumes symmetry in the structure of probes, the standards, and probe's contact condition. It is imaginably difficult to make contact condition of two probes, such as probe's contact position relative to a contact pad, being same in on-wafer measurement. As described in section 1.4.2, TRL calibration requires two of transmission lines with different lengths. Since TRL calibration requires an operator to change distance between two probes, it is more difficult to keep contact condition being same than others calibration method. Furthermore, on-wafer measurement has operator dependence because operator's habit gives strongly impact to probe contact position, because the probe position is determined by direct observation using a microscope. Fig. 1.16 shows the typical microscopic image observed during a probe-positioning procedure. The operator can observe the silhouette of the probe body, but cannot observe the head of the probe tip. Thus, the operator assumes that probe contact position is corresponding to head of the silhouette in the probing process. Unfortunately, this assumption is often incorrect in actual operation. Distance between the probe contact position and head of silhouette is different in probe models because of thickness of tip as shown in inset of figure 1.16. In addition, the distance becomes different between a used probe and a new probe even in a same probe model. As these are fundamental problems in direct observation, they exist even in fully automatic measurement systems with image processing and a Nano-probe positioner [97,98]. Use of alignment mark are popular ways to improve measurement reproducibility [90,91]. However, these methods cannot solve the problem with regard to microscope observation described above. These complex problems with respect to the probe tip cause variations in the probe position reaches to approximately 10 μm. Furthermore, since probe's contact point on a contact pad has discontinuity of EM field, the discontinuity is modeled as discontinues step in width of transmission line [94]. It is therefore unwanted-modal signal propagation is easy to be generated at the contact point of a probe. Since the impact of the unwanted signal becomes

prominent at mmW frequencies, measurement repeatability is significantly degraded by variation of probe position in the mmW frequencies. Moreover, influence of variation in probe position to phase of S-parameter becomes larger at mmW frequencies because of shorter wave-length at the frequency range. Figure 1.17 shows phase of S-parameter of the 50 Ω transmission line with changing the probe contact position. The measured data was normalized by the result when probe's position relative to the contact pad was same between the processes of calibration and evaluation of the transmission line. As shown in the figure, variation of the probe position gives significant influence to measured S-parameter. Since the problem above, evaluation results should be strongly influenced by variation of probe position.

1.6   Uncertainty analysis for S-parameter measurement

1.6.1   Difference between repeatability and uncertainty

Uncertainty is one of the expressions for possible range of error in measurement [99-101]. Measurement repeatability is often discussed in some papers, but they often stay to make several measurements and calculate standard deviation. Hence measurement results extracted by different measurement methods often deviate and become out of range of the repeatability bound. On the other hand, uncertainty includes systematic error and theorical error of measurement. Hence, two of measurement with different measurement system and method should be corresponded in the uncertainty range. Concept of uncertainty is especially effective for measurement comparison work. Thus, uncertainty analysis method is essential for metrology research field.

1.6.2   Present researches on uncertainty analysis

On-wafer measurement is widely accepted as a useful measurement technique for evaluating a high-frequency electrical circuit, which is used in modern communication devices. As described in the section 1.1.1, the operating frequencies of such devices have been reaches to millimeter-wave frequency. On-wafer measurement techniques also has been developed to accommodate millimeter-wave frequency against this background. In same manner with coaxial measurement, on-wafer measurement also requires calibration of the system preliminary to evaluate DUT. Reference plane is defined at a probe tip in the calibration process [87,88,90]. The calibration is executed by using ISS, which is typically an alumina substrate with SOLT and Line standards on it [90,91]. Recently, some European countries established a "PlanarCal" project [102]. In the project, different measurement systems were compared to investigate their reliability of the measurement system at frequencies up to 110 GHz. Moreover, other comparison works were also conducted to verify their measurement reliability. Studies reported that operator dependence of evaluated results prevents them from providing an explicit conclusion [92,103-107]. One of the major suspicions about the measurement is contact repeatability of a radio-frequency probe. For instance, probe-skating strongly impacts probe-to-pad transition because of transformation of parasitic impedance such as a mutual inductance between the probe tip and contact pad [87,88,94].

Uncertainty analyses of a VNA system are described in elsewhere [94,108-110]. Furthermore, European Association of National Metrology Institutes (EURAMET) publishes guidelines for VNA uncertainty [111]. With respect to on-wafer measurement, uncertainties derived from the inaccurate fabrication of a CPW [112,113] and probe contact position in a single axis are discussed [114]. However, a comprehensive and quantitative discussion on measurement uncertainty in on-wafer measurement, including a detailed discussion on probe positions, has not been provided. TRL calibration is widely accepted as a precision calibration method that defines the standard impedance as the difference

between thru and line standards, whose physical lengths are preliminary known [79,81]. However, calibration repeatability tends to degrade in TRL calibration because TRL calibration requires changing the distance between probes [87].

1.7   Procedures of the study

1.7.1   Aim of the study

As was described in the previous section 1.3, the absence of dielectric measurement techniques in the 300-GHz band and inhomogeneity of a substrate are critical problems of dielectric measurement in the mmW frequencies. This study focuses on the dielectric measurement techniques to address the problems.

1.7.2   Contents of study

As was described in section 1.5, variation in probe position causes large impact to on-wafer S-parameter measurement. First, the precision probing technique was developed to realize precision determination of probe contact position in Chapter 2. Further, improvement of measurement repeatability was demonstrated by the proposed probing technique in Chapter 3. Further, applications of the precision probing technique are described in the following Chapter 4, and 5. The new dielectric measurement technique, Probe-Backside Reflection (PBR) method, is demonstrated in the frequency range up to 340 GHz in Chapter 4. The proposed method in the Chapter 4 can solve the problem of absence of a dielectric measurement method at 300 GHz described in the section 1.3.1. An "In-situ" effective dielectric permittivity measurement of actual on-wafer device is demonstrated in the Chapter 5. One of the unique features of the PBR method is that the technique does not requires to prepare any resonator for the measurement. Attenuator device is used for the demonstration in this chapter. Realization of in-situ measurement

can solve the problem of inhomogeneity of material described in section 1.3.2. Contribution of this study for human society and academic fields are discussed in Chapter 6. Finally, the contents of the thesis are summarized in Chapter 7.

1.8   Summary of the chapter

Various RF devices are developed to work at the mmW frequencies. With the increase of the communication traffic, the use of the mmW frequencies is expected to solve the problems of frequency resource deficit and communication speed limitations. Various types of planar circuits are widely adopted in communication devices. The dielectric properties of a circuit substrate are essential information for the circuit design. Although various dielectric measurement techniques are developed in the microwave frequency, they have certain difficulties when they are applied in the mmW frequencies. This study focuses on the two major problems: the absence of dielectric measurement methods in the 300-GHz band and inhomogeneity of ceramics materials. To address the problems, the new dielectric measurement technique was developed in this study.

1.9   References

[1]   Ministry of internal affairs and communications, "The radio use web site," acceesed on-line at: https://www.tele.soumu.go.jp/j/adm/freq/search/myuse/summary/index.htm.

[2]   Z. Pi, and F. Khan, "An introduction to millimeter-wave mobile broadband systems," IEEE Communications Magazine, 49 6, pp.101-107, 2011.

[3]   M. Fujishima, IEICE conference 2018, BCI-2, Tokyo, 2018.3.

[4]   E. G. Larsson, O. Edfors, F. Tufvesson, and T. L. Maretta, "Massive MIMO for next generation wireless systems," IEEE Communications Magazine, 52 2, pp.186-195, 2014.

[5]   Microwave Journal, "DOCOMO, R&S Pioneering Beyond 5G with Frequency Bands Up to 150 GHz," accessed on-line at: http://www.microwavejournal.com/articles/31413-docomo-rs-pioneering-beyond-5g-with-frequency-bands-up-to-150-ghz

[6]   Network world article, "Get ready for upcoming 6G wireless, too", Accessed on-line at: https://www.networkworld.com/article/3285112/mobile-wireless/get-ready-for-upcoming-6g-wireless-too.html.

[7]   K. Takano, R. Dong, S. Lee, S. Amakawa, T. Yoshida, and M. Fujishima, "A 239-315 GHz CMOS frequency doubler designed by using a small-signal harmonic model," 13th European Microwave Integrated Circuits Conf. Dig., Madrid, Oct. 2018.

[8]   P. R. Vazquez, J. Grzyb, N. Sarmah, B. Heinemann, and U. R. pfeiffer, "Towards 100 Gbps: A fully electronic 90 Gbps one meter wireless link at 230 GHz," Euro. Microw. Conf. Dig., Madrid , Spain, 2018.

[9]   I. Kallfass, I. Dan, S. Rey, P. Harati, J. Antes, A. Tessmann, S. Wagner, M. Kuri, R. Weber, H. Massler, A. Leuther, T. Merkle, and T. Kurner, "Towards MMIC-based 300 GHz indoor wireless communication systems," IEICE Trans. Electron., E98-C, 12, pp.108-1090, 2015.

[10]   H. J. Song, "Packages for terahertz electronics," Proc. IEEE, 105 6, pp.1121-1138, 2017.

[11]   R. Minami, C. Han, K. Matsushita, K. Okada, and A. Matsuzawa, 41st European Microwave Conf. Dig., Manchester, Oct. 2011.

[12]   R. K. Hoffmann, "Handbook of microwave integrated circuits," Artech House.

[13]   Form Factor technical paper, "Impedance standard substrate (101-190) map," accessed on-line at: https://www.formfactor.com/download/iss-map-101-190/?wpdmdl=3159&refresh=5bc0a646d62711539352134

[14]   Sigma-Aldrich, "Coplanar waveguide calibration set: NIST RM8130," accessed on-line at: https://www.sigmaaldrich.com/catalog/product/sial/nistrm8130?lang=ja&region=JP.

[15]   D. F. Williams, U. Arz, and H. Grabinski, "Accurate characteristic impedance measurement on silicon," in 51st ARFTG Conf. Dig., pp.155-158, 1998.

[16]   D. F. Williams, U. Arz, and H. Grabinski, "Characteristic impedance measurement error on lossy substrate," IEEE Microw. Wireless Components Lett., 11, pp.299-301, 2001.

[17]   National Institute of Standard and Technology (NIST), "Reference Material 8130. Coplanar waveguide calibration set," MD 20899, USA, 1998.

[18]   Ceramics, "LTCC substrate," 42 10, pp.795-797, 2007.

[19]   T. Tajima, H. J. Song, and M. Yaita, "Design and analysis of LTCC-integrated planar microstrip-to-waveguide transition at 300 GHz," IEEE Trans. Microw. Technol., 64 1, pp.106-114, 2016.

[20]   J. H. Lee, G. Dejean, S. Sarkar, S. Pinel, K. Lim, J. Papapolumerou, J. Laskar, M. M. Tentzeris, "Highly integrated millimeter-wave passive components using 3-D LTCC system-on-package (SOP) technology," IEEE Trans. Microw. Theo. Technol., 53 **6**, pp.2220-2229, 2005.

[21]   T. Hu, A. Uusimaki, H. Jantunen, S. Sirisoonthorn, "Optimazation of MgTio3-CatiO3 based LTCC tapes containing B2O3 for use in microwave applications," Ceram. Int., 21 **1**, pp.85-93, 2005.

[22]   Q. Tan, H. Kang, L. Qin, J. Xiong, Z. Zhou, W. Zhang, T. Luo, C. Xue, and J. Liu, "Measurement of relative permittivity of LTCC ceramic at different temperatures," 4 3, 031316, 2014.

[23]   K. Wada, and S. Ono, "Fundamentals and vital points of planar filters in the case of miniaturization," MWE 2017 Microw. Workshop Dig., WE3B-1, Yokohama, Nov.2017.

[24]   S. Ono, and K. Wada, "Fundamentals and vital points of planar filters in the case of high frequency," MWE 2017 Microw. Workshop Dig., WE3B-2, Yokohama, Nov.2017.

[25]   J. Svacina, "Analysis of multilayer microstrip lines by a conformal mapping method," IEEE Trans. Microw. Theo. Technol., 40 **4**, pp. 769-772, 1992.

[26]   Schneider M. V., Glance B., Bodtman W. F., "Microwave and millimeter wave hybrid integrated circuits for radio systems," Bell Syst. Tech. J., 48, pp.1703-1726, 1969.

[27]   Schneider M. V., "Microstrip lines for microwave integrated circuits," Bell Syst. Tech. J., 48, pp.1421-1444, 1969.

[28]   Wheeler H. A., "Transmission line properties of parallel strips separated by a dielectric sheet," IEEE Trans. Microw. Theo. Technol., MTT-13, pp. 172-185, 1965.

[29]   Wheeler H. A., "Transmission line properties of a strip on a dielectric sheet on a plane," IEEE Trans. Microw. Theo. Technol., MTT-25, pp. 631-647, 1977.

[30]   Y. Kato, "A survey on measurement techniques of dielectric properties and dissemination of their national standards," AIST bulletin of Metrology, 9 1, pp.99-116, 2014.

[31]   Agilent technologies technical paper, "Impedance measurement handbook,"   accessed   on-line   at: http://literature.cdn.keysight.com/litweb/pdf/5950-3000JA.pdf.

[32]   R. Sakamaki, "A survey on impedance standards and their application for evaluation of battery devices," AIST bulletin of Metrology, 9 3, pp.355-370, 2016.

[33]   R. Sakamaki, B. Cheng, J. Cai, Y. H. Lin, C. W. Nan, and J, He," Preparation of TiO2-enriched CaCu3Mn0.1Ti3.9O12 ceramics and their dielectric properties," J. Euro. Ceram. Soc., 30 1, pp.95-99, 2010.

[34]   A. K. Jonscher, "The universal dynamic response," Nature, 267, pp.672-679, 1977.

[35]   A. S. Nowick, A. V. Vaysleyb and I. Kuskovsky, "Universal dielectric response of variously doped CeO2 ionically conducting ceramics," Phys. Rev. B, 58 **13**, pp.8398-8406, 1998.

[36]   W. Cao, and R. Gerhardt, "Calculation of various relaxation times and conductivity for a single dielectric relaxation process," Solid State Ionics, 42, pp.213-221, 1990.

[37]   A. K. Jonscher, "Hopping losses in polarisable dielectric media," Nature, 250, pp.191-193, 1974.

[38]   D. Popovici, H. Nagai, S. Fujishima, and J. Akedo, "Preparation of lithium aluminum titanium phosphate electrolytes thick films by aerosol deposition method," J. Am. Ceram. Soc., 94 11, pp.3847-3850, 2011.

[39]   H. Kinbara, T. Harigai, H, Kakemoto, and T, Tsurumi, "Temperature Dependence of Dielectric Permittivity of Perovskite-type Artificial Superlattices," IEEE Trans. Ultrasonics, Ferrorelectrics, and Frequency control, 54 12, pp.2541-2547, 2007.

[40]   J.R. Macdonald, "Impedance Spectroscopy Emphasizing solid materials and systems," Wiley, 1987.

[41]   E. Barsoukov, J. R. Macdonald, "Impedance Spectroscopy Second Edition," Wiley, 2005.

[42]   E. Karden, S. Buller, R. W. De Doncker, "A method for measurement and interpretation of impedance spectra for industrial batteries," J. Power Sources, Vol.85, pp.72-78, 2000.

[43]   E. Karden, S. Buller, R. W. De Doncker, "Frequency Domain approach to dynamical modeling of electrochemical power sources," Electrochimica Acta, 47, pp.2347-2356, 2002.

[44]   S. Bullar, M. Thele, E. Karden, R. W. De Doncker, "Impedance-based non-linear dynamic battery modeling for automotive applications," J. Power Sources, 113 pp.422-430, 2003.

[45]   Y. Kobayashi, and A. Nakayama, "Round Robin Test on a cavity resonance method to measure complex permittivity of dielctric plates at microwave frequency," IEEE Trans. Dielec. Electr. Insul., 13 **4**, pp.751-759, 2006.

[46]   R. N. Clarke, A. P. Gregory, D. Cannell, M. Patrick, S. Wylie, I. Youngs, and G. Hill, "A guide to the characterisation of dielectric materials at RF and microwave frequencies," Institute of Measurement and Control / NPL, 3687, 2003.

[47]   H. W. Chao, and T. H. Chang, "Wide-range permittivity measurement with a parametric-dependent cavity," IEEE Trans. Microw. Theo. Technol., 66 **10**, pp. 4641-4648, 2018.

[48]   M. D. Janezic, J. B. Jarvis, "Full-wave analysis of a split-cylinder for nondestructive permittivity measurements," IEEE Trans. Microw. Theo. Technol., 40 **10**, pp. 2014-2020, 1999.

[49]   J. B. Jarvis, M. D. Janezic, B. Riddle, C. L. Holloway, N.G. Paulter, and J. E. Blendell, "Dielectric and conductor-loss characterization and measurements

on electronic packaging materials," Natl. Inst. Stand. Technol. Techn., 1520, 2001.

[50]   K. Araki, D. I. Kim, and Y. Naito, "A Study on Circular Disk Resonators on a Ferrite Substrate," IEEE Trans. Microw. Theo. Technol., 30 **2**, pp. 147-154, 1982.

[51]   H. Kawabata, and Y. Kobayashi, "The analysis of a balanced-type circular disk resonator excited by coaxial cable lines to measure the complex permittivity," APMC 2001 Conf. Dig., 01TH8577, Taipei, Dec. 2001.

[52]   Y. Kato, and M. Horibe, "Permittivity measurements and associated uncertainties up to 110 GHz in circular-disk resonator method," Euro. Microw. Conf. Dig., P01-42, London, Oct. 2016.

[53]   J. B. Jarvis, "Transmission/reflection and short-circuit line permittivity measurement," Natl. Inst. Stand. Technol. Techn., 1341, 1990.

[54]   J. B. Jarvis, M. D. Janezic, B. F. Riddle, R. T. Johnk, P. Kabos, C. L. Holloway, R. G. Geyer, and C. A. Grosvenor, "Measuring the Permittivity and Permeability of Lossy Materials: Solids, Liquids, Metals, Building Materials, and Negative-Index Material," Natl. Inst. Stand. Technol. Techn., 1536, 2005.

[55]   J. H. Kim, "Permeability measuremts of thin sheet materials and uncertainty analysis," 91st ARFTG Conf, Dig., Philadelphia, Mar. 2018.

[56]   P. Skocik, and P. Neumann, "Measurement of Complex Permittivity in Free Space," Proc. Eng., 100, pp.100-104, 2015.

[57]   Z. Awang, F. A. M. Zaki, N. H. Baba, A. S. Zoolfakar, and R. A. Bakar, "A FREE-SPACE METHOD FOR COMPLEX PERMITTIVITY MEASUREMENT OF BULK AND THIN FILM DIELECTRICS AT MICROWAVE FREQUENCIES," Prog. Electr. Res. B, 51, pp.307-328, 2010.

[58]   E. Hajisaeid, A, F. Dericioglu, A. Akyurtlu, "All 3D printed free-space setup for microwave dielectric characterization of materials," IEEE Trans. Inst. Meas., 67 **8**, pp.1877-1886, 2018.

[59]   P. H. Bolivar, M. Brucherseifer, J. G. Rivas, R. Gonzalo, I. Ederra, A. L. Reynolds, M. Holker, and P. Maagt, "Measurement of the Dielectric Constant and Loss Tangent of High Dielectric-Constant Materials at Terahertz Frequencies," IEEE Trans. Microw. Theo. Technol., 51 **4**, pp. 1062-1066, 2003.

[60]   K. Z. Rajab, M. Naftaly, E. H. Linfield, J. C. Nino, D. Arenas, D. Tanner, R. Mittra, and M. Lanagan, "Broadband dielectric characterization of aluminum oxide," J. Micro. And Elect. Pack., 5, pp.101-106, 2008.

[61]   Y. Kimura, Y. Sato, and S. Yoshikado, "Evaluation of beta-Al2O3 by transmittance and reflectance measurement using the terahertz time domain spectroscope," JSAP meeting 2014 spring, 17a-PA2-16, Tokyo, Mar.2014.

[62]   M. Naftaly, and R. E. Miles, "Terahertz Time-Domain Spectroscopy for Material Characterization," Proc. IEEE, 95 **8**, pp.1658-1665, 2007.

[63]   Y. Kim, M. Yi, B. G. Kim, and J. Ahn, "Investigation of THz birefringence measurement and calculation in Al2O3 and LiNbO3", Appl. Opt., 50 18, pp. 2906-2910, 2011.

[64]   N. Matsumoto, T. Nakagawa, A. Ando, Y. Sakabe, S. Kirihara, and Y. Miyamoto, "Study of Multilayer Ceramic Photonic Crystals in THz Region," J. Jap. Appl. Phys., 44 9B, pp. 7111-7114, 2005.

[65]   M. Feneberg, J. Nixdorf, M. D. Neumann, N. Esser, L. Artus, R. Cusco, T. Yamaguchi, R. Goldhahn, "Ordinary dielectric function of corundum-like -Ga2O3 from 40 meV to 20 eV," Phys. Rev. Mater., 2, 044601, 2018.

[66]   A. N. Deleniv, S. Gevorgian, "Open resonator technique for measuring multilayerd dielectric plates," IEEE Trans. Microw. Theo. Tech., 53 9, pp.2908-2916, 2005.

[67]   M. A. Saed, "Measurement of the complex permittivity of low-loss planar microwave substrates using aperture-coupled microstrip resonators," IEEE Trans. Microw. Theo. Tech., 41 8, pp.1343-1348, 1993.

[68]   J. Barowski, M. Zimmermanns, and I. Rolfes, "Millimeter-wave characterization of dielectric materials using calibrated FMCW transceivers," IEEE Trans. Micow. Theo. Tech., 66 8, pp.3683-3689, 2018.

[69]   E. Semouchkina, W. Cao, M. Lanagan, "High frequency permittivity determination by spectra simulation and measurement of microstrip ring resonators," Electr. Lett., 36 **11**, pp.956-958, 2000.

[70]   P. A. Bernard, J. M. Gautray, "Measurement of dielectric constant using a microstrip ring resonator," IEEE Trans. Microw. Theo. Technol., 39 **3**, pp. 592-595, 1991.

[71]   I. Waldron, "Ring resonator method for dielectric permittivity measurement of foams," Master thesis in Worcester polytechnic institute, 2006.

[72]   D. I. Amey, and J. P. Curilla, "Microwave properties of ceramic materials," 1991 Proc. 41st Electr. Components and Technol. Conf., Atlanta, May 1991.

[73]   A. E. Fathy, A. Pendrich, B. D. Geller, S. M. Perlow, S. Tormey, A. Prabhu, and S. Tani, "An innovative semianalytical technique for ceramics evaluation at microwave frequencies," IEEE Trans. Microw. Theo. Technol., 50, pp. 2247, 2002.

[74]   T. Jyo, H. Hamada, D. Kitayama, M. Yaita, A. E. Moutaouakil, H. Matsuzaki, and H. Nosaka, "Fast and Accurate THz Permittivity Measurement Using a Self-Heterodyne Technique and Multitone Signal With Nonuniform Intervals," IEEE Trans. Microw. Theo. Technol., 66 **10**, pp.4649-4657, 2018.

[75]   X. Bao, S. Liu, I. Ocket, J. Bao, D. Kil, S. Zhang, C. Cheng, K. Feng, G. Avolio, B. Puers, D. Schreurs, and B. Nauwelaers, "Coplanar waveguide for dielectric material measurements at frequency from 140 GHz to 220 GHz," 90th ARFTG Conf. Dig., Boulder, 2017.

[76]   D. F. Williams, A. C. Young, and M. Urteaga, "A Prescription for Sub-Millimeter-Wave Transistor Characterization," IEEE Trans. Terahertz Technol., 3 4, pp.433-439, 2013.

[77]   G. F. Engen, and C. A. Hoer, "Thru-reflect-line: An improved technique for calibrating the dual six-port automatic network analyzer," IEEE Trans. Microw. Theo. Technol., 27 **12**, pp.987-993, 1979.

[78]   D. F. Williams, C. M. Wang, and U. Arz, "An optimal multiline TRL calibration algorithm," IEEE MTT-S IMS Dig., Philadelphia, Jul.2003.

[79]   H. J. Eul, and B. Schiek, "A generalized theory and new calibration procedures for network analyzer self-calibration," IEEE Trans. Microw. Theo. Technol., 39 **4**, pp.724-731, 1991.

[80]   R. B. Marks, and D. F. Williams "A general waveguide circuit theory," J. Res. NIST, 97 5, pp.533-562, 1992.

[81]   R. B. Marks, "A multiline method of network analyzer calibration," IEEE Trans. Microw. Theo. Technol., 39 **7**, pp.1205-1215, 1991.

[82]   A. Orii, M. Suizu, S. Amakawa, K. Katayama, K. Takano, M. Motoyoshi, T. Yoshida, M. Fujishima, "On the length of THRU standard for TRL de-embedding on Si substrate above 110 GHz," IEEE ICMTS 2013 Conf. Dig., Osaka, Jun.2013.

[83]   D. K. Ryutting, "Improved RF hardware and calibration methods," Accessed on-line at: http://na.support.keysight.com/faq/symp.pdf.

[84]   D. K. Ryutting, "Network analyzer error models and calibration methods," Accessed   on-line   at: http://www2.electron.frba.utn.edu.ar/~jcecconi/Bibliografia/04%20-%20Param_S_y_VNA/Network_Analyzer_Error_Models_and_Calibration_Methods.pdf.

[85]   R. A. Soares, P. Gouzien, P. Legaud, and G. Follot, "A unified mathematical approach to two-port calibration techniques and some applications," IEEE Trans. Microw. Theo. Technol., 39 **11**, pp.1669-1674, 1989.

[86]   D. K. Ryutting, "An analysis of vector measurement accuracy enhancement techniques," Accessed on-line at: http://na.support.keysight.com/faq/accuracy.pdf.

[87]   A. Davidson, E. Strid, and K. Jones, "Achieving greater on-wafer S-parameter accuracy with the LRM calibration technique," 34th ARFTG Conf. Dig., Ft. Lauderdale, Nov.1989.

[88]   A. Davidson, K. Jones, and E. Strid, "LRM and LRRM Calibrations with Automatic Determination of Load Inductance," 36th ARFTG Conf. Dig., Monterey, Nov.1990.

[89]   Y. Sugimoto, N. Mori, Y. Moriya, and T. Takada, "Dielectric properties of new LTCC material applied to high frequencies," J. Ceram. Soc. Jap., 122 6, pp.492-495, 2014.

[90]   C. Doan, "Introduction to on-wafer characterization at microwave frequency," accessed on-line at: http://web.doe.carleton.ca/~nagui/labequip/loadpull/papers/calibration/CascadeMicro_On-Wafer_Characterization.pdf.

[91]   Form Factor technical paper, "Probes selection guide," accessed on-line at: https://www.formfactor.com/download/probe-selection-guide/?wpdmdl=2561&refresh=5bc1a0122dafc1539416082.

[92]   T. Probst, R. Doerner, M. Ohlrogge, R. Lozae, U. Arz, "110 GHz on-wafer measurement comparison on alumina substrate," 90th ARFTG Conf. Dig., Boulder, USA, Nov. 2017.

[93]   L. Chen, C. Zhang, T. J. Reck, A. Arsenovic, M. Bauwensm C. Groppi, A. W. Lichtenberger, R. M. Weikle, N. S. Barker, "Terahertz Micromachined On-Wafer Probes: Repeatability and Reliability," IEEE Trans. Microw. Theo. Technol., 60 9, pp. 2894-2902, 2012.

[94]   L. Galatro, F. Mubarak, and M. Spirito, "On the definition of reference planes in probe-level calibations," 87th ARFTG Conf. Dig., San Francisco, Jun.2016.

[95]   K. Jones, and E. Strid "Where are my on-wafer reference planes?," 30th ARFTG Cof. Dig., Dallas, USA, 1987.

[96]   M. Spirito, L. Galatro, G. Lorito, T. Zoumpoulidis, and F. Mubarak, "Improved RSOL planar calibration via EM modelling and reduced spread resistive layers," 86th ARFTG Conf. Dig., Atlanta USA, 2015.

[97]   F. T. K. Retzow, T. Tiemerding, P. Elfert, O. C. Haenssler, and S. Fatikow, "Automated calibration of RF on-wafer probing and evaluation of probe misalignment effects using a desktop micro-factory," J. Comput. Commun., vol. 4, no. 3, pp. 61–67, Mar. 2016.

[98]   K. Daffé, G. Dambrine, F. von Kleist-Retzow, and K. Haddadi, "RF wafer probing with improved contact repeatability using nanometer positioning," in 87th ARFTG Dig., May 2016, pp. 1–4.

[99]   Bureau international des poids et mesures (BIPM), "Guide to the expression of uncertainty in measurement (GUM)," Paris, 1st edition, 2008.

[100]   European Association of National Metrology Institute (EURAMET), "Guideline on the evaluation of vector network analysers", cg-12 ver3.0, Braunschweig, 2016.

[101]   M. Garelli, and A. Ferrero, "A Unified Theory for S-Parameter Uncertainty Evaluation," IEEE Trans. Microw. Theo. Technol., 60 **12**, pp.3844-3855, 2012.

[102]   EMPIR, "IND02 'PlanarCal," Accessed on-line at: https://planarcal.ptb.de/.

[103]   R. G. Clarke, C. Li, and N. N. Ridler, "An intra-laboratory investigation of on-wafer measurement reproducibility at millimeter-wave frequencies," 90th ARFTG Conf. Dig., Boulder, 2017.

[104]   R. James, "Verification of 110 GHz on-wafer VNA probe systems," COMPASS 2016, Portland, 2016.

[105]   R. G. Clarke, J. Quraishi, and N. M. Ridler, "A bilateral comparison of on-wafer S-parameter measurements at millimeter wavelengths," 69th ARFTG Conf. Dig., Honolulu, 2007.

[106]   J. R. Fenton, "Validation of on-wafer vector network analyzer systems," 68th ARFTG Conf. Dig., Broomfield, 2006.

[107]   T. Probst, S. Zinal, R. Doerner, and U. Arz, "On the importance of calibration standards definitions for on-wafer measurements up to 110 GHz," 91st ARFTG Conf. Dig., Philadelphia, Jun.2018.

[108]   A. Arsenovic, L. Chen, M. F. Bauwens, H. Li, N. S. Barker, and R. M. Weikle, "An Experimental Technique for Calibration Uncertainty Analysis" IEEE Trans. Microwave Theo. Tech., vol. 61, no. 1, pp. 263–269, Nov. 2012.

[109]   R. A. Ginley, "Establishing traceability for SOLT calibration kits," in 90th. ARFTG Dig., pp. 1-4, November 2017.

[110]   R. A. Ginley, "VNA uncertainties," in 86th. ARFTG short course, December 2015.

[111]   Guidelines on the evaluation of vector network analysers (VNA) version 3.0, European Association of National Metrology Institutes., Bundesallee, Germany, 2016.

[112]   A. A. Savin, V. G. Guba, and O. N. Bykova, "Uncertainty analysis in coplanar waveguide with unscented transformation," in 86th. ARFTG Dig., pp. 1-4, December 2015.

[113]   J. Leinhos, and U. Arz, "Monte-Carlo analysis of measurement uncertainties for on-wafer thru-reflect-line calibrations," in 71st. ARFTG Dig., pp. 1-4, June 2008.

[114]   A. M. E. Safwat, and L. Hayden, "Sensitivity Analysis of Calibration Standards for SOLT and LRRM," in 58th. ARFTG Dig., pp. 1-4, November 2001.
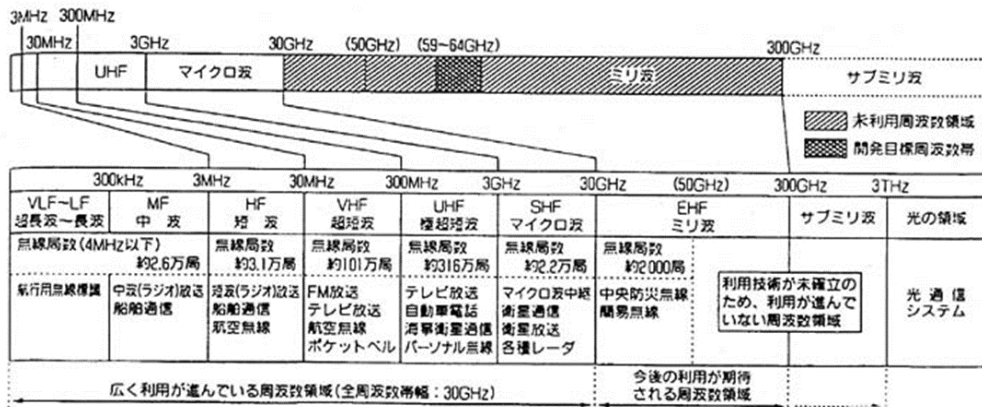
Figure 1.1   Assignment of radio wave by Ministry of internal affairs and communications [1].
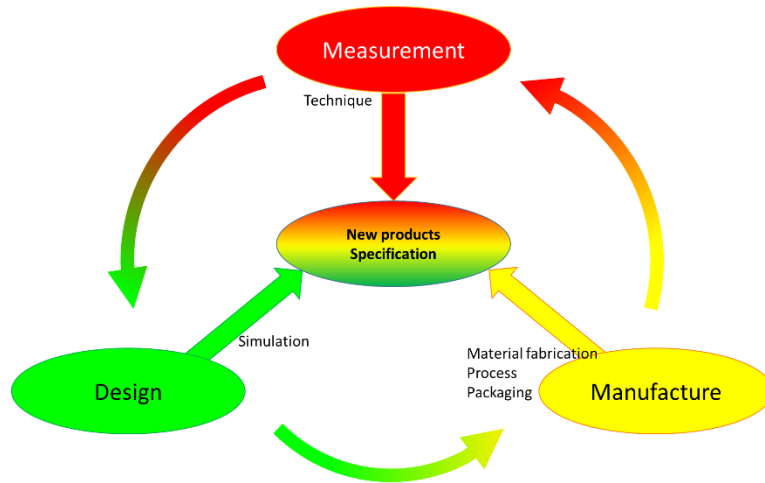

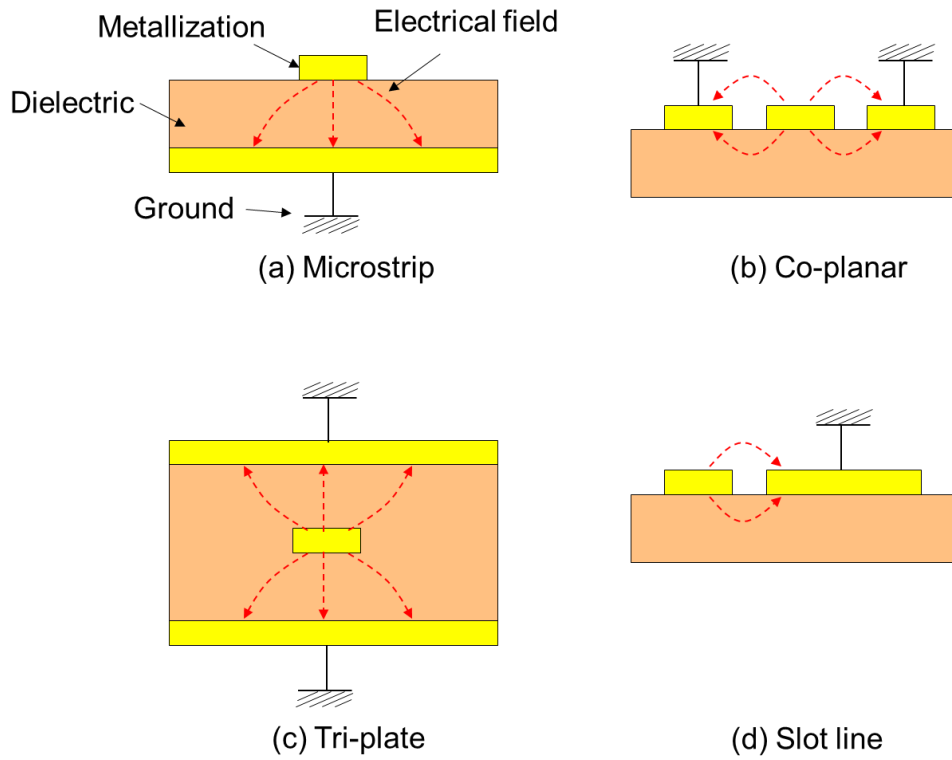Figure 1.2   Work flow for development electronic product.

Figure 1.3   Structure of the various planar-circuits. Broken lines indicate electrical field distributions.
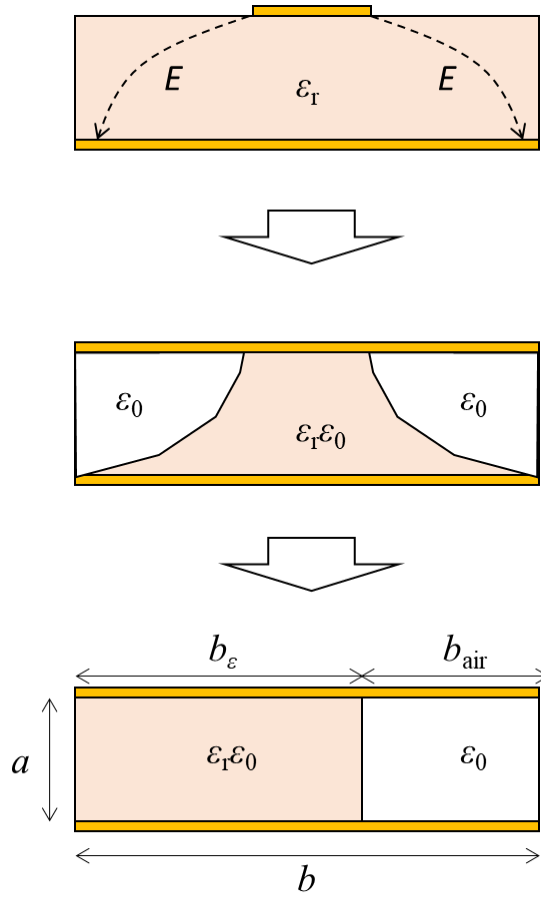
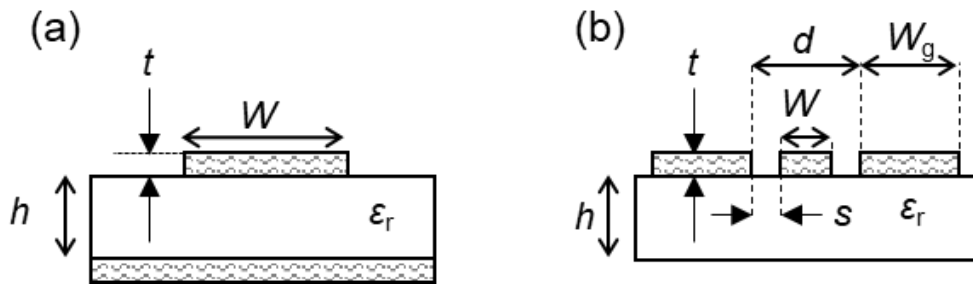Figure 1.4   Transformation process of conformal mapping model for MSTL.

Figure 1.5   Definition of each dimension in (a) MSTL, and (b) CPW
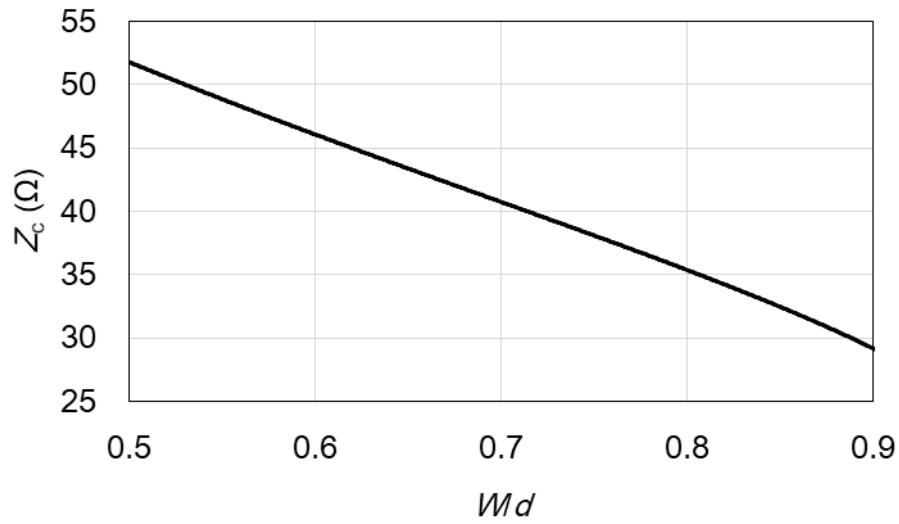
Figure 1.6   Circuit dimension dependence of characteristic impedance of CPW.
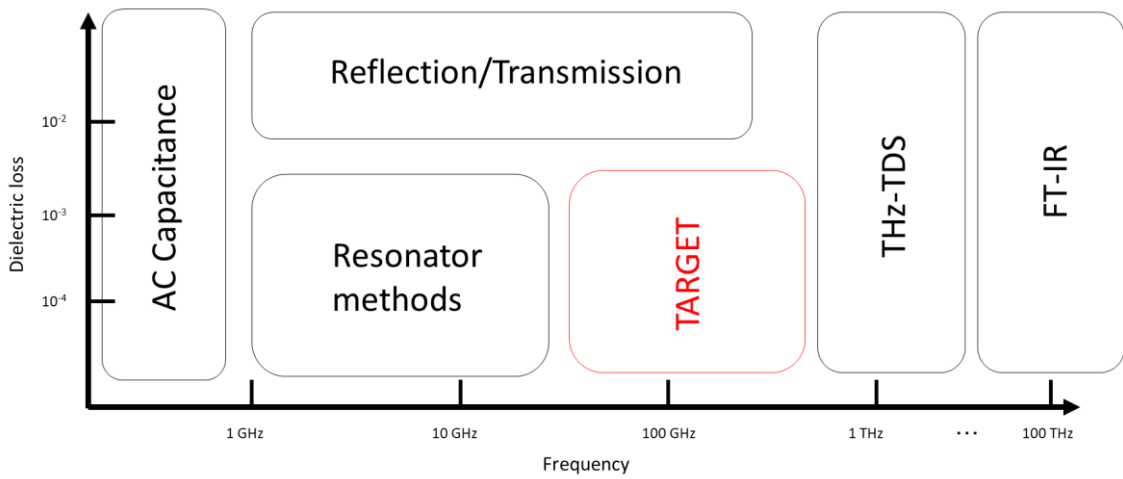

Figure 1.7   Various dielectric measurement techniques and their applicable ranges.
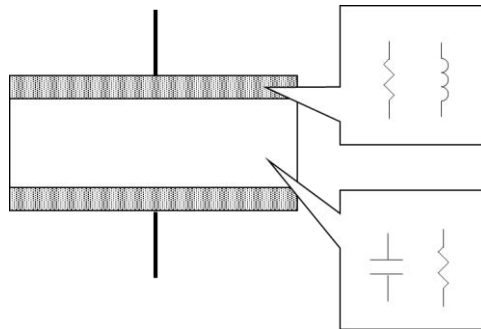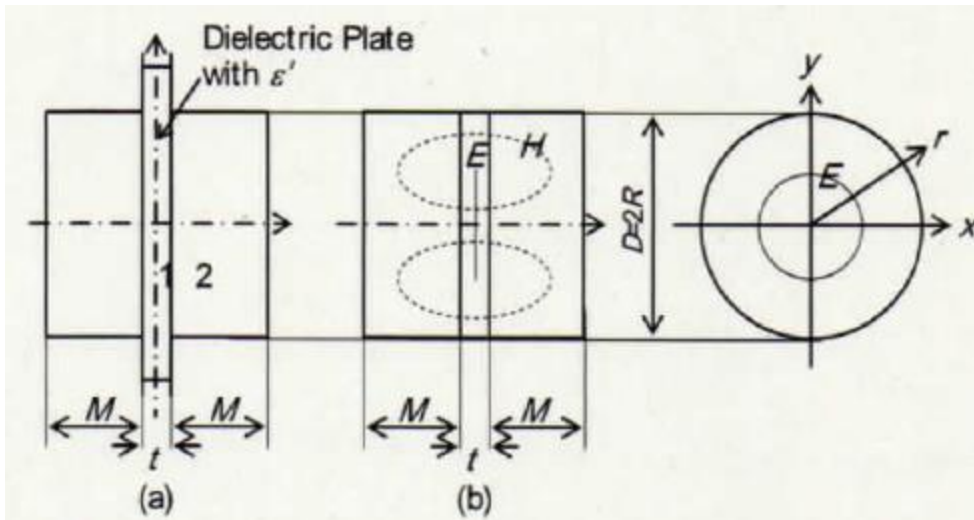
Figure 1.8   Illustration of capacitance method

Figure 1.9   Structure of a cavity for cavity resonance method. (a) Resonator used in measurement, and (b) resonator to calculate ε_r and $\tan\delta$. [45]
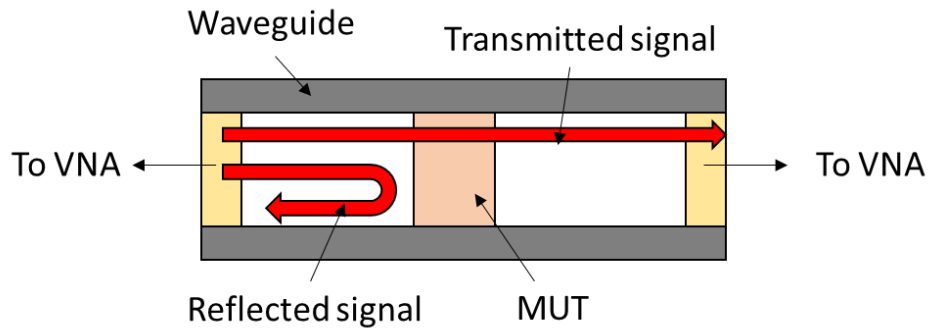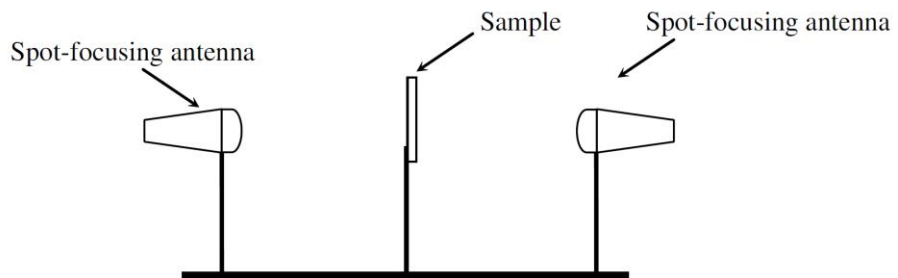
Figure 1.10   Illustration of R/T method.

Figure 1.11   Illustration of set-up of Free space method [57]
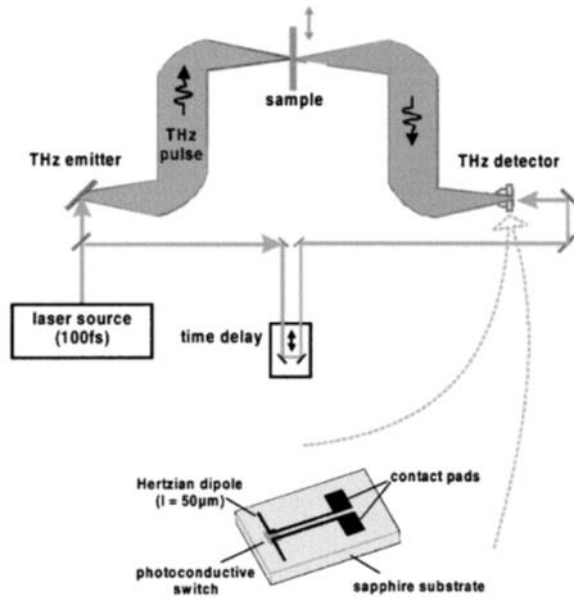
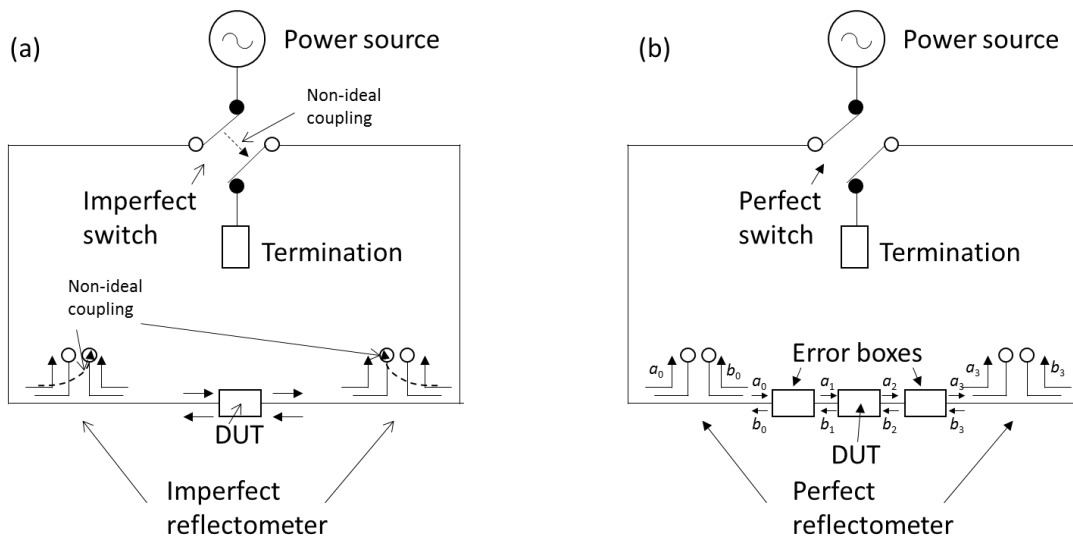Figure 1.12   Illustrations of THz-TDS method [59]

Figure 1.13   (a) Basic structure of VNA, and (b) a model of error correction with the error boxes.
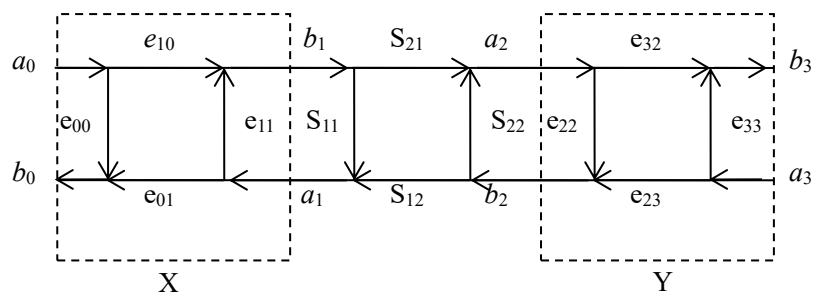
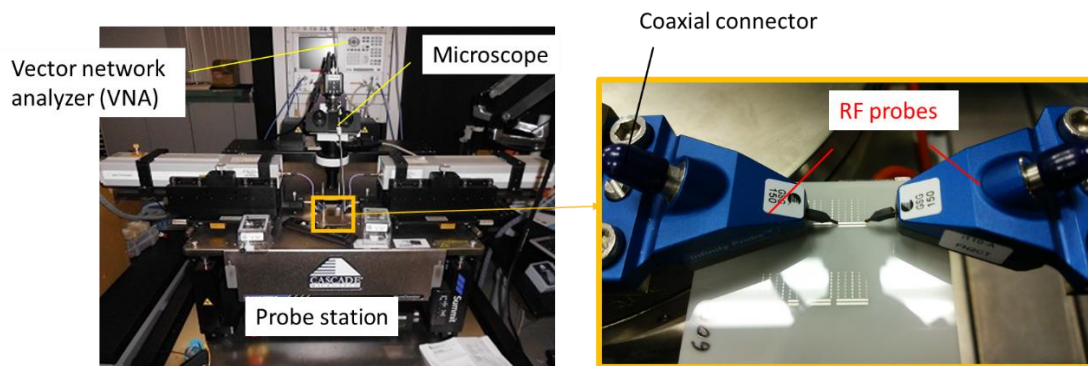Figure 1.14   8 terms error model
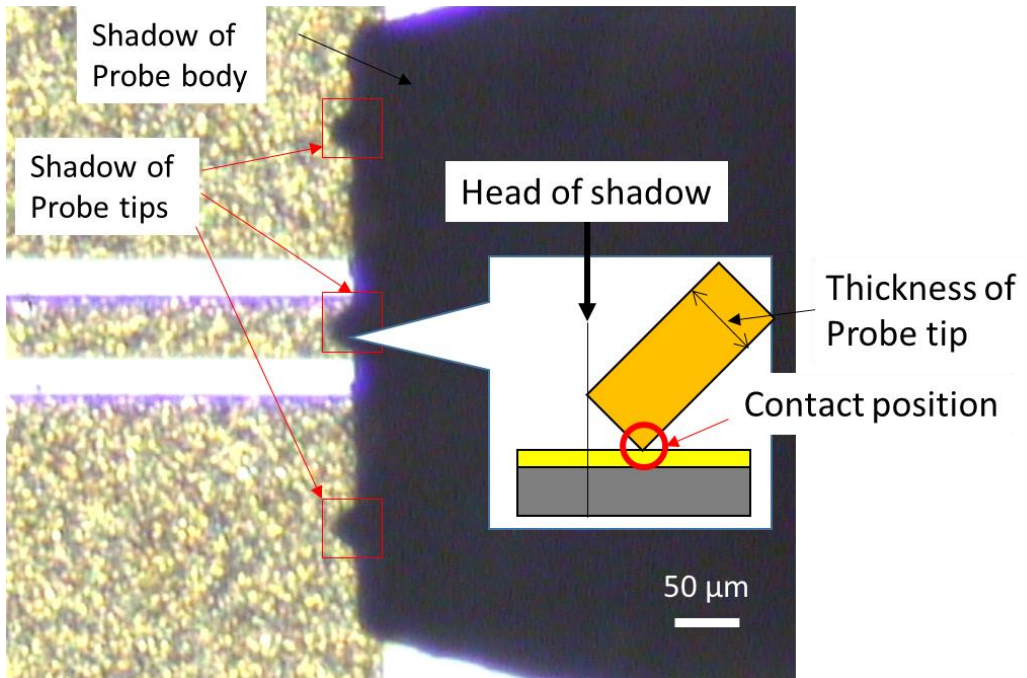

Figure 1.15   Images of on-wafer measurement system

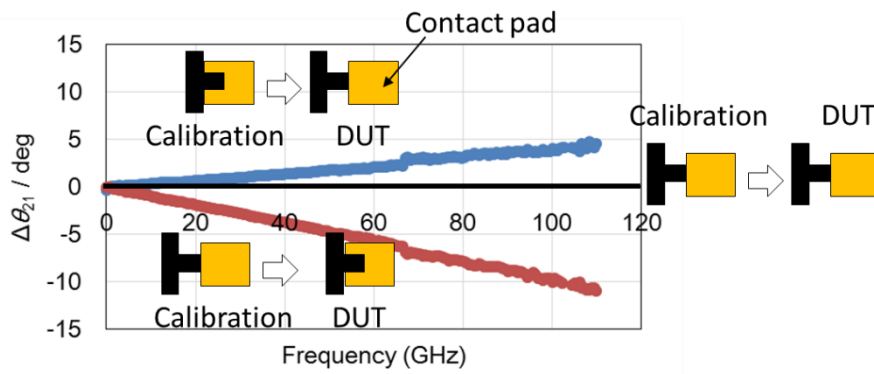Figure 1.16 Typical image of probe and its tips

Figure 1.17　Impact of variation in probe position

Chapter 2   Precision probing technique for improving repeatability in probe contact position

2.1   Contents of chapter 2

This chapter describes the precision probing technique and improvement of repeatability in probe contact position. The proposed probing technique can be adopted for various device measurements even in the frequency range up to 340 GHz. The detail of the technique is provided in "Paper I: IET Microw. Antennas Propag., 11, 1892 (2017)", "Paper II: IEEE Trans. Inst. Meas., 67 8, (2018)", "Conference paper I: CPEM 2018 Conf. Dig., (2018)", and "Conference paper II: EuMC 2018 Conf. Dig., (2018)".

2.2   Construction of measurement system

2.2.1   Construction of probe station

The components of the measurement system and the measurement conditions are listed in Table 2.1 and Table 2.2. A probe station and VNA were controlled by MATLAB-based measurement algorithms. A fully automatic probe station, as shown in figure 2.1, was constructed to realize an automatic probing system. Precision XYZ stages, MCU-099 (Kouzu-seiki), were used as the 2-port probe positioners, and XY stages, HPS80-50X, with a Z stage, OSMS80-20ZF (Sigma-koki), were used as a sample stage. In this study, the frequency range of 10 MHz−110GHz is named as "100-GHz band", and frequency range of 190 GHz−340 GHz is named as "300 GHz-band".

Table 2.1   Measurement system and conditions for 100 GHz band.

Items	Components and conditions
RF probes	Infinity-GSG-150

VNA system	N5260-016
Frequency range	10 MHz–110 GHz
IF band width	1 kHz
Measured points	2

Table 2.2   Measurement system and conditions for 300 GHz band.

Items	Components and conditions
RF probes	Infinity-GSG-75
VNA	N5222B
Frequency extender	V03VNA2-T/R
Frequency range	190 GHz–340 GHz
Measured points	2
IF band width	1 kHz

2.2.2   Preparation of impedance standard substrate

TRL calibrations were used as the calibration method. An impedance standard substrate (ISS) was fabricated for this purpose (Fig 2.2). Fig. 2.3 depicts the illustration of a typical THRU standard. Each calibration standard had alignment patterns on both the left and right. The delays of the THRU and the five LINE standards were 1 ps, 3 ps, 7 ps, 14 ps, 27 ps, and 40 ps, respectively. The alignment pattern was a simple short device with a contact pad, for a Ground-Signal-Ground (GSG) probe. The alignment patterns were fabricated around each standard and verification device; however, they were located 1-mm away from the standards and devices to avoid intercalation.

2.3   Precision probe adjustment by RF-signal detection
2.3.1   Theory and methodology of demonstration

The probe coordinates in the X-, Y-, and Z- axes were automatically aligned by detecting the edges of the alignment, as shown in Fig. 2.4. The procedure for probe alignment is described below.

Before the automatic alignment, a probe is roughly aligned on a pad of the alignment patterns. This step is a last operation requested for an operator, and this operation does not give influence to final probe position. After that, the system gradually shifts down the probe in 1-μm step with monitoring S-parameter. Figure 2.5 shows the procedure of detection of probe touch-down. Measured reflection coefficient should be in certain point in a smith chart when a probe is floated in air. On the other hand, measured reflection coefficient should become perfectly different when the probe is touched down on conductor. It is therefore, a standard Z-coordinate can be defined at the surface of conductor by shifting down the probe in Z-axis with monitoring the reflection coefficient till detecting a steep change of it. Next, the probe is shifted to opposite direction to align the probe out of the contact pad. After that, the probe was shifted to approach direction with repeating probe release and touchdown. The edge of alignment pattern can be detected in the same manner. A standard Y-coordinate also defined in the same manner, but upper and bottom sides of edges were detected to define a standard coordinate as intermediate of the both edges. In this way, we can realize reproducible definition of standard coordinates of probe position relative to the alignment patterns.

Not only the X, Y, and Z- coordinates, but probe tilt angle also should be precisely adjusted to improve probe positional repeatability. Figure 2.6 shows equivalent circuits with different numbers of contacted probe tips. As shown in the figure, different parasitic impedance should be assumed due to different contact conditions. This resulted in different measured S-parameter as shown in Figure 2.7. This result indicates that probe tilt angle can be automatically adjusted by analyzing the measured S-parameter. In this paper, the probe tilt angle was adjusted by changing the angle to the point where the measured S-parameter is in the third quadrant in the polar map.

2.3.2   Estimation in repeatability of probes distance

Reproducibility of probe distance were investigated by using both of the alignment technique, those are the conventional manual technique and the proposed probing technique. The two of probes were aligned at the both edge of the line by the both techniques. However, it was difficult to measure distance between two probes accurately. Thus, difference in the probes distance between two of transmission line measurements (Δd) was investigated in this time. The Δd was calculated by using absolute coordinates of the probe positioners by using equation (1) and (2), where x_i^p, y_i^p, and z_i^p are the coordinates of the probe stages at port p (p=1,2), and i corresponds to each line. This operation was repeated for 4 times for both of the techniques. Finally, standard deviations of Δd were calculated.

$$X_i = x_i^1 - x_i^2, Y_i = y_i^1 - y_i^2, Z_i = z_i^1 - z_i^2 \quad \text{(i=1,2)} \tag{1}$$

$$\Delta d = \sqrt{(X_2 - X_1)^2 + (Y_2 - Y_1)^2 + (Z_2 - Z_1)^2}. \tag{2}$$

Figure 2.8 shows a standard deviation of Δd. As shown in the figure, the Δd was greatly reduced from 10 μm in the conventional technique to 2 μm by the precision probing technique even in the 300 GHz band. The developed probing system does not require microscope and an operator intervention. Thus, repeatability in probe positioning can be improved to 2 μm comparing to the conventional manual inspection, which is beyond resolution of the microscope. Because the positional repeatability of two probe stages contribute to variation in Δd, repeatability of the signal probe is estimated approximately 1 μm.

2.4   Conclusion of chapter 2

The precision probing technique was demonstrated in this chapter. The results are summarized below:

1) A fully automatic probe station and original ISS were prepared to realize the precision probing technique. Each standard on the ISS has the alignment patterns to define the origin coordinates of the probes.

2) Repeatability in probes distance was reduced to 2 μm by using the technique even in the frequency range up to 340 GHz, which extend up to 10 μm in the conventional manual probing technique.

3) Mechanism of the S-parameter threshold technique is so simple that it can realize universal use for various probe models and devices. Thus, the precision probing technique is used in the following chapters.
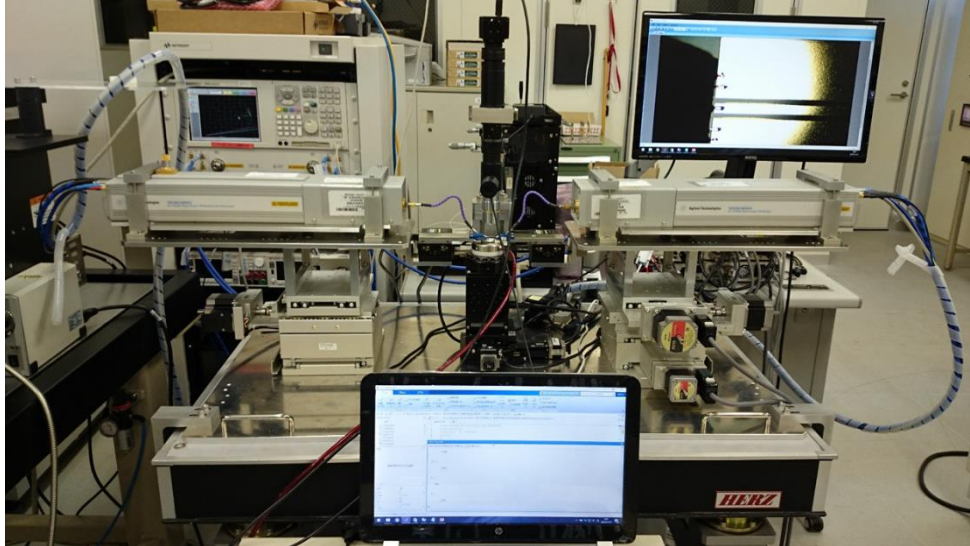
Figure 2.1 Image of constructed measurement system.
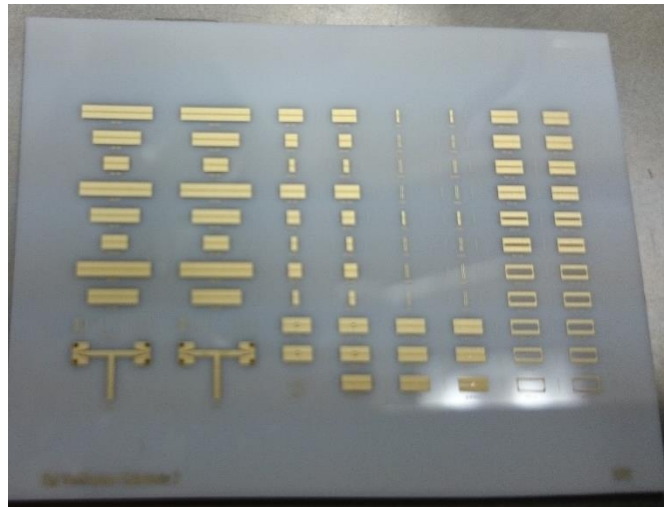
Figure 2.2 Image of an original impedance standard substrate.
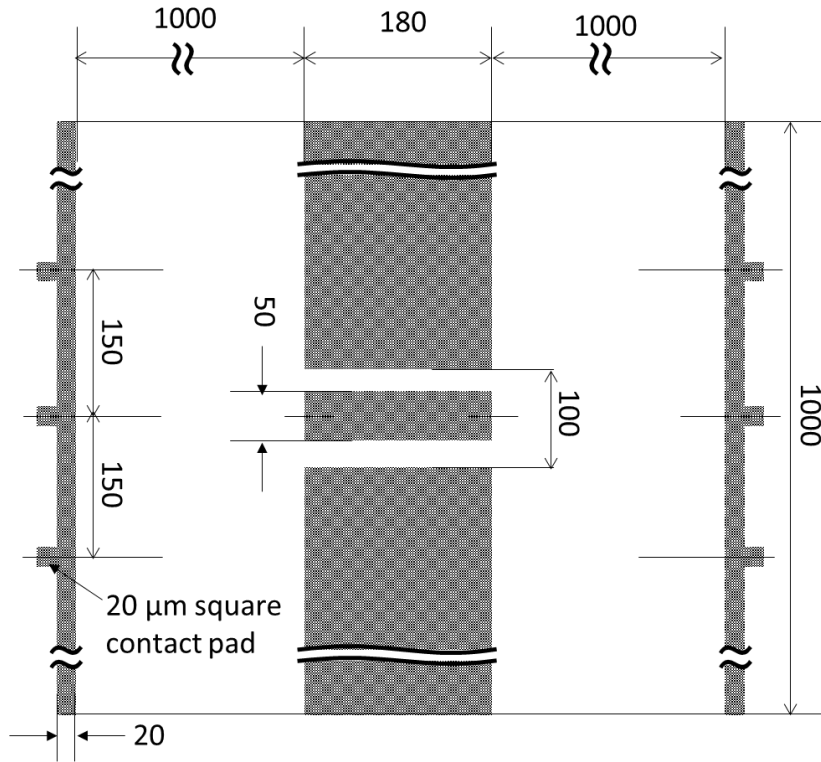
Figure 2.3   Structure of a typical thru standard (center) with the alignment
patterns (both left and right sides).
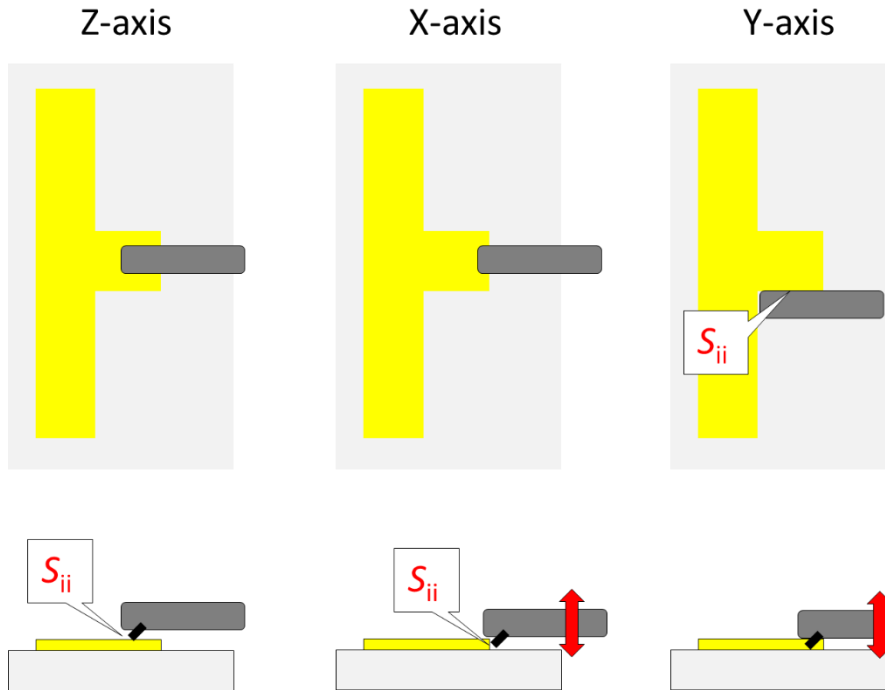
Figure 2.4   Schematic illustration of the procedure for determining the origin coordinates in the X-, Y-, and Z- axes. The upper illustrations show top views and the bottom figures show cross views in the alignment processes.
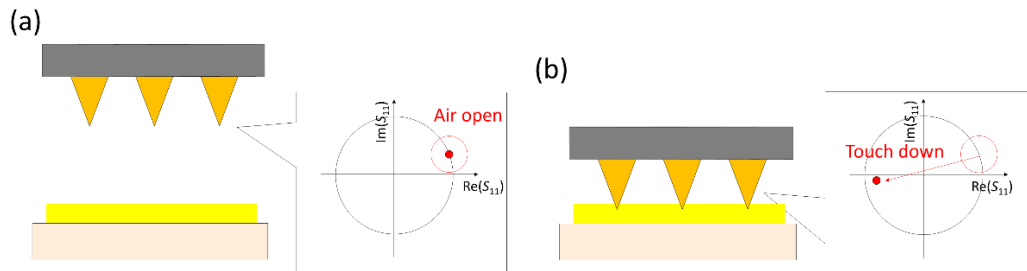
Fig. 2.5 Procedure for the definition of a standard Z-coordinate. (a) Air-open and (b) touch-down on CPW.
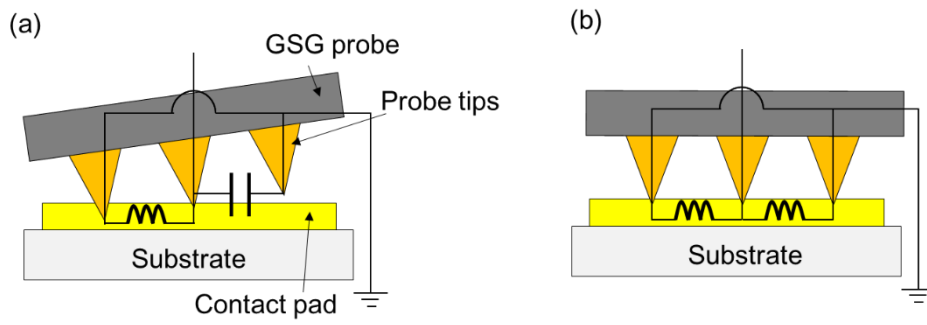
Figure 2.6 Parasitic impedance around a probe and a circuit substrate. (a) 2 of probe tips, and (b) all of probe tips, are contacted on the conductor.
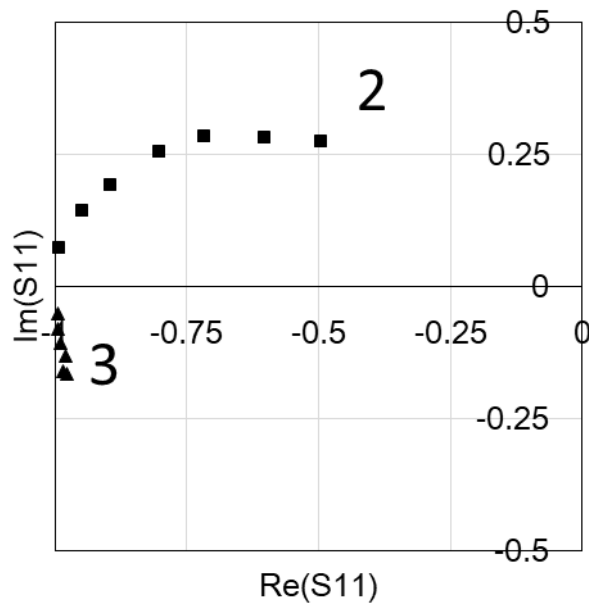
Figure 2.7 S-parameter polar map with different numbers of the contacted probe tips.
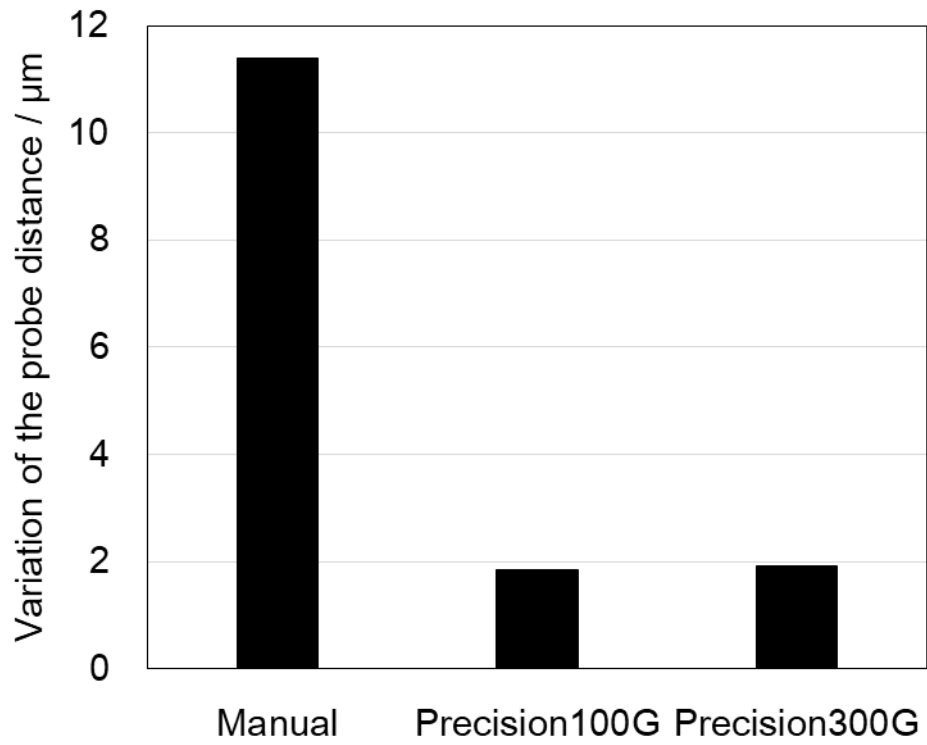
Figure 2.8 Comparison of repeatability of probes distance.

Chapter 3   Demonstration of the precision probing technique for improving measurement repeatability

3.4   Contents of chapter 3

This chapter describes improvement in measurement repeatability of on-wafer measurement with the precision probing technique developed in the chapter 2. First, this chapter demonstrates an uncertainty analysis method for on-wafer S-parameter measurement with TRL calibration to determine the major uncertainty contributors in the measurements. The theories and algorithm of the uncertainty analysis are presented in section 3.2. Next, the analysis is demonstrated to show the dominant uncertainty contributor in section 3.3. Improvement of measurement repeatability was demonstrated in section 3.4 and 3.5. Finally, the findings in this chapter are summarized in section 3.6. The detail of the technique is provided in "Invited paper I: IEICE Trans. Electron., J102-C No.6, (2019).", "Paper III: IEICE Trans. Electron. Express, 16 3, (2019)", "Paper IV: IEEE Trans. Inst. Meas., 68 6, (2019).", "Conference paper III: CPEM 2018 Conf. Dig., (2018)", "Conference paper IV: 92nd ARFTG Conf. Dig., (2019)", and "Conference paper V: 91st ARFTG Conf. Dig., (2018)".

3.2   Development of uncertainty analysis algorithm

3.2.1   Monte-Carlo calculation

Monte-Carlo calculation is commonly used for uncertainty analysis of VNA system in coaxial measurement [106,115]. In the calculation, some variables are distributed in certain range (i.e. estimated standard deviation of the variables) by using random number.

Since distributed function can be obtained by the calculation, the possible range of a function can be estimated by the calculation.

3.2.2 Calculation procedures

A comprehensive uncertainty analysis algorithm for on-wafer measurement was established by using Monte-Carlo method. In calibration process, the error terms are calculated from measured S-parameter of standards without any error-correction. Using the error terms, measured S-parameter of DUT with error-correction is extracted. Figure 3.1 shows brief calculation flow in uncertainty analysis. In use of the developed uncertainty analysis algorithm, contributions of each uncertainty contributor to S-parameter of standards was evaluated preliminary to the analysis. The evaluated impact is necessary to estimate a range of distribution of measured S-parameter of standards without any error-correction in calibration procedure. After that, TRL calibration was executed for 1000 times by using the distributed S-parameter data sets of standards ($S_{\text{STD,dist}}$). The distributed S-parameter of standards were generated by random numbers. The generated distribution was transferred to distribution of S-parameter data sets of DUT ($S_{\text{DUT,dist}}$) which is generated from distributed error terms data sets ($e_{\text{ij,dist}}$) through TRL calibration. Combined uncertainty was defined as the equation (1).

$$U_{\text{c}} = 2 \times \text{std}(S_{\text{DUT,dist}}) \qquad (1)$$

3.2.3 Evaluation of uncertainty sources

The analysis requires to evaluate impact of each uncertainty contributor preliminary to the analysis. Figure 3.2 shows a detail flow chart of the calculation process. The uncertainties caused by the system noise, non-linearity, drift, contact repeatability of probe, and the reference data used in the calibration standards, are investigated to find dominant uncertainty contributor. The uncertainty associated with the stability of the test

port cables was not examined because the cables were almost immobile throughout the measurement process. Although the analysis algorithm was based on EURAMET guideline for VNA measurement [111], the calculations were modified to fit for on-wafer measurement.

According to Supplemental, reference data of calibration standards in TRL calibration are based on dimension of calibration standard. Hence, variation in dimension of the TRL standards were evaluated by dimensional measurement. An optical microscope, Keyence VHX-5000, was used for evaluation of in-plane dimensional measurement. Thickness of the substrate was evaluated by micrometer. Thickness of the fabricated pattern was measured by laser interference measurement system by Keyence LT9010M. Before the measurements, each equipment was calibrated by the calibrated block gage and the height gage. The system noise was evaluated by repeating 5 of the measurements without releasing the probes from the standard in short time. Maximum deviation in 5 of the S-parameter data sets was calculated in each measured frequency point, and treat it as the contribution of the system noise. The system drift was evaluated by continuing the measurements without releasing the probes from the standard for 5 hours. Maximum deviation in the S-parameter data sets was calculated in each measured frequency point, and treat it as the contribution of the system drift. The system linearity was evaluated by using known-attenuator according to the EURAMET guideline. The 5 dB stepped attenuator, 84908M by Keysight technologies, was utilized for the evaluation.

Last, contribution of connection repeatability, which is key feature of the developed uncertainty analysis algorithm, was investigated. The contribution is generally evaluated by evaluating variation of measured S-parameter with rotating connector in coaxial system. Instead, variation in probe position in X-, Y-, and Z- axes, tilt, and rotation angle were evaluated to investigate on contribution of connection repeatability in on-wafer measurement. Figure 3.3 shows the definition of the axes. Impacts of the differences in

probe position along to each axis was evaluated by evaluating maximum deviation in measured S-parameter of the standards with varying the probe's position in certain range. Figure 3.4 shows the illustrations of the probe moving in the evaluation process. The probe coordinate in X_p-, Y_p-, and Z-axes, and tilt angle, and rotation angle of the sample stage was varied in certain range for the evaluation. Table 3.1 shows the range of the variation in probe shifting along to each axis. The values in the table were determined by assuming possible variation in probe position in actual on-wafer measurement. Totally 11 of the measurements were conducted for the evaluation with changing the probe position. For instance, the probes were shifted along to X-axis from -5 µm to +5 µm with 1 µm step. Maximum deviation of standards was calculated from 11 of S-parameter data sets.

Table 3.1   Range of the variations in each axis

Contributors	Range
X-axis	±5 µm
Y-axis	±5 µm
Z-axis	±10 µm
Probe distance	±10 µm
Tilt angle	±1.0 deg
Stage rotation	±0.1 deg

Finally, the evaluated each contribution was used to generate distributed S-parameter of standards as described in the section 3.2.2.

3.3   Demonstration of the uncertainty analysis

3.3.1   Methodology

Same probe station and ISS with Chapter 2 were used in this chapter. To focus on uncertainty contributor in TRL calibration process, a single set of raw data of a 75 Ω

mismatched line device was used for all processes to avoid any disturbance caused by measurements of the device. Preliminary to the analysis, each contribution was evaluated for every standard. Table 3.2 shows measurement systems and conditions. In this study, contributions of probe positional error in X_p-, Y_p-, Z- axes, and probe distance were summarized as "CR-XYZ", those of probe tilt and rotation were summarized as "CR-TR".

Table 3.2   Measurement system and conditions

Items	Components and conditions
Probe station	AIST full-auto prober
RF probes	Infinity-GSG-150
ISS	AIST original
VNA system	N5260-016
Frequency range	10 MHz–110 GHz
Measured points	201
IF band width	10 Hz
Source power	-17 dBm

3.3.2   Uncertainty for measured S-parameter

Figures 3.5 shows the contribution of each uncertainty contributor to the calculated S-parameter of the 75 Ω mismatched line at 100 GHz. As shown in the figure, "CR-XYZ" was considered as the most dominant uncertainty contributor. System drift also gives large contribution because of the temperature sensitivity of the frequency extender which is discussed in reference [116]. In this study, a new technique to decrease the probe positional error in the X_p-, Y_p-, and Z- axes should be established for more accurate on-wafer measurement system.

3.4   Improvement of measurement repeatability

3.4.1   Measurement system and evaluation procedures

The original probe station in the Chapter 2 was also used in this chapter. The components of the measurement system and the measurement conditions are listed in Table 3.3 and Table 3.4.

Table 3.3　　　Measurement system and conditions for 100 GHz band.

Items	Components and conditions
Probe station	AIST full-auto prober
RF probes	Infinity-GSG-150
ISS	AIST original
VNA system	N5260-016
Frequency range	10 MHz–110 GHz
Measured point	201
IF band width	10 Hz

Table 3.4　　　Measurement system and conditions for 300 GHz band.

Items	Components and conditions
RF probes	Infinity-GSG-75
VNA	N5222B
Frequency extender	V03VNA2-T/R
Frequency range	190 GHz–340 GHz
Measured points	201
IF band width	100 Hz

An ISS described in the previous chapter 2 was used in this chapter, too. The measurement repeatability was compared between the precision probing technique and the conventional manual technique. Figure 3.6 shows a procedure for the investigation. First, standard coordinates in X-, Y-, and Z- axes were defined at the alignment patterns by both techniques. After that, the probes approached 1 mm from the alignment patterns and then made probes contact on the devices, then TRL calibration was performed (Figure 3.7). Thereafter, verification devices were evaluated. This procedure was repeated for 4 times to obtain 4 data sets for both techniques. The measurement reproducibility was evaluated by the equation (2), where "std" means standard deviation.

$$\delta S_{ij} = \sqrt{\text{std}\big(\text{Re}(S_{ij})\big)^2 + \text{std}\big(\text{Im}(S_{ij})\big)^2} \qquad\qquad (2)$$

3.4.2 Verification devices on ISS

The verification devices include 50 Ω matched and 75 Ω mismatched transmission lines, 10 dB attenuator (Figure 3.8). Lengths of the verification devices were 2 mm. All of the verification devices were fabricated on the ISS. Hence, the calibration quality was verified without replacing the substrate.

3.4.3 Screen-printed devices

Screen-printed transmission lines were prepared by using a handheld printer ZT320 (Tokyo process service). The fabrication conditions are summarized in Table 3.5. The as-printed 5250 μm transmission line was heated in air oven for 30 min at 130 °C, and then it was annealed in an inert oven for 1 h at 600 °C. Figure 3.9 shows a screen-printed transmission line.

Table 3.5　　Conditions for fabrication of screen-printed devices.

Items	Components and conditions
Ag paste	CA-T31(Daikin)
Average grain size	0.3 μm
Viscosity of the paste	310 Pa· s
Thickness of emulsion layer	7 μm
Squeezing speed	100 mm/s
Mesh count	730 mesh
Thickness of emulsion layer	7 μm

Table 3.6 shows dimensions of the screen-printed transmission line. Each dimension was defined as shown in figure 1.5(b).

Table 3.6 Dimension of the transmission line

Parameters		Values
Surface roughness	R_q	30 nm
Width of signal line	W	50 μm
Width of slit	s	25 μm
Thickness of the metallization	t	2 μm
Distance between outer edge of ground conductor	W_g	200 μm
Conductivity of metallization	h	250 μm

However, the screen-printed transmission lines do not have the alignment patterns at both sides of the transmission line. It is therefore, the adjustment was executed by using the device itself as shown in the figure 3.10. First, the pair of probes was roughly aligned at 35 μm from the open end of the transmission line. The reference Z-coordinates of the probes were defined at that point. Then, the probes were moved 50 μm in the opposite direction to align the probes out of the transmission line. After that, the reference X-coordinate was defined in same manner as was described in Chapter 2. Thus, the both probes were aligned at the edge of the CPW.

3.5   Improvement in measurement repeatability

3.5.1   Verification devices on ISS

Figure 3.11 and figure 3.12 show typical S_{ij} traces and δS_{ij} of the 75 Ω transmission line by the precision probing technique and the conventional manual technique. The precision probing technique demonstrated higher measurement reproducibility than that of the conventional manual probing technique. Since the precision probing technique improved the repeatability of the distance between probes, the evaluated S-parameter was more stable. However, the technique exhibited larger ripples in the reflection coefficient

and greater discontinuities in the transmission coefficient at 67 GHz. These may relate to the system drift of the frequency extender [116]. Despite the system drift problem, the precision probing technique can improve the measurement reproducibility by reducing the variations in the probe position. Figure 3.13 and figure 3.14 show typical S_{ij} traces and δS_{ij} of the 10-dB attenuator measured by the both techniques. As shown in the figure, measurement repeatability was improved even in the attenuator device. These results illustrate importance of the probe position in on-wafer S-parameter measurement.

Measurement repeatability was also investigated in the frequencies range up to 340 GHz. However, manual operation was not executed in this experiment to avoid giving damage to expensive RF probes and transmission lines for 300 GHz band. Instead, probe skating distance was varied from 15 μm to 25 μm. Measurement with 25 μm skating was repeated for 4 time to estimate measurement repeatability by using the equation (2). Then, impact of probe skating distance (ΔS_{ij}) was defined by an equation (3), where "AVE" means an average value. As described in the chapter 1, variation in probe position can reach to 10 μm in the conventional manual technique. It is therefore, ΔS_{ij} represents variation in S-parameter with the manual probing technique.

$$\Delta S_{ij} = \sqrt{\left[\mathrm{Re}(S_{ij,15\mu m}) - \mathrm{AVE}\{\mathrm{Re}(S_{ij,25\mu m})\}\right]^2 + \left[\mathrm{Im}(S_{ij,15\mu m}) - \mathrm{AVE}\{\mathrm{Im}(S_{ij,25\mu m})\}\right]^2} \qquad (3)$$

Figure 3.15 and figure 3.16 show typical S_{ij} traces and comparison of δS_{ij} and ΔS_{ij} of the 50 Ω matched transmission line. As shown in the figures, δS_{ij} was smaller than ΔS_{ij} in the both of reflection and transmission coefficients. This indicates the precision probing technique improves measurement repeatability even in the 300 GHz band. Ripple-like traces of ΔS_{ij} was associated with original S-parameter of the transmission line.

3.5.2   Screen-printed transmission lines

Figure 3.17 and figure 3.18 show typical S_{ij} traces and comparison of δS_{ij} between the precision probing technique and the conventional manual technique. The precision probing technique demonstrated higher measurement reproducibility than that of the conventional manual probing technique.

Owing to its simple mechanism, the precision probing technique can be used for various devices, including a screen-printed device. Its versatility is also a superior feature of the precision probing technique.

3.6 Conclusion of chapter 3

Measurement repeatability was compared between the conventional manual probing technique and the precision probing technique. The techniques can realize a repeatable determination of the probe contact position. The results are summarized below:

1) Uncertainty analysis algorithm for on-wafer TRL calibration was developed to find a dominant uncertainty contributor in the calibration process. The developed algorithm can calculate the contribution of probe position along to each axis.

2) The analysis results show that probe position along to X_p-, Y_p-, and Z-axes was a dominant uncertainty contributor in S-parameter measurement with TRL calibration process.

3) The proposed technique improved the measurement repeatability in evaluation of the transmission lines and the attenuator. This indicates that the precision probing technique can be applied for measurement of various devices.

4) Mechanism of the precision probing technique is so simple that it can realize universal use for various devices include the screen-printed device.

5) The precision probing technique can be used not only in the 100 GHz band, but also in the 300 GHz band.

3.7   Reference

[115]   J. P. Hoffman, P. Leuchtmann, J. Schaub, and R. Vahldiech, "Computing uncertainties of S-parameters by means of Monte Carlo Simulation," in 69th. ARFTG Conf. Dig., 2007, pp. 1–7.

[116]   J. P. Hoffman, "Temperature control of waveguide extenders," in CPEM 2016 Conf. Dig., 2016, pp. 1–2.
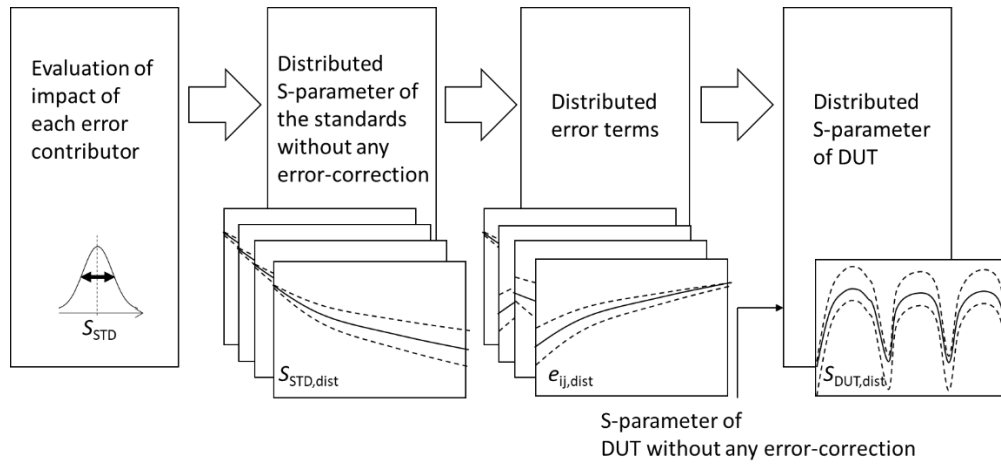
Figure 3.1   Brief flow chart of uncertainty analysis.
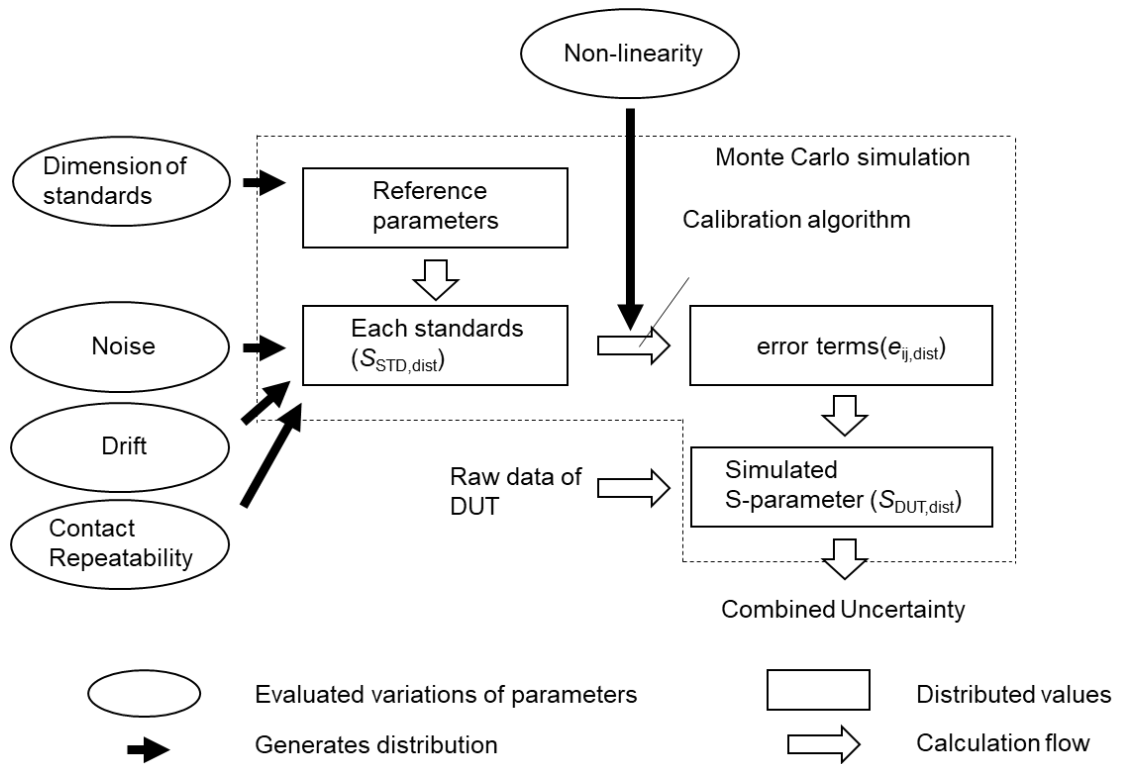
Figure 3.2   Flow chart of the Monte-Carlo calculation.
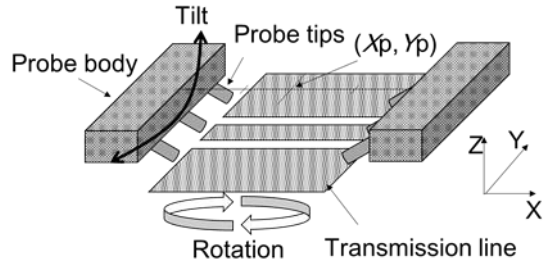
Figure 3.3   Definition of the axes of probe
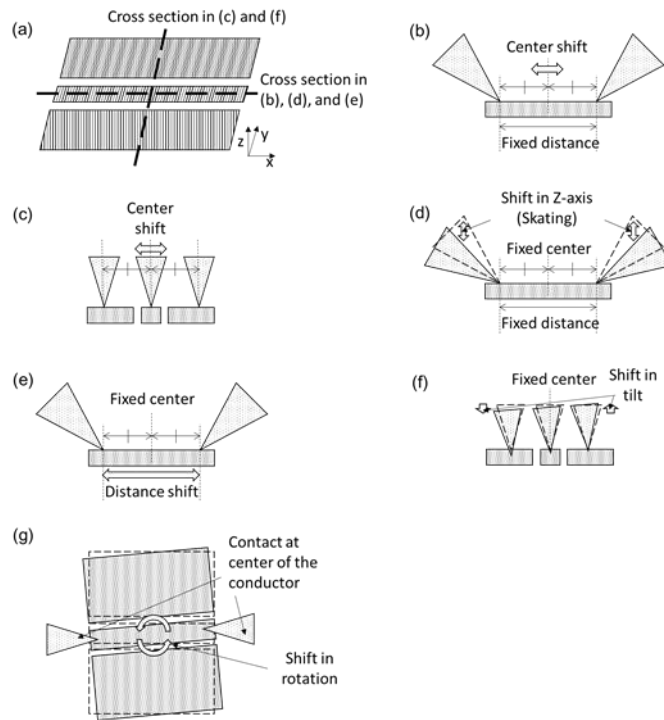
Figure 3.4   Schematic illustrations to explain uncertainty contribution of contact repeatability of probe.
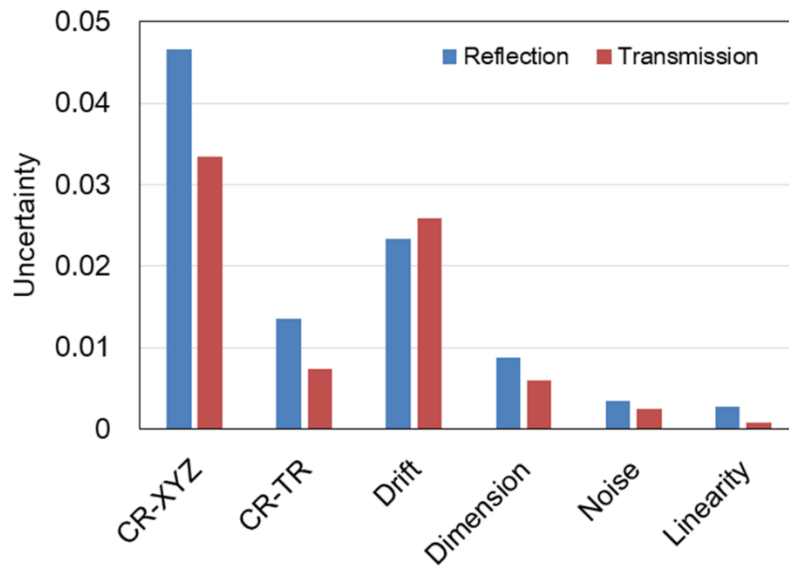
Figure 3.5   Uncertainty of the S-parameter of a 75 Ω transmission line for each contributor at 100 GHz.
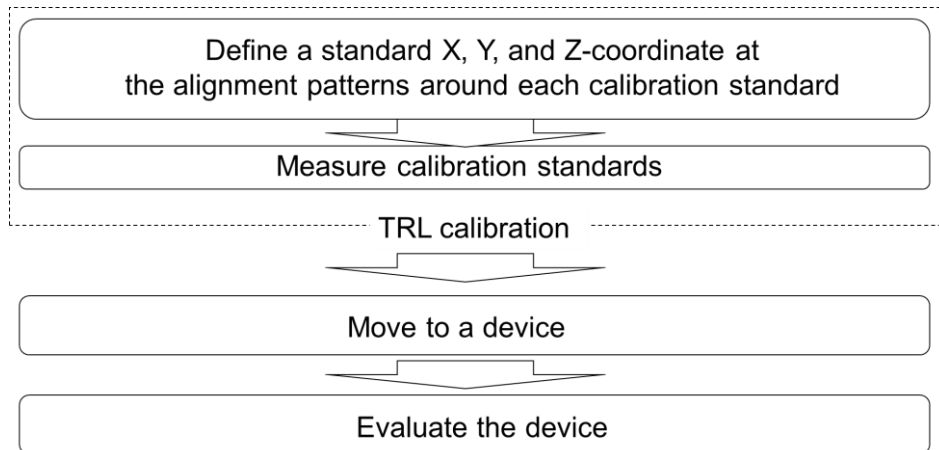
Fig. 3.6 Procedure for the investigation on improvement in measurement
repeatability.
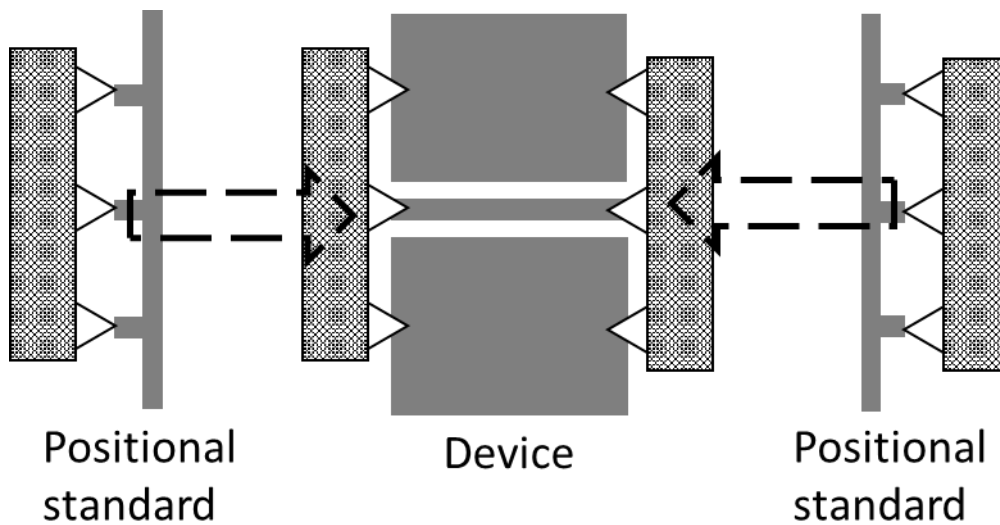
Fig. 3.7 Illustration of procedure to align probes on device.
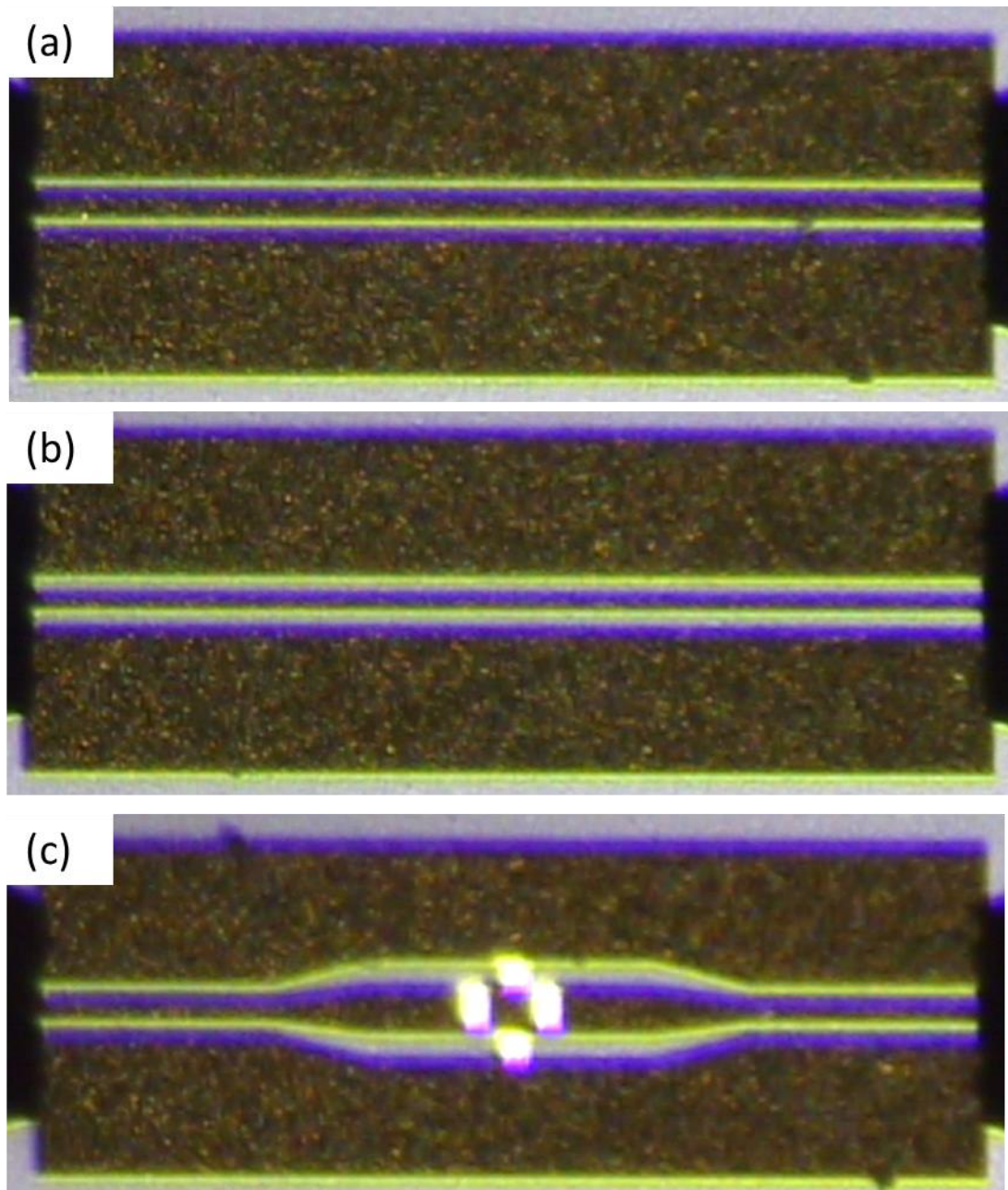
Fig. 3.8 Image of the devices. (a) 50 Ω matched line, (b) 75 Ω mismatched line, and (b) 10 dB attenuator.
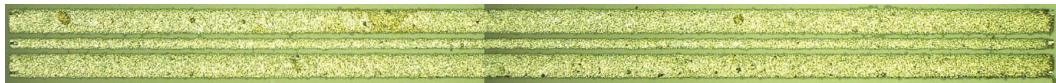
Fig. 3.9 Image of the 5.25 mm screen-printed transmission line.

(a)

(b)

Probe body

Gradual shift

Probe tip

Gradual shift down

Reference coordinate on X-axis

CPW device

Reference coordinate on Z-axis

Substrate
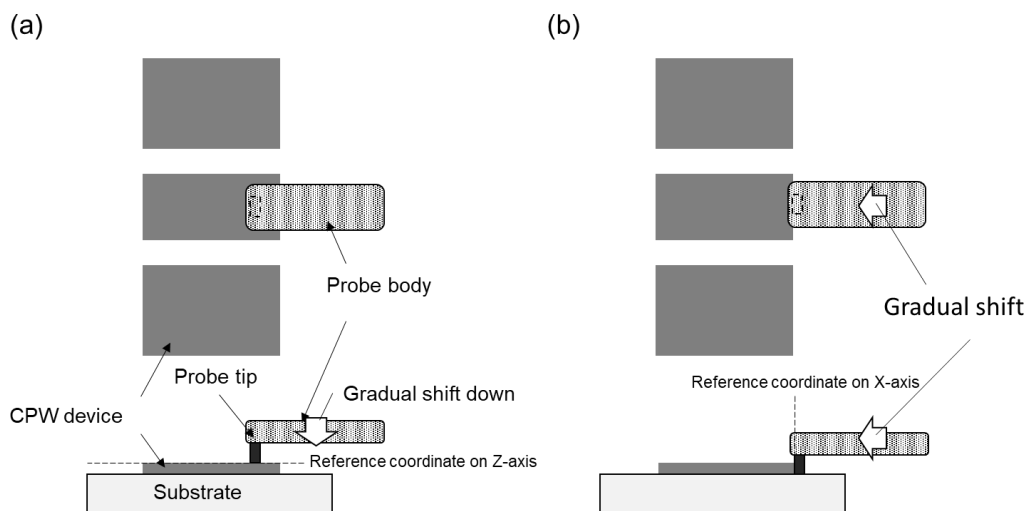
Fig 3.10 Illustrations of probing procedure of the adjustment. (a) Definition of standard coordinate in Z-direction, (b) that in X-direction.
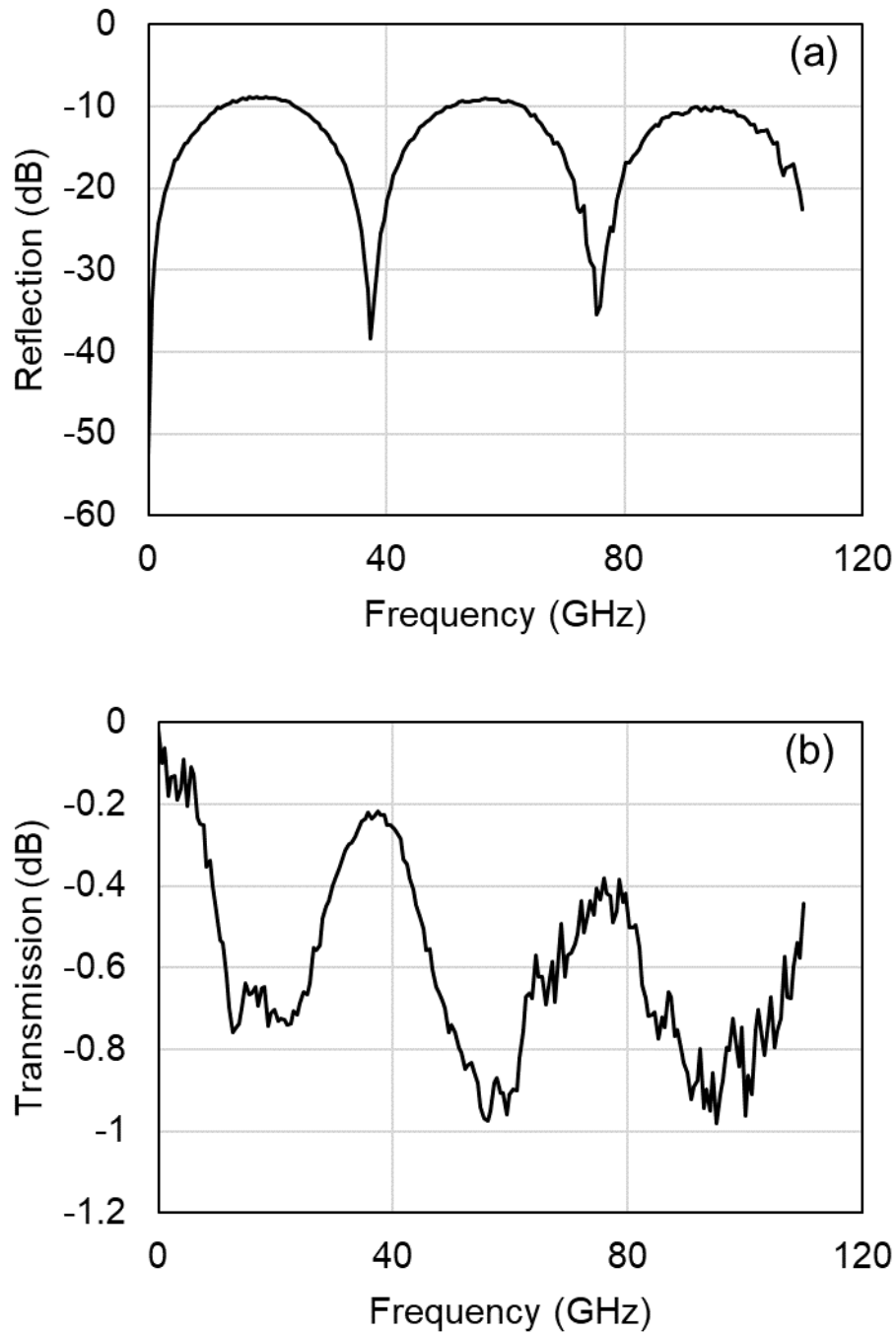
Figure 3.11   Typical S_{ij} traces of a 75 Ω transmission line. (a) Reflection coefficient
and (b) transmission coefficient.
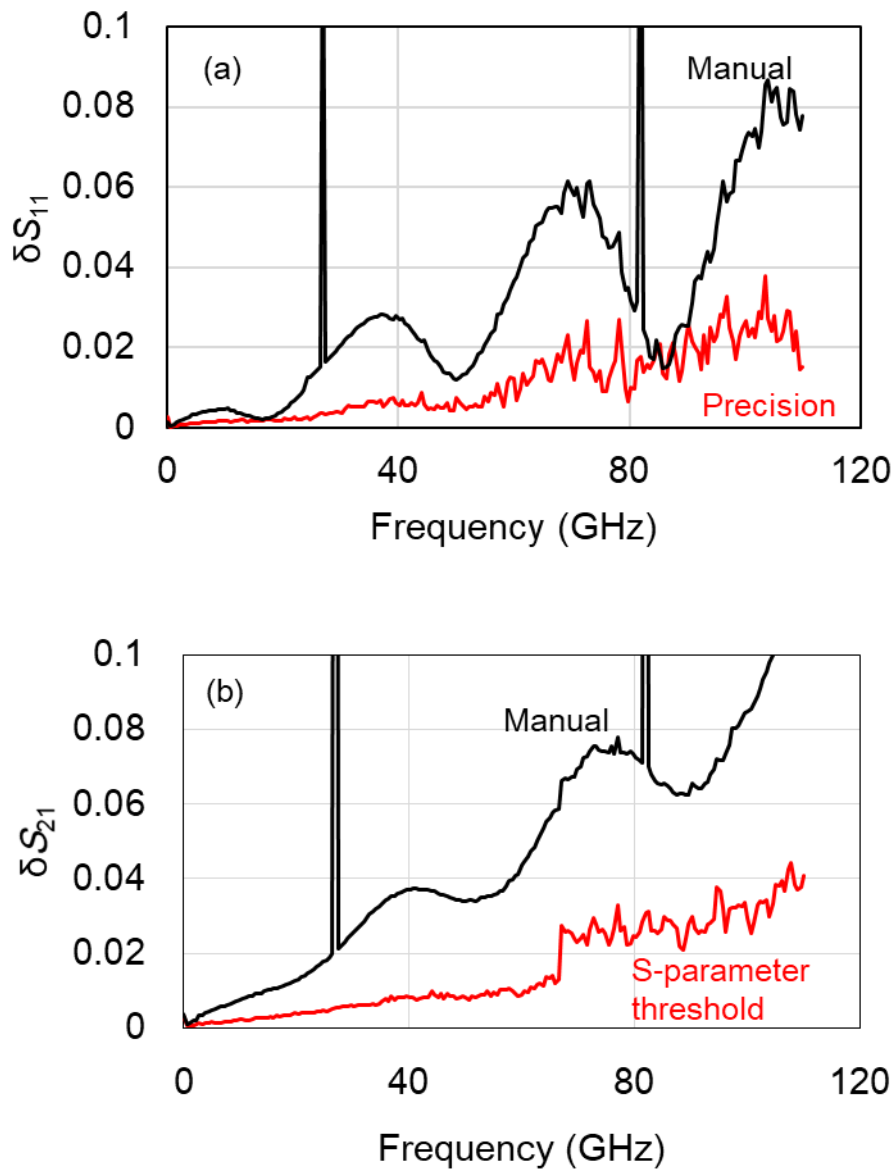
Figure 3.12   Comparison of the measurement reproducibility of the 75 ohms transmission line between the proposed technique and the conventional manual probing technique. (a) Reflection coefficient and (b) transmission coefficient.
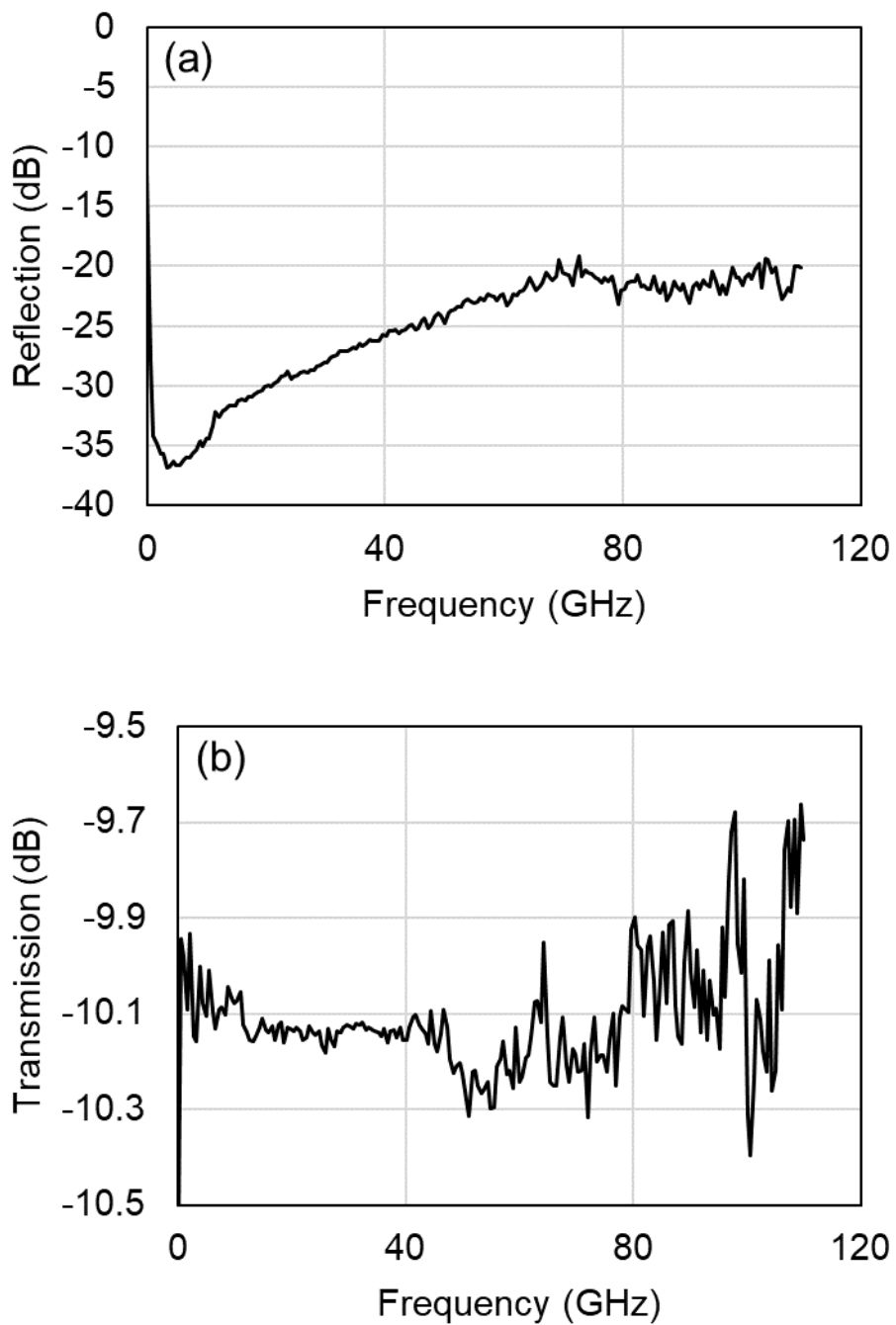
Figure 3.13   Typical S_{ij} traces of a 10 dB attenuator. (a) Reflection coefficient and (b) transmission coefficient.
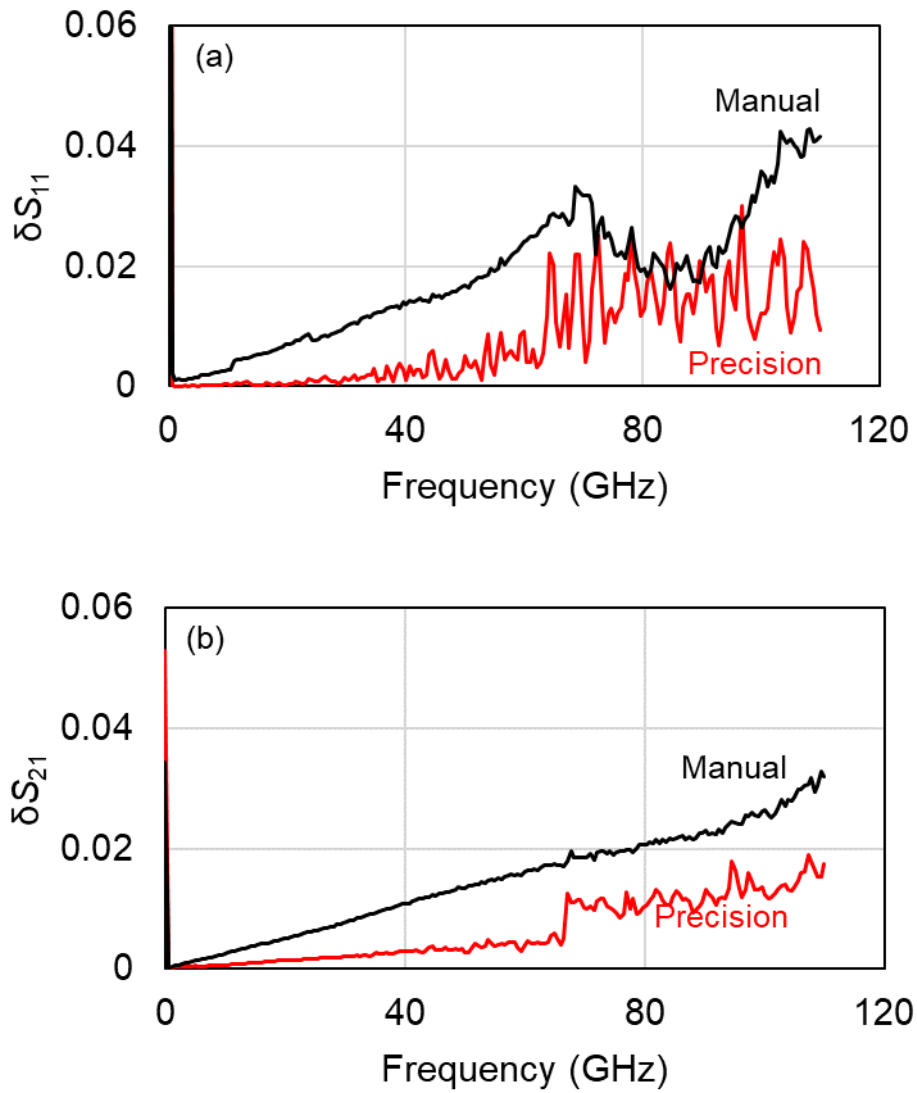
Figure 3.14   Comparison of the measurement reproducibility of the 10 dB attenuator between the proposed technique and the conventional manual probing technique. (a) Reflection coefficient and (b) transmission coefficient.
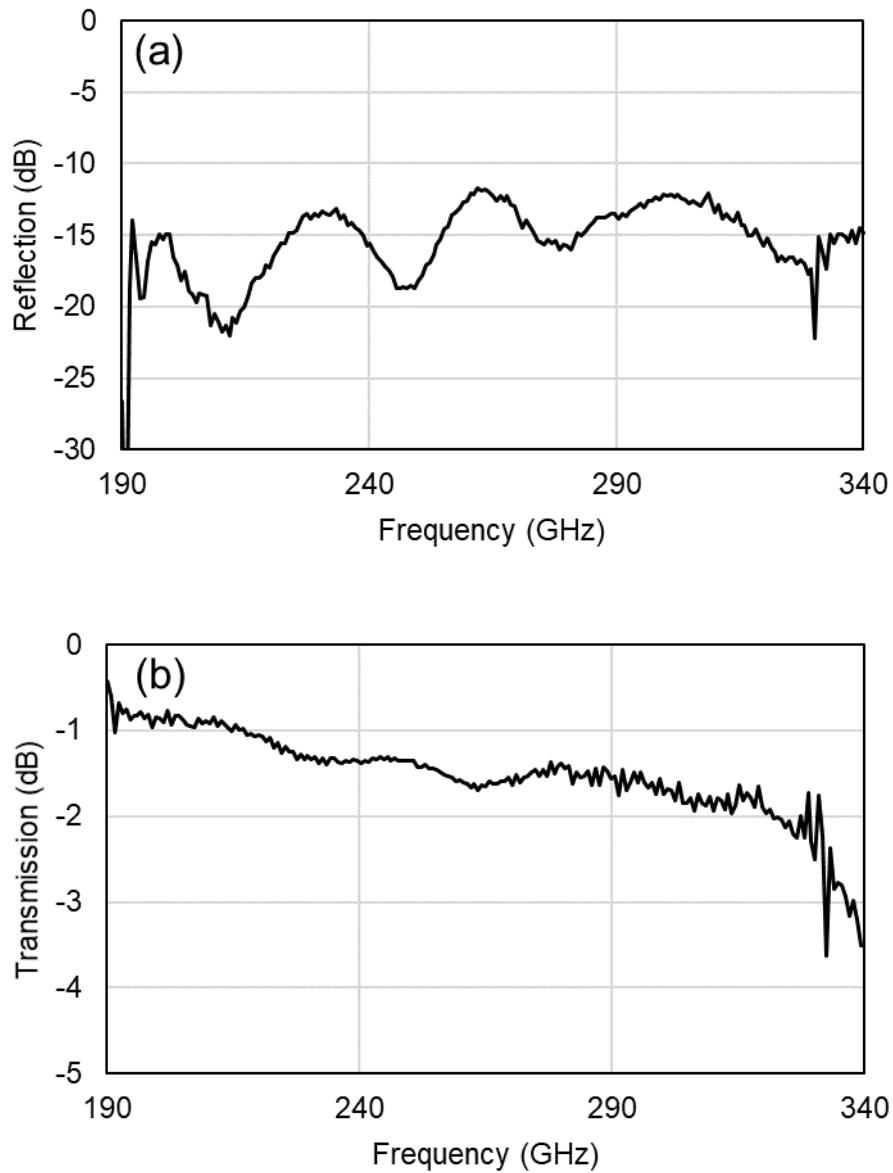
Figure 3.15   Typical S_{ij} traces of a matched transmission line in the 300 GHz band. (a) Reflection coefficient and (b) transmission coefficient.
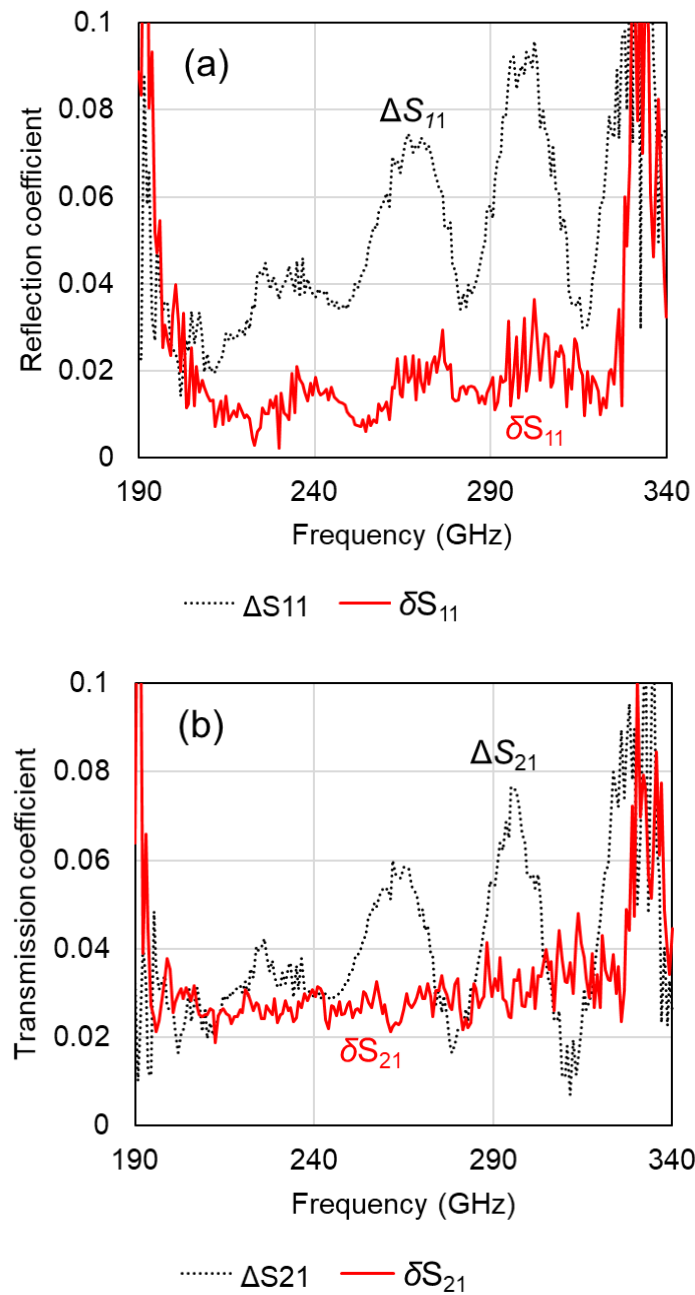
Figure 3.16   Comparison of the measurement reproducibility between the proposed technique and the conventional manual probing technique. (a) Reflection coefficient and (b) transmission coefficient.
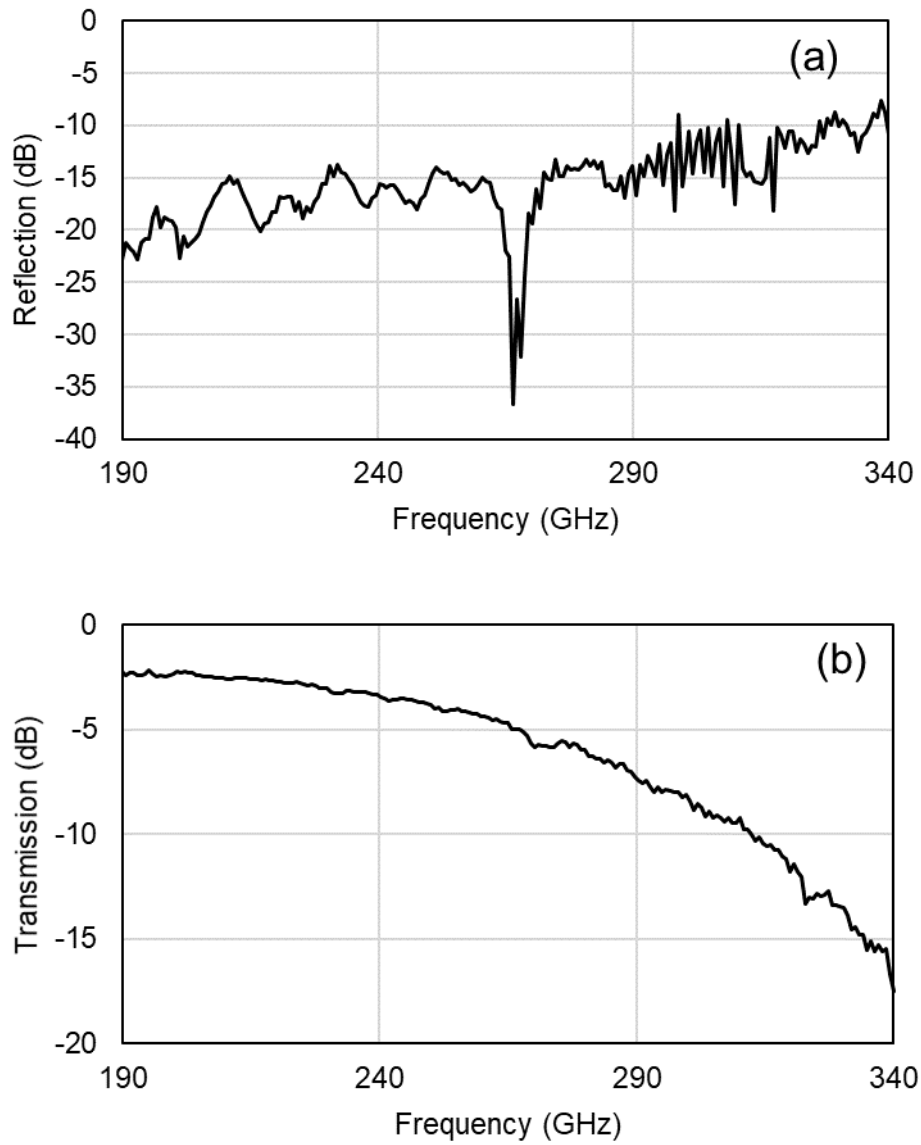
Figure 3.17   Typical S_{ij} traces of a printed-matched transmission line in the 300 GHz band. (a) Reflection coefficient and (b) transmission coefficient.
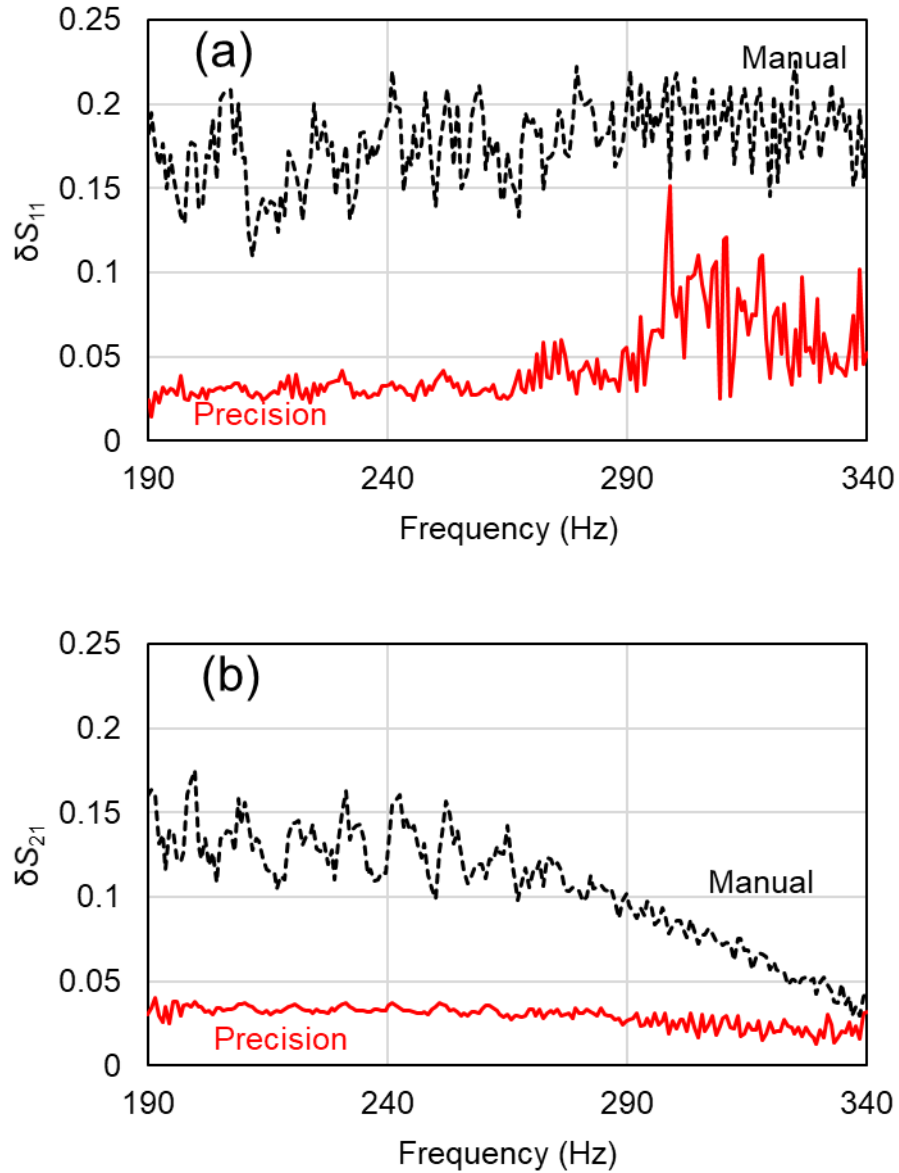
Figure 3.18   Comparison of the measurement reproducibility of the screen-printed transmission line between the proposed technique and the conventional manual probing technique. (a) Reflection coefficient and (b) transmission coefficient.

# Chapter 4   Proposal of new dielectric measurement method up to 300 GHz

4.1   Contents of chapter 4

This chapter demonstrates dielectric measurement by the PBR methods. This chapter first reviews the theory for determination of dielectric permittivity and dielectric loss tangent, and then demonstrates the measurement technique in the frequency range up to 340 GHz. Further, accuracy of the measurement and the applicable range of the technique were discussed. The detail of the technique is provided in "Paper V: Jap. J. Appl. Phys., in print." and "Conference paper VI: FMA 2019, (2019)".

4.2   Measurement principle of probe-backside reflection method

4.2.1   Dielectric permittivity

Figure 4.1(a) shows a brief illustration of T-junction resonator. The resonant frequency of the T-junction resonator f_r is determined by length of notch-line L_{notch} according to an equation (1), where c_0 is speed of light. Length of the notch-line L_{notch} should be corresponded to a quarter of electrical wave-length at a lowest resonant frequency. RF signal at output side of the line show destructive interference, thus resonance is observed in certain frequency as shown in the figure.

$$f_r = \frac{c_0}{4L_{notch}} \tag{1}$$

Figure 4.1(b) shows a schematic illustration of the principle of the proposed technique. A pair of probes and a transmission line are required for the measurement. One of the probes is contacted at the edge of the transmission line, and the other probe is contacted at middle of the transmission line. In this case, the transmission line at back side of the probe is behaved as a notch-line of the T-junction resonator. As described in the previous chapter, a T-junction resonator can be used for material characterization. Thus, the procedure of the calculation was constructed according to the way in T-junction resonator.

Effective dielectric permittivity can be calculated by using the equations (2) – (4), where n means a number of the nth resonance.

$$\lambda_r = \frac{c_0}{f_r} \tag{2}$$

$$L_e = \frac{2n-1}{4}\lambda_r \tag{3}$$

$$\varepsilon_{eff} = \left(\frac{L_e}{L_p}\right)^2 \tag{4}$$

However, the equations have some difficulties to be applied for the material characterization at millimeter-wave frequency. First, an open end of notch-line is electrically enlarged by "edge effect" due to fringing field as shown in equations (5)-(7).

$$L_{e,eval} = L_{e,eff} = L_e + \Delta L \tag{5}$$

where

$$\Delta L = \frac{C_L Z_L c_0}{\sqrt{\varepsilon_{r,eff}}} \tag{6}$$

Hence, Eq. (4) is rewritten as Eq. (7).

$$\varepsilon_{eff,eval} = \left(\frac{L_e + \Delta L}{L_p}\right)^2 = \varepsilon_{eff} + \Delta\varepsilon \tag{7}$$

This enlargement ΔL is hard to estimate because dielectric constant itself is one of the variables. Furthermore, radiation of a transmission line is not negligible at mmW

frequency. Thus, the proposed technique utilizes two of the measurements, and take difference between the measurements to address these problems. Basic of the method is also used for the open-ended strip-line method. In the method, an open-ended transmission line whose length is adequately long is used for the first measurement. After the measurement, the transmission line is cut down, then the second measurement is executed. Dielectric permittivity can be calculated by using difference in the length of transmission lines and the resonant frequencies of the open-ended transmission line. On the other hand, the proposed technique does not require to cut down a transmission line, but length of the quasi-resonator is easily changed by just shifting of probe's contact position. Thus, the quasi-resonator behaves as great flexibility in adjustment of its length, unlike conventional resonators. Furthermore, accuracy in positioning of a mechanical stage is generally no more than several microns, which is much better than working accuracy in fabrication of conventional resonators which sometimes reaches to several hundred microns. It is therefore accuracy improvement in size of resonator is expected by using the proposed technique. According to above mentioned considerations, dielectric permittivity can be calculated by using the modified equations (8) – (11).

$$\lambda_{\text{r,eval,m}} = \frac{c_0}{f_{\text{r,eval,m}}} \tag{8}$$

$$L_{\text{e,eval,m}} = \frac{2n-1}{4}\lambda_{\text{r,eval,m}} \tag{9}$$

$$\varepsilon_{\text{eff,mod}} = \left(\frac{\left(L_{\text{e,m+1}} + \Delta L\right) - \left(L_{\text{e,m}} + \Delta L\right)}{L_{\text{p,m+1}} - L_{\text{p,m}}}\right)^2 = \left(\frac{\Delta L_{\text{e,eval,m}}}{\Delta L_{\text{p,m}}}\right)^2 \tag{10}$$

$$f_{\text{r,m}} = \frac{f_{\text{r,eval,m+1}} + f_{\text{r,eval,m}}}{2} \tag{11}$$

The dielectric permittivity was calculated using equations (12) – (15).

$$\varepsilon_r = 2(\varepsilon_{\text{eff,mod}} - 1) \frac{\frac{K(k'_1)}{K(k_1)} - \frac{t}{d - W}}{\frac{K(k'_2)}{K(k_2)}} \tag{12}$$

$$k_1 = \frac{W_{\text{tot}}}{d} \sqrt{\frac{d^2 - W^2}{W_{\text{tot}}^2 - W^2}} \tag{13}$$

$$k_2 = \frac{\sinh(\pi W_{\text{tot}}/4h)}{\sinh(\pi d/4h)} \sqrt{\frac{\sinh^2(\pi d/4h) - \sinh^2(\pi W/4h)}{\sinh^2(\pi W_{\text{tot}}/4h) - \sinh^2(\pi W/4h)}} \tag{14}$$

$$k'_n = \sqrt{1 - k_n^2} \quad \text{(n=1,2)} \tag{15}$$

4.2.2 Dielectric loss tangent

The loss of a transmission line σ_{line} and quality factor Q_{line} are expressed by equations (16) and (17), where subscripts "c", "ε_r", "r", and "m" indicate the conductivity loss, dielectric loss, radiation loss, and magnetic loss, respectively.

$$\sigma_{\text{line}} = \sigma_c + \sigma_{\varepsilon r} + \sigma_r + \sigma_m \tag{16}$$

$$\frac{1}{Q_{\text{line}}} = \frac{1}{Q_c} + \frac{1}{Q_{\varepsilon r}} + \frac{1}{Q_r} + \frac{1}{Q_m} \tag{17}$$

The quality factor of the magnetic loss Q_m is considered negligible in this study, because non-ferromagnetic material is used.

As Q_{line} can be calculated from the 3-dB bandwidth, $Q_{\varepsilon r}$ can be obtained if Q_c and Q_r are negligibly small. However, impacts of these quality factors cannot be neglected in the PBR technique. Therefore, the contribution of $Q_{\varepsilon r}$ should be extracted from measured Q_{line}. In this study, contribution of the dielectric loss was extracted by using the well-known transmission line theory, which was proposed by W. Heinrich [117]. W. Heinrich expressed resistance R, inductance L, conductance G, and capacitance C of a transmission line in the mmW frequency range up to 100 GHz. However, modifications are required to extend the theory toward the 300-GHz band. In this study, dielectric dispersion, radiation, and surface roughness were considered to extract the dielectric

loss contribution. The transmission line theory assumes that there is a difference in skin effects between the signal and ground lines of a CPW. Frequency-dependent expressions of $R(f)$, $L(f)$, $G(f)$, and $C(f)$ are established to make the calculation result agree with the data from the mode-matching analysis [118,119]. Several studies extended the theory to sub-mmW frequencies [120-123]. Each of these studies proposes a different expression for a transmission line; thus, the most suitable expressions were selected for the PBR method.

According to Ref. 119, G and C of a transmission line can be expressed as:

$$C = 2\varepsilon_0 \left(F_{up}(w, s, t, w_g) + \varepsilon_r F_{low}(w, s, t, w_g) \right) \tag{18}$$

$$G = 2\omega\varepsilon_0\varepsilon_r \tan\delta F_{low}(w, s, t, w_g) \tag{19}$$

where w is the width of the signal line, t is the thickness of metallization, s is the width of the slot between the signal line and ground line, and w_g is the width of the ground line. The line resistance R is defined as a sum of the signal line resistance R_c and ground line resistance R_g ($R = R_c + R_g$). The frequency range is divided into three ranges because of the different current distributions in the signal and ground lines, which strongly depend on the frequency. In the highest frequency range, the current distribution is determined by the classical skin effect. On the other hand, the current distribution is uniform in the lowest frequency range. In the intermediate range, the line resistance is expressed using the fitting parameters, which provide the agreement of the calculation results with the mode-matching analysis. R_c and R_g are defined in each frequency range as:

$$R_c = R_{c0}\left[1 + a_1^c\left(\frac{\omega}{\omega_{c1}}\right)^2\right] \text{ (for } \omega \leq \omega_{c1}) \tag{20}$$

$$R_c = R_{c1}\left(\frac{\omega}{\omega_{c1}}\right)^{\nu_c}\left[1 + a_2^c\left(\frac{\omega_{c1}}{\omega}\right)^2 + a_3^c\left(\frac{\omega}{\omega_{c2}}\right)^2\right] \tag{21}$$
$$\text{(for } \omega_{c1} \leq \omega \leq \omega_{c2})$$

$$R_c = \sqrt{\frac{\omega\mu_0}{2\kappa}}\frac{F_L^c}{4F_0^2}\left[1 + a_4^c\left(\frac{\omega_{c2}}{\omega}\right)^2\right] \text{ (for } \omega_{c2} \leq \omega) \tag{22}$$

$$R_g = R_{g0} \left[1 + a_1^g \left(\frac{\omega}{\omega_{g1}} \right)^2 \right] \; (for \; \omega \le \omega_{g1}) \tag{23}$$

$$R_g = R_{g1} \left(\frac{\omega}{\omega_{g1}} \right)^{v_g} \left[1 + a_2^g \left(\frac{\omega_{g1}}{\omega} \right)^2 + a_3^g \left(\frac{\omega}{\omega_{g2}} \right)^2 \right] \tag{24}$$
$$(for \; \omega_{g1} \le \omega \le \omega_{g2})$$

$$R_g = \sqrt{\frac{\omega \mu_0}{2\kappa}} \frac{F_L^g}{4F_0^2} \left[1 + a_4^g \left(\frac{\omega_{g2}}{\omega} \right)^2 \right] \; (for \; \omega_{g2} \le \omega) \tag{25}$$

$$R = R_c + R_g \tag{26}$$

The frequency limits ω_{c1}, ω_{c2}, ω_{g1}, and ω_{g2}, depend on the conductivity of metallization κ, as well as on t, w, and w_g. The other coefficients, R_{c0}, R_{c1}, R_{g0}, R_{g1}, F_L^g, F_0, a_n^c, a_n^g ($n = 1 - 4$), v^c, and v^g, also depend on κ, t, w, s, and w_g. Thus, the line resistance R can be calculated from the circuit dimensions and conductivity of metallization.

For the line inductance L determination, the entire frequency range is divided into four parts. In the lowest frequency range, the current distribution is uniform in the both signal and ground lines. In the highest frequency range, skin effect has the dominant impact on the current distribution. In the intermediate range, the ground line exhibits non-uniform current distribution, while the signal line still exhibits uniform distribution. Such a non-uniform current distribution makes the line inductance expression in this range more complex.

$$L = L_{DC0} \left[1 + a_0^L \left(\frac{\omega}{\omega_{L0}} \right)^2 \right] \; (for \; \omega \le \omega_{L0}) \tag{27}$$

$$L = L_{e\infty} + L_{z1} \left(\frac{\omega}{\omega_{L1}} \right)^{v_{z1}} \left[1 + a_1^L \left(\frac{\omega_{L0}}{\omega} \right)^2 + a_2^L \left(\frac{\omega}{\omega_{L1}} \right)^2 \right] \tag{28}$$
$$(for \; \omega_{L0} \le \omega \le \omega_{L1})$$

$$L = L_{e\infty} + L_{z2} \left(\frac{\omega}{\omega_{L2}} \right)^{v_{z2}} \left[1 + a_3^L \left(\frac{\omega_{L1}}{\omega} \right)^2 + a_4^L \left(\frac{\omega}{\omega_{L2}} \right) \right] \tag{29}$$
$$(for \; \omega_{L1} \le \omega \le \omega_{L2})$$

$$L = L_{e\infty} + \sqrt{\frac{\mu_0}{2\omega\kappa}} \frac{F_L^c + F_L^g}{4F_0^2} \left[1 + a_5^c \left(\frac{\omega_{L2}}{\omega} \right) \right] \; (for \; \omega_{L2} \le \omega) \tag{30}$$

Similar to the line resistance, all the parameters, ω_{L0}, ω_{L1}, ω_{L2}, a_n^c (n = 1 − 5), F_L^g, F_L^g, F_0, v_{z1}, v_{z2}, L_{DC0}, L_{z1}, L_{z2}, and $L_{e\infty}$, are defined by the circuit dimensions and conductivity of metallization. Figure 4.2 shows the comparison of the calculated R and L in the reference and those of this study. As shown in the figure, these values agree well.

The influence of radiation was modeled in reference [120]. The impact of the radiation is estimated from the electrooptic (EO) measurements of the attenuation in voltage of the EM field just above the transmission line. The contribution of radiation for the line resistance R_{rad} can be expressed as:

$$R_{rad} = \left(\frac{\pi}{2}\right)^5 2 \frac{\left(1 - \frac{\varepsilon_{eff}(f)}{\varepsilon_r}\right)^2}{\sqrt{\frac{\varepsilon_{eff}(f)}{\varepsilon_r}}} \frac{(s + 2w)^2 \varepsilon_r^{1.5}}{c_0^3 K'(k)K(k)} f^3 \qquad (31)$$

$$K'(k) = K(\sqrt{1 - k^2}) \qquad (32)$$

where K is the elliptic integral of the first kind, k is a function of s and w, and c_0 is the speed of light. The line resistance can be modified by summing R_{rad} in (31) and R in (26).

Schneider introduced the dielectric dispersion considering the TE signal propagation [121]. Though ideal CPW based on quasi-TEM mode signal propagation, TE mode signal which assuming a rectangle waveguide of which long axis is side between both outer edges of the ground lines and short axis is thickness of a substrate should propagate on actual CPW. The effective dielectric permittivity can be modified as:

$$\varepsilon_{r,eff,new} = \varepsilon_{r,eff,qs}\left[1 + \left(\sqrt{\frac{\varepsilon_r}{\varepsilon_q}} - 1\right)p\left(\frac{f}{f_{g1}}\right)^2\right] \qquad (33)$$

$$p = \frac{2.86465\left(\frac{d}{w_{tot}}\right)^2}{0.15075 + \frac{d}{w_{tot}}} \qquad (34)$$

$$\varepsilon_q = \frac{1 + \varepsilon_r}{2} \tag{35}$$

where w_{tot} denotes the total width of the CPW, d denotes the ground-to-ground spacing, and f_{g1} corresponds to the frequency, at which the phase constants of the CPW mode and first lateral higher-order mode intersect. f_{g1} is a function of ε_r and w_{tot}. Thus, the line capacitance C in equation (18) was modified by using $\varepsilon_{r,eff,new}$.

The influence of the surface roughness was studied by G. Gold [122]. The surface of metallization was modeled by tiny stacked spheres in that study. The roughness influences on the effective conductivity σ_{eff} and effective permeability μ_{eff} as:

$$\sigma_{eff} = \frac{\omega}{8\mu_0{}^3} \left| B_y(0) \right|^4 \left[\int \frac{\left| J_{rough}(x) \right|^2}{2\sigma(x)} \, dx \right]^{-2} \tag{36}$$

$$\mu_{eff} = 2\mu_0 \sigma \omega \left| B_y(0) \right|^{-4} \left[\int \left| B_{y,rough} \right|^2 dx \right]^{2} \tag{37}$$

$$\sigma(x) = \sigma_{bulk} \frac{1}{R_q \sqrt{2\pi}} \int_{-\infty}^{x} e^{-\frac{u^2}{2R_q{}^2}} \, dx \tag{38}$$

where $B_y(x)$ denotes the magnetic field in the in-plane direction at the depth of x μm from the surface of the conductor, $J_{rough}(x)$ denotes the current density at the depth of x μm, $B_{y,rough}$ denotes the magnetic field around the rough surface, R_q denotes the root mean square of the surface roughness parameter, and σ_{bulk} denotes the conductivity of the bulk material. The calculated σ_{eff} and μ_{eff} were substituted into equations (22), (25), and (30) to take the effect of surface roughness on the calculation algorithm into account.

R, L, G, and C of a transmission line were calculated using the above-mentioned equations. A transmission line resonator can be modeled by the equivalent circuit shown in Figure 4.3. The quality factor of the resonator $Q_{line,fit}$ can be calculated by equations (39) – (41). The parameters for the fitting procedure are summarized in Table 4.1.

$$\frac{1}{Q_{\text{line}}} = \frac{1}{Q_{\text{L}}} + \frac{1}{Q_{\text{C}}} \tag{39}$$

$$Q_{\text{L}} = \frac{\omega L}{R} \tag{40}$$

$$Q_{\text{C}} = \frac{\omega C}{G} \tag{41}$$

Table 4.1 Parameters for the calculation

Parameters		Values
Surface roughness	R_{q}	30 nm
Width of signal line	w	50 μm
Width of slit	s	25 μm
Thickness of the metallization	t	2 μm
Distance between outer edge of ground conductor	w_{g}	200 μm
Permittivity	ε_{r}	9.8
Dielectric loss for the initial state	$\tan\delta$	1.25×10^{-4}
Conductivity of metallization	κ	56×10^{6} S· m

The dissipation factor $\tan\delta$ of a substrate material can be estimated by fitting $Q_{\text{line,fit}}$ to the value derived from the 3-dB bandwidth of the resonator $Q_{\text{line,3dB}}$. However, an additional modification was required to transform the theoretical equation to the form appropriate for actual measurements. As shown in figure 4.3, the calculation of $Q_{\text{line,fit}}$ assumes an ideal resonator. However, the quasi-resonator in the PBR method is considered as a non-ideal resonator. Evidently, the resonator has fringing EM field at the open end. Thus, the equivalent circuit of the resonator was modified as shown in figure 4.4; the modified circuit has an additional RC parallel circuit. Assuming the quality factor of this RC parallel circuit is Q_{c0}, equation (39) takes the form:

$$\frac{1}{Q_{\text{line}}} = \frac{1}{Q_{\text{L}}} + \frac{1}{Q_{\text{C}}} + \frac{1}{Q_{\text{c0}}} \tag{42}$$

Q_{c0} was determined from the known $\tan\delta$ value in microwave frequencies. According to reference [52], $\tan\delta$ of alumina is 1.25×10^{-4} at 30 GHz. Q_{line} measured by the PBR method was 42 at 30 GHz. Thus, Q_{c0} can be determined from equation (42).

Therefore, $\tan\delta$ can be determined at the other measured frequencies by fitting of Q_{line}, assuming Q_{c0} is insensitive to the measured frequency.

4.3 Improvement of measurement repeatability by using the precision probing technique

4.3.1 Measurement system and configurations

The dielectric measurement technique was demonstrated in the two frequency bands, which are referred to as "100-GHz band" and "300-GHz band" in this chapter. Table 4.1 shows the configurations of the measurement systems. The original probe station and ISS from Chapter 2 were used for the demonstration. Furthermore, two of the probe positioning techniques, the conventional manual inspection and precision probing technique described in Chapter 2, were demonstrated to show the improvement in the measurement repeatability. Regarding the precision probing technique, the same process to section 3.2.3 was used for the alignment of probe position, as shown in Figure 3.5 in the Chapter 3.

Table 4.1 System configurations

Frequency band	100 GHz	300 GHz
Measurement frequency	10 MHz-110 GHz	190 GHz- 340 GHz
VNA	E8361A	B5222B
Frequency extender	N5250A	V03VNA2-T/R
IF (Hz)	100	1000
Probe	Infinity-GSG-150	Infinity-GSG-75
ISS	101-190	138-356

4.3.2 Validation of the probe-backside reflection method

After the procedure described in section 4.3.1, one side of the probe was positioned to contact the end of the transmission line, while the other side of the probe did not contact the line. The uncontacted probe was shifted by 500 μm to align the probe in the middle of the transmission line. As the measured frequency range was limited by 110 GHz, no resonance was expected to be observed when the probe contact point was positioned at approximately 350 μm or less from the end of the transmission line. After that, the probe was shifted to 1500 μm from the end in 100-μm steps (Figure 4.5). The probe contacted the middle of the transmission line in each shift with the precision adjustment of the probe skating using the precision probing technique. The total of 10 S-parameter datasets were obtained in this process. Using equations (8) – (11), 9 dielectric permittivity can be calculated in the entire measured frequency range. The measurement was repeated 5 times to investigate the measurement repeatability.

4.3.3 Improvement of measurement repeatability by using the precision probing technique

Acquired scattering parameter was compared with that of calculated by EM simulation. Figure 4.6 shows the EM model for the simulation. The ground ring model was adopted for the modeling of the probe tip in this thesis. The ground ring model was reported as the optimal model for RF probe tips [124]. The dimensions of the ground ring were optimized by comparing the measurement result of the 2-mm-long matched transmission line. The size of the modeled probe tips was 20 μm. Figure 4.7 shows the comparison of the scattering parameters when the probe contact was positioned at 800 μm from the open end. The solid line indicates the measured S-parameter, and the dashed line indicates the simulated result. Although there is a slight difference in the resonant frequencies, the results show good agreement.

Figure 4.8 shows comparison of evaluated effective dielectric permittivity calculated by the equations (8) – (11). The error bars in the figure indicate single standard deviation of the evaluated dielectric permittivity. Range of the error bars was approximately 3-10 % with the conventional manual probing technique. Generally, this level of the error is out of acceptable range for dielectric measurement. It is reasonable that the variation of the permittivity reached to those level, because variation of the probe position reaches 10 μm despite difference in physical length of the quasi-resonator, which is associated with amount of the probe shifting, was only 100 μm. On the other hand, the precision probing technique exhibited obviously improved measurement repeatability. The error bars with the precision probing technique was no more than 1 % and 0.2 % in their best. This is considered as acceptable range because uncertainty of dielectric permittivity measurement is 3 % even in circular-disk resonator method, which is known as the precision dielectric measurement method [52]. It is therefore, measurement repeatability was considerably improved by the precision probing technique. Furthermore, the broken line in the figure shows reference value which was derived by phase of S_{21} of the two lines. The evaluated value in the proposed technique was 5.1, which was well-corresponded to the reference value. Therefore, accuracy of the proposed technique was also validated.

4.4   Demonstration of dielectric measurement method up to 300 GHz

4.4.1   Methodology of the demonstration

The screen-printed 5.25-mm matched transmission line was used for the demonstration. The substrate material was also alumina ceramics with the nominal dielectric permittivity of 9.8. As the improvement in the measurement repeatability was

already demonstrated in the 100-GHz band, only the precision probing technique was used for the measurements.

In the "100 GHz band", the one probe was shifted by 900 μm from the edge of transmission line to align the probe in the middle of the transmission line. After that, the probe was shifted to 500 μm from the end in 100-μm steps (Figure 4.9(a)). Only the 1st resonant frequency, which corresponded to a peak of n = 1, was utilized to calculate ε_{eff}.

The third and fourth order resonances (n = 3, 4) were used for the measurements in the 300 GHz band, because the other orders were out of the measurement frequency band. The probe contact point was positioned at 600 μm and 800 μm from the end for the third order resonance and at 700 μm and 1050 μm for the fourth order resonance (Figures 4.9(b) and 4.9(c)). The contact positions were selected to make the difference of the physical lengths of the resonators as large as possible for each order.

4.4.2   Investigation on accuracy of the measurement

Though effective dielectric permittivity of alumina substrate was evaluated as 5.1 in the previous chapter. Inconsistency between calculation theory and actual circuit behavior degrades accuracy in transformation from effective permittivity to dielectric permittivity of a substrate material. Non-ideal circuit design may cause the calculated dielectric permittivity being deviated from the true value. Thus, sensitivity analysis was executed for each dimension of transmission line. In conventional circuit fabrication technique, a Pd layer is fabricated between a substrate and a gold metallization for the adhesion of the metallization. However, this adhesion layer may cause the analysis more complex. To address the problem, a screen-printed transmission line was used, because the screen-printed line does not need an adhesion layer. The details of the screen-printed transmission line are described in the Chapter 3.

The measurement uncertainty was estimated at each resonant frequency. Table II and III shows lists of evaluated contributors and their uncertainties for dielectric permittivity and loss tangent at 50 GHz and 270 GHz. Impact of frequency dependence of Q_{c0}, accuracy of the circular-disk resonator, are additionally evaluated for $\tan\delta$. Frequency dependence of Q_{c0} was estimated by assuming that $Q_{c0}=\omega C_m/G_m$. Variation of Q_{c0} with varied frequency up to 500 GHz was evaluated as shown in the figure 4.10. Contribution of non-TEM mode propagation was evaluated by comparing the values between with and without transformation of ε_{eff} in the equation (33). The others uncertainty contributors were evaluated by using the Electro-Magnetic (EM) simulation and changing the parameter for calculation of ε_r and $\tan\delta$ in the analysis program. Thereafter, larger variation between both of the methods was adopted as the estimated uncertainty, because inaccurate simulation model can underestimate uncertainty contribution in the former case, and some parameters which are not included in the calculation, such as a length of the line, cannot be evaluated in the latter case. EM simulator femtet (murata software) was used for the investigation. Each sensitivity coefficient of the contributor $u_{A,i}$ (A is ε_r or $\tan\delta$) was calculated by the equations (43), where max(A) means maximum value, min(A) means minimum value, and Δx_i means estimated variation range. D_i is a divisor which was $\sqrt{3}$ excepting the accuracy of CDR by assuming a rectangular distribution. For accuracy of CDR, D_i was set as $\sqrt{6}$ because a triangle distribution can be assumed. Combined uncertainty was calculated by taking square-root of sum of squares of every contribution as equation (45). A coverage factor of combined uncertainty k was 2, which is corresponded to 95 % confidence limit.

$$u_{A,i} = \frac{\max(A_i)-\min(A_i)}{D\Delta x_i} \qquad (43)$$

$$U_{A,i} = u_{A,i}\Delta x_i \qquad (44)$$

$$U_A = k \times \sqrt{\sum_i (U_{A,i}^2)} \qquad (45)$$

Variation of each contributor (Δx_i) was determined according to the limitation in accuracy of circuit fabrication. Measurement repeatability was defined as a standard deviation in 4 of the measurements.

At 50 GHz, thickness of metallization causes a dominant impact to ε_r. On the other hand, surface roughness causes a dominant impact to evaluated $\tan\delta$. This is reasonable because thickness of metallization relates to distribution of the EM field, and surface roughness relates to conductivity of the metallization. At 270 GHz, non-TEM mode signal propagation becomes larger for ε_r, and accuracy of the CDR becomes a dominant contributor for $\tan\delta$. Since f_{g1} in the equation (33) is 188 GHz in this time, it is reasonable that impact of non-TEM mode signal propagation becomes larger at 270 GHz than that of 50 GHz. In addition, since accuracy of CDR is transfer to the evaluated $\tan\delta$ in the proposed technique, it is also reasonable that impact of accuracy of CDR becomes larger when measurement frequency becomes far from 30 GHz. It is noted that impact of surface roughness for $\tan\delta$ become smaller at 270 GHz. Combined uncertainties were calculated as 0.43 and 0.58 for ε_r, and 5.9×10^{-3} and 3.6×10^{-3} for $\tan\delta$ at 50 GHz and 270 GHz, respectively.

Table 4.2 Uncertainty contributions for ε_r.

Contributors	Variations $x_i \pm \Delta x_i/2$	$u_{\varepsilon r,i}$ 50 GHz	$u_{\varepsilon r,i}$ 270 GHz
Characteristic impedance	$50 \pm 2\ \Omega$	6.3×10^{-2}	1.1×10^{-2}
Thickness of substrate	$250 \pm 25\ \mu m$	1.8×10^{-2}	1.0×10^{-2}
Length of the line	$3.5 \pm 0.005\ mm$	1.6×10^{-3}	3.1×10^{-2}
Surface roughness	$0.1 \pm 0.1\ \mu m$	1.4×10^{-1}	3.3×10^{-2}
Conductivity of metal	$94 \pm 6\ \%$	4.7×10^{-2}	1.1×10^{-2}
Thickness of metallization	$2 \pm 1\ \mu m$	**1.5×10^{-1}**	**1.8×10^{-1}**
Measurement repeatability	N=4	5.7×10^{-2}	1.4×10^{-1}
Non-TEM mode propagation		9.6×10^{-3}	1.7×10^{-1}
Combined uncertainty	k=2	4.3×10^{-1}	5.8×10^{-1}

Table 4.3 Uncertainty contributions for tanδ.

Contributors	Variations $x_i \pm \Delta x_i/2$	$u_{\tan\delta,i}$ 50 GHz	$u_{\tan\delta,i}$ 270 GHz
Characteristic impedance	$50 \pm 2\ \Omega$	2.7×10^{-4}	3.6×10^{-4}
Thickness of substrate	$250 \pm 25\ \mu m$	1.8×10^{-4}	1.0×10^{-4}
Length of the line	$3.5 \pm 0.005\ mm$	5.9×10^{-7}	5.0×10^{-4}
Surface roughness	$0.1 \pm 0.1\ \mu m$	$\mathbf{1.4 \times 10^{-3}}$	6.7×10^{-4}
Conductivity of metal	$94 \pm 6\ \%$	1.0×10^{-3}	2.3×10^{-4}
Thickness of metallization	$2 \pm 1\ \mu m$	3.4×10^{-4}	3.6×10^{-4}
Measurement repeatability	N=4	5.0×10^{-4}	6.3×10^{-4}
Non-TEM mode propagation		3.3×10^{-5}	5.8×10^{-4}
Frequency dependence of Q_{c0}		1.1×10^{-6}	1.4×10^{-5}
Accuracy of the CDR		5.7×10^{-4}	$\mathbf{1.1 \times 10^{-3}}$
Combined uncertainty	k=2	5.9×10^{-3}	3.6×10^{-3}

4.4.3 Broadband dielectric measurement

Figure 4.11(a) shows the broadband dielectric permittivity spectra. The data denoted as "Disk resonator" is quoted from reference 52, and the data denoted as "THz-TDS" is quoted from references 59 and 60. The error bars indicate the range of uncertainty. As shown in the figure, the dielectric permittivity evaluated by the circular-disk resonator and PBR technique exhibit good agreement, despite the difference in the measurement methods. Furthermore, the "This work" plots exhibit continuity to the "THz-TDS" reference values. Figure 4.11(b) shows the dielectric loss tangent. The dielectric loss tangent also shows discontinuity with the values evaluated by THz-TDS. Dielectric dispersion due to the phonon of alumina was calculated by using the equations (46) and (47) with the phonon parameters in the Table 4.4, which are quoted from the reference 60.

$$\varepsilon^* = \varepsilon_\infty + \varepsilon_{phonon} \qquad (46)$$

$$\varepsilon_{phonon} = \sum_{i=1}^{n} \frac{\Delta\varepsilon_i \omega_i^2}{\omega_i^2 - \omega^2 - j\omega\gamma_i} \qquad (47)$$

The solid curves in the figure 4.11 indicate calculated dielectric dispersion of the phonon model. As shown in the figure, evaluated ε_r and $\tan\delta$ were corresponded to those of calculated from the dispersion model within the uncertainty range. It is therefore, accuracy of the PBR method was validated by the dispersion model of the alumina substrate. On the other hand, broken curves in the figure 4.11 shows dielectric dispersion due to the phonon and Cole-Cole relaxation model calculated by the equations (48) and (49). Parameters for Cole-Cole relaxation model are shown in the Table 4.5.

$$\varepsilon^* = \varepsilon_\infty + \varepsilon_{debye} + \varepsilon_{phonon} \qquad (48)$$

$$\varepsilon_{debye} = \frac{\varepsilon_s}{1+(j\omega\tau)^\beta} \qquad (49)$$

The broken curve of ε_r was corresponded to the all plots, but that of $\tan\delta$ was deviated from the plots of the PBR method. However, dispersion factor β was 0.1, which was extremely small value. According to this model, lots of dipole-moments should be existed in broadly distributed frequency domain. This dispersion model is not substantial for alumina. It is therefore, the dispersion model only with the phonon mode, was considered as a substantial model in this case. As a conclusion, the PBR method was demonstrated at the mmW frequencies and accuracy of the measurement was discussed. Dielectric dispersion model of alumina substrate was discussed with the broadband frequency range in this paper. This indicates that the potential of the PBR method to adopt for investigation on dielectric property in the mmW-frequencies. The PBR method is expected as an effective technique for development of 6G communication technologies.

Table 4.4 Parameter of phonon modes of Alumina substrate. [60]

Resonant frequency ω_i (cm^{-1})	Oscillator Strength $\Delta\varepsilon_i$	Damping Coefficient γ_i (cm^{-1})

385	0.25	4.1
405	0.63	16.6
435	2.73	4.0
495	0.05	10.9
573	2.60	14.2
633	0.11	7.0
769	0.07	143.6

Table 4.5 Parameter of Cole-Cole relaxation.

β	τ (sec)	ε_s
0.1	1×10^{-11}	0.6

4.5   Conclusion of chapter 4

The PBR method was demonstrated in the frequency range up to 300 GHz in this chapter. It is noted that the precision probing technique is essential for improving measurement repeatability of the PBR method. The dielectric permittivity and loss tangent obtained by the PBR method exhibited good agreement with the other dielectric measurement techniques below 100 GHz. Furthermore, the evaluated permittivity exhibited reasonable continuity till sub-mmW frequencies, which can be explained by the dielectric dispersion of the phonon mode. This result validates the accuracy of the PBR method. The PBR method is expected to be an important tool for material characterization even in the frequency range up to 300 GHz.

4.6   References

[117]   W. Heinrich, "Quasi-TEM description of MMIC coplanar lines including conductor-loss effects," IEEE Trans. Microw. Theo. Technol., 41 1, pp.45-52, 1993.

[118]   W. Heinrich, "Full-wave analysis of conductor losses on MMIC transmisison lines," IEEE Trans. Microw. Theo. Technol., 38 10, pp.1468-1472, 1990.

[119]   W. Heinrich, "Conductor loss on transmission lines in monolithic microwave and millimeter-wave integrated circuits," Int. J. Microw. And millimeter-wave computer-aided Eng., 2 3, pp.155-167, 1992.

[120]   M. Y. Frankel, S. Gupta, J. A. Valdmanis, and G.A. Mourou, IEEE Trans. Microw. Theo. Technol., 39 6, pp.910-916, 1991.

[121]   F. Schnieder, T. Tischler, and W. Heinrich,"Modeling dispersion and radiation characteristics of conductor-backed CPW with finite ground width," IEEE Trans. Microw. Theo. Technol., 51 1, pp.137-143, 2003.

[122]   G. Gold, and K. Helmreich, "A Physical Surface Roughness Model and Its Applications," IEEE Trans. Microw. Theo. Technol., 65 10, pp.3720-3732, 2017.

[123]   W. Heinrich, F. Schnieder, and T. Tischler, "Dispersion and radiation characteristics of conductor-backed CPW with finite ground width," IEEE MTT-S Dig., TH3E-1, 2000.

[124]   T. K. Johansen, C. Jiang, D. Hadziabdic, and V. Krozer, "EM simulation accuracy enhancement for broadband modeling of on-wafer passive components," Proc. 2nd EuMIC Conf. Dig., pp.447-450, (2007).

(a)

Input   Output

L_{notch} Destructive
                interaction

(b)

S_{21}

f_r f

Resonator   GSG probe tips

L_p

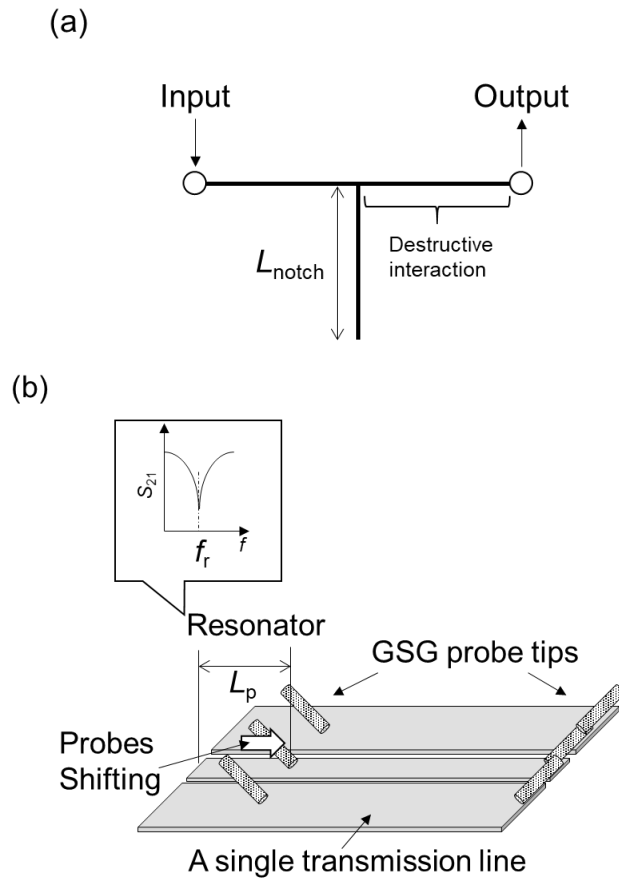Probes
Shifting

A single transmission line

Figure 4.1   Illustrations of the PBR method. (a) Equivalent circuit of the
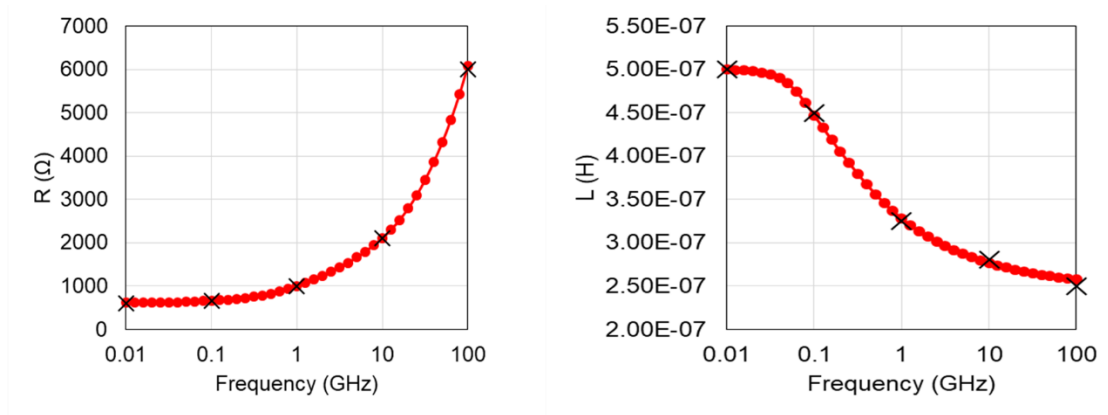measurement, and (b) the measurement principle.

Figure 4.2 Resistance and inductance of a transmission line by the transmission line theory. Cross marks indicate the values from the reference, and red-colored plots and curve indicates calculated value in this thesis.

$$Q_L = \frac{\omega L}{R}$$

$$Q_C = \frac{\omega C}{G}$$
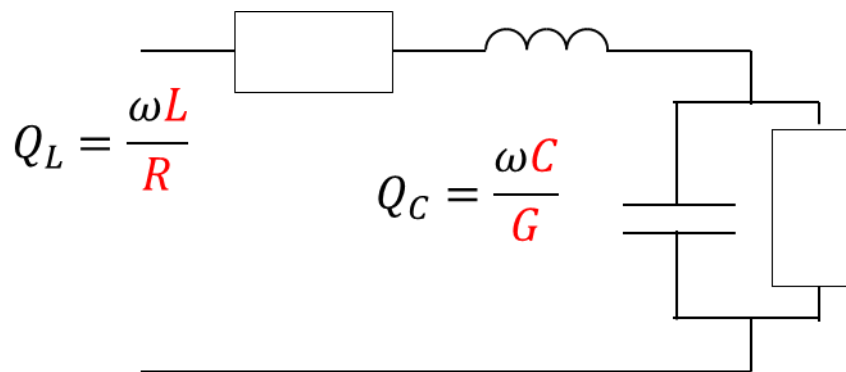
Figure 4.3   Equivalent circuit of the ideal resonator.

Q_{Co}

$$Q_L = \frac{\omega L}{R}$$

$$Q_C = \frac{\omega C}{G}$$

Ideal resonator   Open end of the line
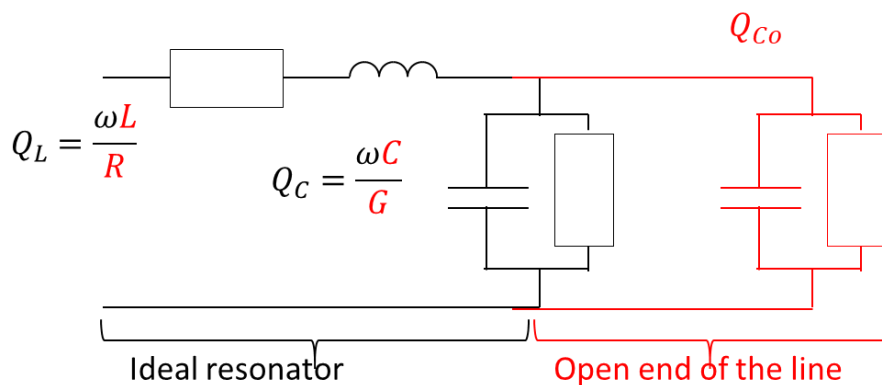
Figure 4.4 Modified equivalent circuit. An open end the line was additionally modeled compares to the figure 4.2.
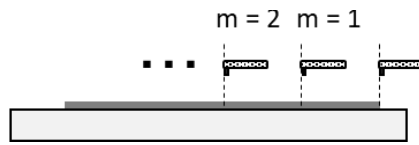
Figure 4.5   Illustrations of probing procedure of the dielectric measurement.
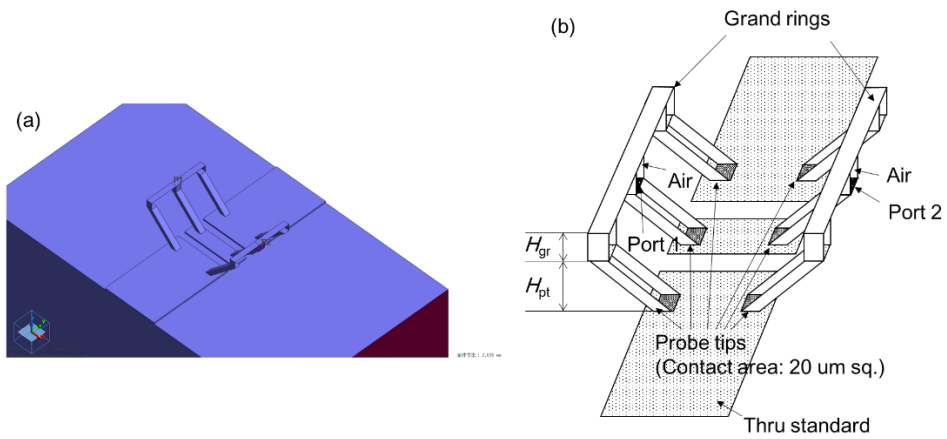

Figure 4.6   Model of the probe and transmission line for EM simulation. (a) Overview the model, and (b) a schematic illustration of the model of probe tips.
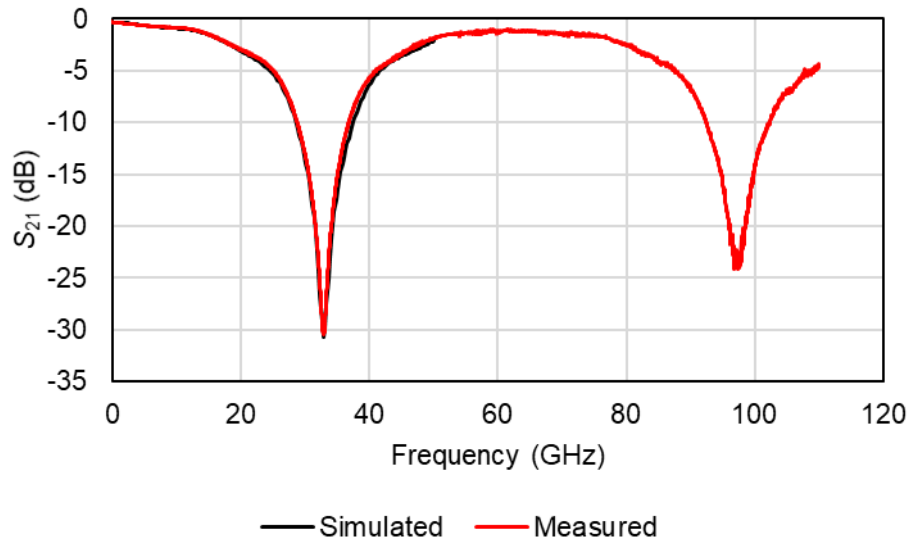
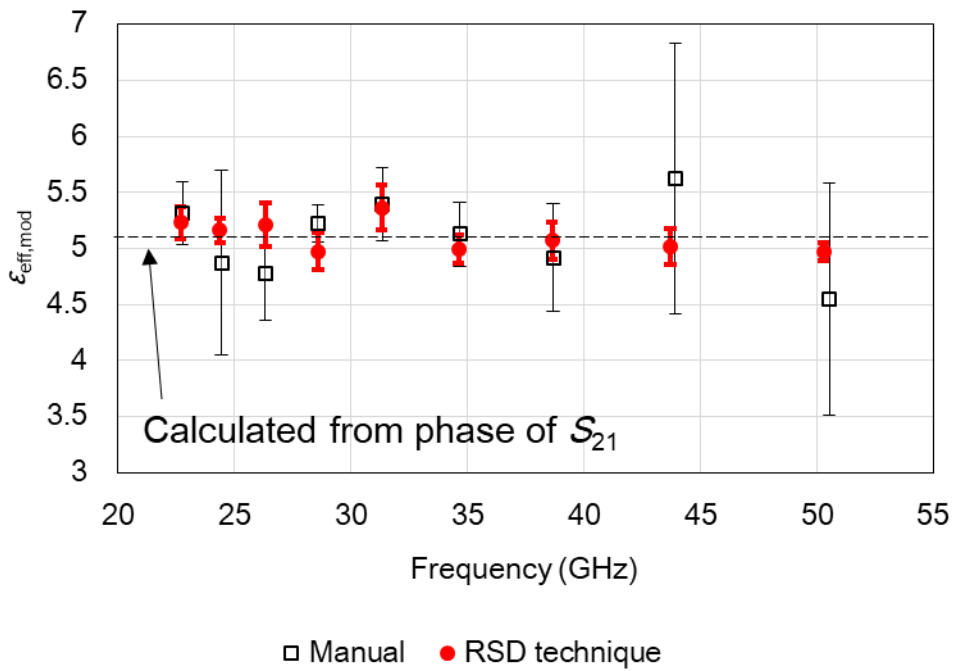Figure 4.7   Measured- and simulated- traces of S-parameter.

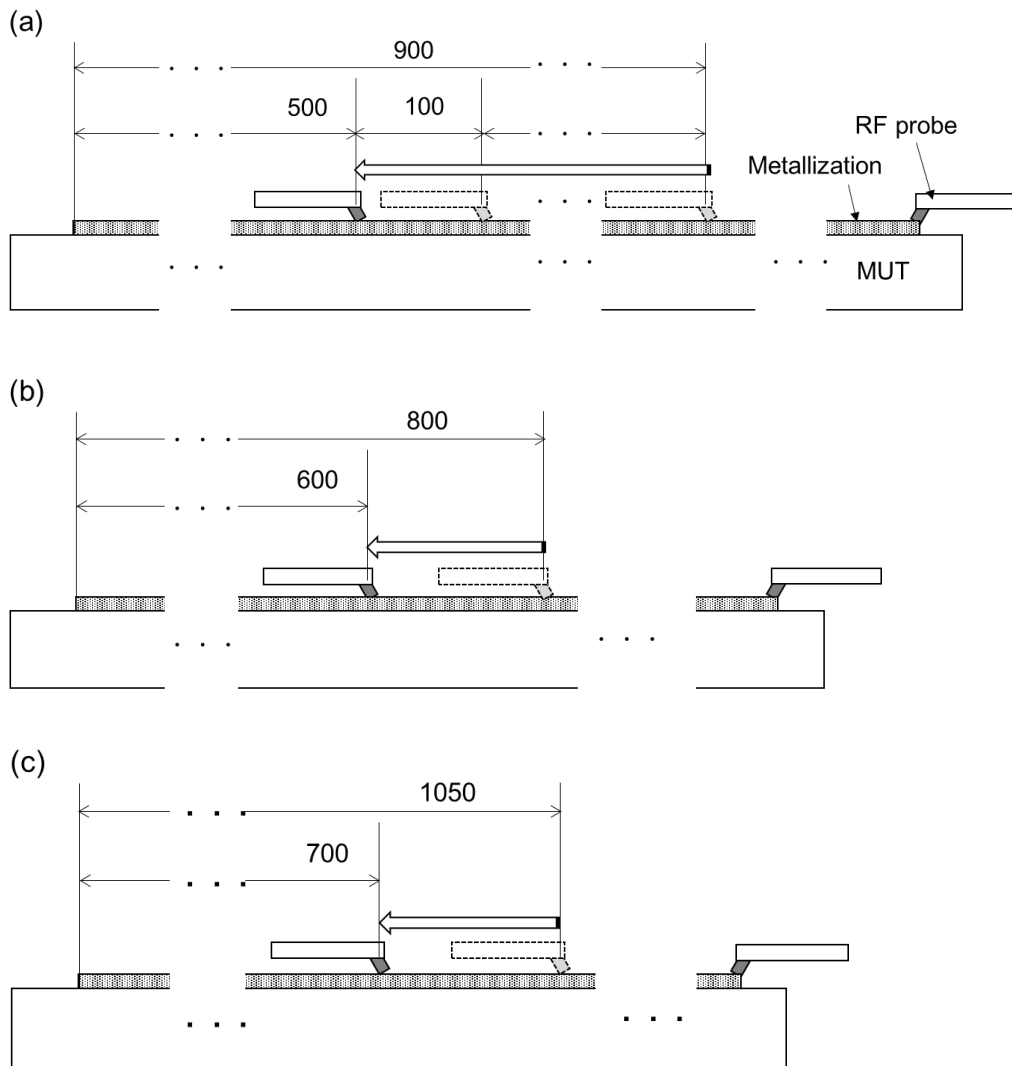Figure 4.8 Evaluated dielectric permittivity with the conventional and the proposed techniques.

(a)

900

500 100

RF probe

Metallization

MUT

(b)

800

600

(c)

1050

700

Figure 4.9 Modified equivalent circuit. An open end the line was additionally modeled compares to the figure 4.2.
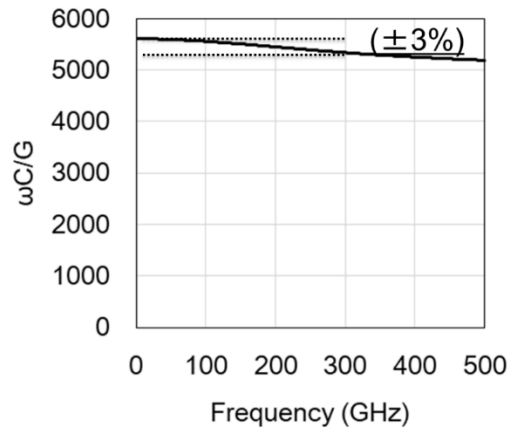
Figure 4.10   Estimated Qc_0 spectra in the frequency range up to 500 GHz.
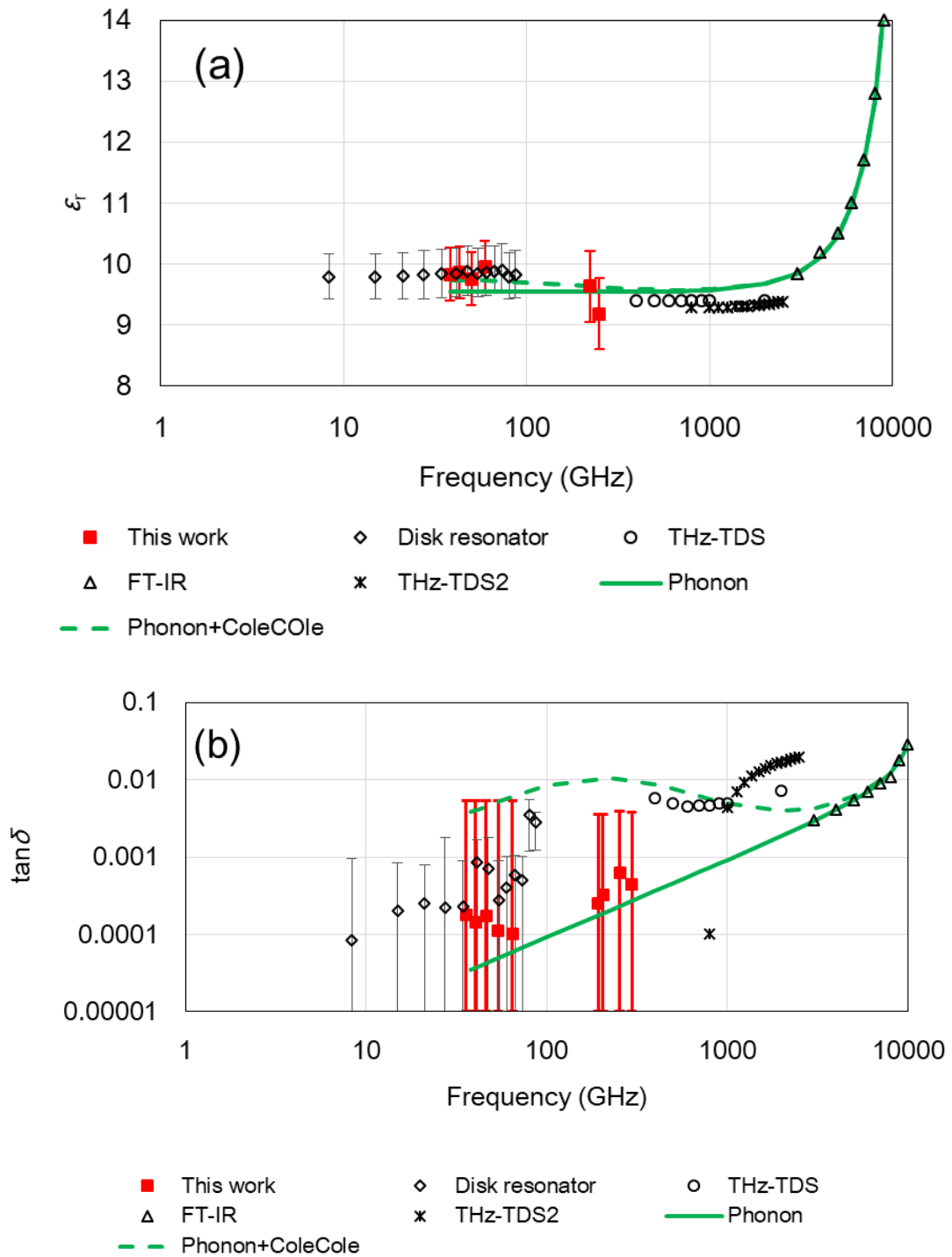
Figure 4.11　Broadband dielectric properties evaluated by several dielectric measurement methods. (a) Dielectric permittivity and (b) dielectric loss.

Chapter 5   In-situ effective dielectric permittivity measurement of transmission line

5.1   Introduction of chapter 5

"In-situ" dielectric permittivity measurement by the PBR method is demonstrated in the frequency range up to 110 GHz in this chapter. Attenuator and mismatched transmission line were used for the demonstration. The detail of the technique is provided in "Paper VI: Jap. J. Appl. Phys., 57, 11UE01 (2018)" and "Conference paper VII: IFAAP 2018, (2018) [Awarded]".

5.2   Measurement principle of probe-backside reflection method

Figure 5.1 (same with Figure 4.1(b)) shows a schematic illustration of the principle of the proposed technique. As described in the Chapter 4, the proposed technique utilizes two of the measurements, and take difference between the measurements. Effective dielectric permittivity can be calculated by using the equations (1) – (4).

$$\lambda_{\mathrm{r,eval,m}} = \frac{c_0}{f_{\mathrm{r,eval,m}}} \tag{1}$$

$$L_{\mathrm{e,eval,m}} = \frac{2n-1}{4} \lambda_{\mathrm{r,eval,m}} \tag{2}$$

$$\varepsilon_{\mathrm{eff,mod}} = \left(\frac{L_{\mathrm{e,m+1}} - L_{\mathrm{e,m}}}{L_{\mathrm{p,m+1}} - L_{\mathrm{p,m}}} \right)^2 = \left(\frac{\Delta L_{\mathrm{e,eval,m}}}{\Delta L_{\mathrm{p,m}}} \right)^2 \tag{3}$$

$$f_{\mathrm{r,m}} = \frac{f_{\mathrm{r,eval,m+1}} + f_{\mathrm{r,eval,m}}}{2} \tag{4}$$

5.3   Methodology of demonstration

5.3.1   Measurement system and configurations

The dielectric measurement technique was demonstrated in the "100-GHz band" in this chapter. Table 5.1 shows the configurations of the measurement systems. The original probe station from Chapter 2 were used for the demonstration. The substrate material of the ISS was alumina ceramics with the nominal dielectric permittivity of 9.8. Furthermore, the precision probing technique described in Chapter 4, was used to improve measurement repeatability.

Table 5.1 System configurations

Frequency band	100 GHz
Measurement frequency	10 MHz-110 GHz
VNA	E8361A
Extender	N5250A
IF (Hz)	100
Probe	Infinity-GSG-150
ISS	101-190

5.3.2   In-situ dielectric measurement by using actual common attenuator

As described in the Chapter 4, the proposed technique does not require to use any resonator, but it generates the quasi-resonator on a normal transmission line. It is therefore the technique should work not only for transmission line, but also for an attenuator. In this time, a 6-dB attenuator and matched transmission line on the same alumina substrate was used for the validation. Originally, the devices were fabricated as verification devices to check accuracy of on-wafer measurement system [125]. Figure 5.2 shows images of both devices. The length of transmission line was 2 mm. the

attenuator was designed theoretically based on T-type attenuator. The dielectric measurement was executed by using the feedline of the attenuator and the transmission line. Since length of the feedline of attenuators was only 500 μm, comparison of dielectric permittivity was executed by shifting the probe from 350 μm to 500 μm. The permittivity was evaluated at 70 GHz in this case.

5.4   Comparison of effective dielectric permittivity

Figure 5.3 shows the comparison of the effective dielectric permittivity measured using the matched transmission line and 6-dB attenuator. As shown in the figure, these dielectric permittivity values agree with each other. This result indicates that the proposed technique can be utilized even in an attenuator device. Therefore, the proposed technique has a great potential for in-situ dielectric measurements. The proposed technique provides breakthrough capabilities of dielectric property measurements of circuit substrates at mmW frequencies. The PBR method is expected as a powerful tool for investigation on local dielectric measurement in inhomogeneous material because the method works even on the actual on-wafer device without any resonator component.

5.5   Conclusion of Chapter 5

The in-situ effective dielectric permittivity of the transmission line and the attenuator was demonstrated in this chapter. The effective dielectric permittivity exhibited good agreement between the values obtained by using transmission line and attenuator. This result validates the accuracy of the PBR method for an effective dielectric permittivity measurement, which is insensitive to a used device. The PBR method can realize "in-situ" dielectric measurement without preparing specific device, because the method

doesn't require to fabricate any resonator in a device. This unique feature allows to investigate on inhomogeneity of substrate material just below actual devices.

5.6   Reference

[125]   R. Sakamaki, and M. Horibe, "Development of Verification Process for On-Wafer Measurement at Millimeter-Wave Frequencyn," CPEM 2016 Conf. Dig., Ottawa, Jul. 2016.
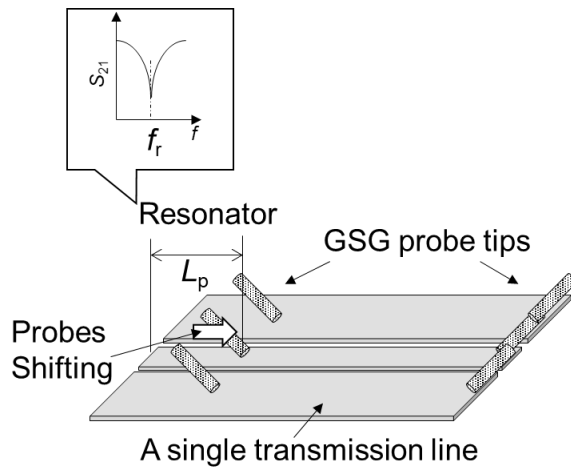
Figure 5.1   Illustrations of the measurement principle of PBR method. (Same with Figure 4.1(b))
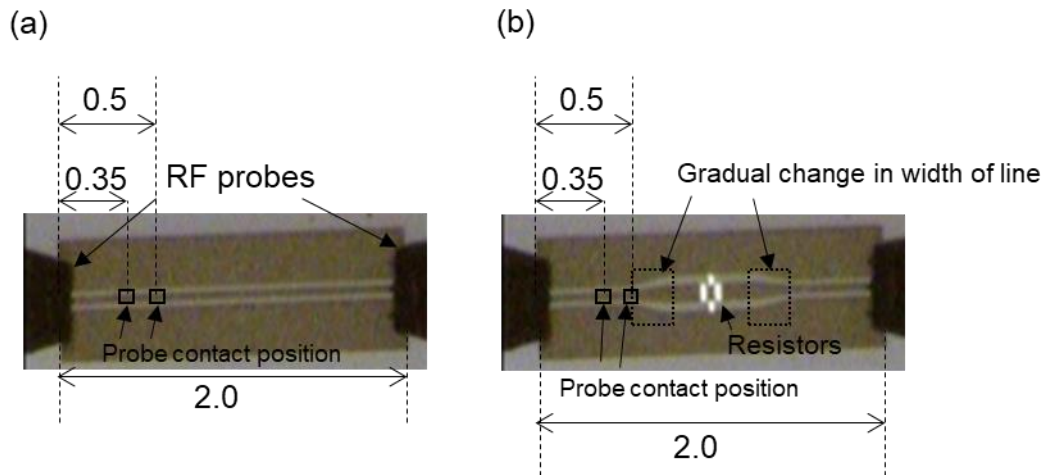

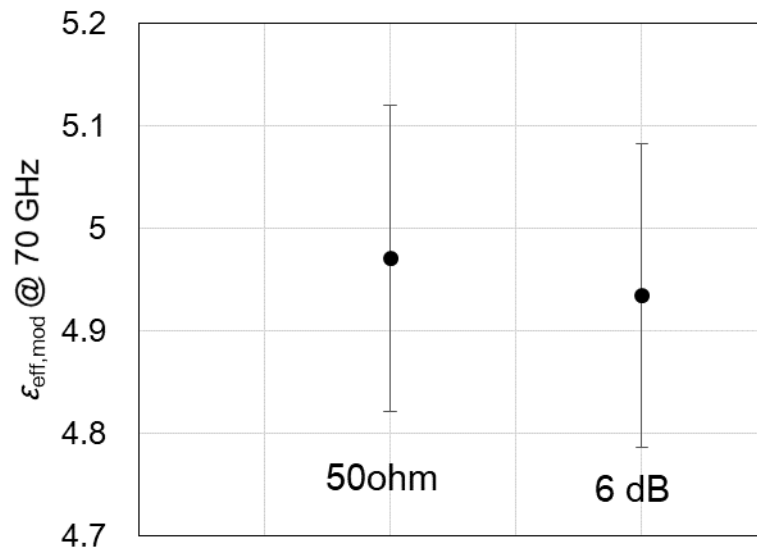Figure 5.2   Images of the devices. (a) 2mm-length transmission line, and (b) 6-dB attenuator.

Figure 5.3   Comparison of the effective dielectric permittivity measured by using the matched transmission line and the 6-dB attenuator.

Chapter 6   Progress of dielectric measurement technique for future communication technologies

6.1   Historical aspect of related technologies

6.1.1   Communication technologies

The world's first wireless communication technology is mechanical semaphore signal by telegraph developed in 18th century at France. At that time, the semaphore was communicated by direct observation using a telescope. In 19th century, Morse signal was developed by using electrical signal by wire communication. In 1923, Yagi-antenna have been developed. Thereafter, developments of wireless communication technologies are raced on. In the early days of the development, the wireless communications were limited in military uses. After the World War II, the wireless communications were used in marine vessels and automotive. A shoulder-phone was adopted for the phone in automotive. This shoulder-phone was primitive form of the today's mobile-phone. First PHS mobile communication became commercialized in 1995, which is referred as 1st generation communication today. After that, since communication signal was digitalized, E-mail and internet access can be realized by 2nd generation communication technologies. From 3rd generation communication technologies, international standardized organization of 3rd generation partnership project (3GPP) leads standardization of mobile communication system includes 5G communication technologies. IoT technologies was main frame of the 5G communication technologies. On the other hand, Internet of Human (IoH) and Internet of Ability (IoA) are put forward for 6G communication technologies. Main feature of the IoH and IoA is a communication of tactile sense. For instance, people can receive

lesson of professional pianist at far-off place by using high-speed communication and wearable devices. Thus, developments of wearable devices are also required for the improvement of 6G communication technologies. Sixth-generation communication technologies make people recognizing the thing exists on site by combining virtual reality technologies.

6.1.2 Transition of transmission line

In the past years, RF transmission lines are constructed by coaxial or waveguide structures. Thus, few material such as polyethylene was considered for construction of those transmission lines. However, requirements for miniaturization of electronics devices and improvement of fabrication technologies of thin-film lead use of planar-circuit as transmission line in 1950's. Variety of substrate materials, such as alumina, FR4, polytetrafluoroethylene, polyimide, SiO_2, Si, and glass-alumina, were adopted in nowadays. Use of planar-circuit leads diversity of material for the transmission line. Furthermore, as described in the previous chapters, operating frequency of the devices reaches to the mmW. Thus, wideband frequencies from high-frequency band to the mmW should be considered in this research field. It is therefore, knowledges of dielectric dispersion due to macro- and micro-structure of materials such as phonon vibration become essentials for design of transmission lines. Thus, both knowledges of material science and device engineering are required for development of transmission line and related technologies.

6.1.3 Transition of social requirements to science and technologies

Figure 6.1 shows relationship between operating frequency of the communication devices and years for starting development. The operating frequencies were drastically increased in recent several years, which may relate to growing in use of internet. Thus,

development speed is expected to be accelerated for catching up with it. However, resource for the development such as human-resource is limited. Therefore, ours society requires science researcher to comprehend more industrial needs of related technologies than ever before.

6.2   Contribution of this study

As described in the section 6.1.2, knowledge of dielectric dispersion mode is necessary for RF transmission line technologies. Direct measurement of dielectric properties is necessary to construct accurate model of the dielectric dispersion. However, the measurements in the mmW frequencies has a problem with regards to non-ideal electrical field distribution. As shown in Figure 6.2, electrical field is distributed in both of air and substrate for planar-circuits. Speed of transmitted electrical signal in air and substrate are different each other. To accommodate this difference, non-TEM mode signal have to propagate in the planar-circuit. Non-TEM mode signal propagation causes a transmission line theory more complex, because almost of the theories assumes single mode signal propagation. In this context, EM simulation is powerful tool to investigate non-TEM mode signal propagation. Actually, electrical behavior of planar-circuits can be estimated without detail knowledge with regards to the transmission line theories by using the EM simulation. However, in the 300 GHz band, requirement for accuracy of simulation model is extremely increased. This transition causes electrical properties of circuit difficult to be estimated even with the EM simulation. It is therefore, detail knowledge with regards to transmission line theories are required for this study. This study solved problems of material science by using the novel mmW and sub-mmW transmission line theories. Thus, this study can be positioned as a bridge between material science and device engineering. This study includes contents which belong to several academic fields, such as electronic

engineering, materials science, and metrology. The devices were designed by using transmission line theory from electronic engineering. Some knowledges from material science was used to analyze dielectric dispersion due to phonon of alumina substrate, and uncertainty analysis method belongs to metrology.

Two of major achievements of the study are proposal of the dielectric measurement in the 300 GHz band, and effective dielectric permittivity measurement of a transmission line of actual devices. Former achievement provides more accurate dielectric property data in the 300 GHz band. This improvement can accelerate speed of RF device development. Latter achievement can realize investigation on difference in transmission line properties due to fabrication process. Furthermore, this study is a bridge of several research fields. A bridge work can encourage to understand wider research back ground, and industrial needs of related technologies. For instance, this study may lead material scientist understand requirements of mmW devices. Thus, it is expected to accelerate development speed of mmW devices.

6.3   Future works

This study realizes dielectric measurement in the 300 GHz band, which is frequencies range where optimal dielectric measurement method is not exist. Thus, a broadband dielectric measurement can be realized by using the RSD method, and others methods such as FT-IR, THz-TDS, and AC parallel capacitance method. The broadband dielectric measurement is powerful tool for investigating dielectric dispersion modeling such as phonon vibration and Debye relaxations, which is essential for transmission line design as described in the section 6.1.2.

6.4   Conclusion

Requirements of high-speed communication and lack of frequencies resources cause the operating frequencies of RF communication devices reach to millimeter-wave frequencies. Note that discussion about "Beyond-5G" communication technology has been started and the operating frequencies up to 340 GHz are considered as candidates of target frequencies. Dielectric permittivity of a ceramic substrate is important information for circuit design. However, dielectric measurement at mmW frequencies has some problems as follow:

1) Since conventional low-loss dielectric measurement technologies are based on resonator-method, accuracy of mechanical working of a resonator limits range of measurement frequency. It becomes programmatic especially at mmW frequencies range of 100-300 GHz.

2) Conventional measurement techniques assume a homogeneous material. Thus, inhomogeneity of substrate cannot be investigated in the mmW. Inhomogeneity of substrate causes harmful impacts to reliability of RF devices. Thus, in-situ dielectric measurement technique is required to address the problem in the mmW.

This study addressed the problems described above. The combination of the PBR method and the precision probing technique realized material characterization in the frequencies ranging up to 300 GHz, because accuracy in size of the resonator can be determined by the accuracy in probe positioner in the PBR method. Further, since the PBR method does not require DUT having any resonator, it can be applied to common feedline of RF devices. Thus, the measurement can be demonstrated even with the attenuator. The PBR method can realized in-situ measurement. This unique feature realizes to investigate on inhomogeneity of substrate material just below actual RF

device. Thus, the in-situ measurement technique is considered as a useful tool for circuit testing process for circuit fabricators.

As described above, the proposed techniques can address the problems. Thus, they are considered to be powerful tools for development of millimeter-wave devices, which are essential technologies for realization of "Beyong-5G" communication technologies.
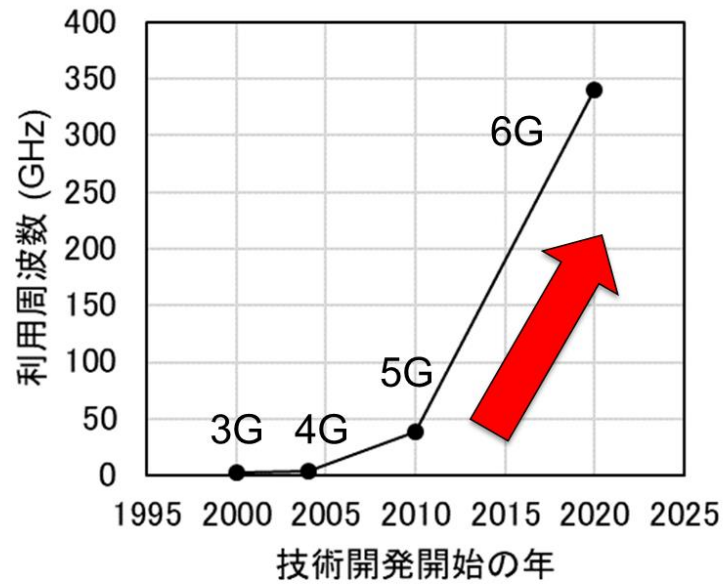
Figure 6.1   Relationship between operating frequencies and years for starting
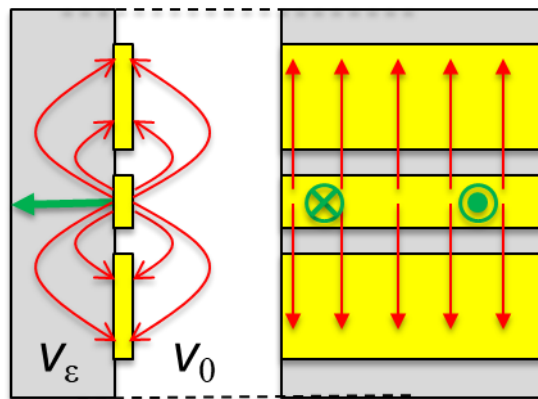development of the communication technologies.

Figure 6.2   Electrical field distributions of coplanar-wave guide.

Chapter 7   Summary

The new dielectric measurement technique was developed to address following two present problems of conventional technique.

1) Since conventional low-loss dielectric measurement technologies are based on resonator-method, accuracy of mechanical working of a resonator limits range of measurement frequency. It becomes programmatic especially at mmW frequencies range of 100-300 GHz.

2) Conventional measurement techniques assume a homogeneous material. Thus, inhomogeneity of substrate cannot be investigated in the mmW. Inhomogeneity of substrate causes harmful impacts to reliability of RF devices. Thus, in-situ dielectric measurement technique is required to address the problem in the mmW.

The problems above are obstacles for development of "Beyond-5G" communication technologies of which the operating frequencies up to 340 GHz are considered to be assigned.

The proposed measurement technique utilizes on-wafer measurement system to contact a probe at the middle of transmission line. Thus, impact of probe positioning should be investigated to establish the measurement technique. Main achievements of the study are summarized below:

1) The precision probing technique was developed to minimize variation in probe position in on-wafer measurement. The variation was reduced to 1 μm, which reaches 10 μm in the conventional technique.

2) The precision probing technique was demonstrated with various devices, such as the attenuator and the screen-printed transmission line. Measurement repeatability was greatly improved by using the precision probing technique in the all of measurements.

3) Material characterization was demonstrated by the proposed PBR method. Further, accuracy of the measurement was investigated. The evaluated results exhibited good correspondence to dielectric dispersion estimated from conventional phonon mode model.

4) Effective dielectric permittivity measurement was demonstrated by using the attenuator device, which does not have any resonator structure. The evaluated effective permittivity was corresponded to value derived from matched transmission line.

5) Measurement uncertainty analysis algorithm was developed to investigate on impact of probe positioning to dielectric measurement. The analysis result shows that accuracy of the positioning is a dominant uncertainty contributor in the ε_r measurement, but dimension of CPW was still dominant for $\tan\delta$ measurement.

Supplemental   TRL calibration

Detail of TRL calibration algorithm is described as follow:

As described in the chapter 2, TRL calibration requires 3 of calibration standards. Each calibration result can be expressed by the equations, where T_{Mi} means measured T-parameter, and T_{Ai} means actual T-parameter of the standards (i=1,2,3).

$$T_{M1} = T_X T_{A1} T_Y \qquad (S\text{-}1)$$

$$T_{M2} = T_X T_{A2} T_Y \qquad (S\text{-}2)$$

$$T_{M3} = T_X T_{A3} T_Y \qquad (S\text{-}3)$$

Asign THRU, LINE, and REFLECT standards to A1, A2, and A3, respectively. Then,

$$S_{thru} = \begin{bmatrix} 0 & 1 \\ 1 & 0 \end{bmatrix}, \quad T_{thru} = T_{A1} = \begin{bmatrix} 1 & 0 \\ 0 & 1 \end{bmatrix} \qquad (S\text{-}4)$$

$$S_{line} = \begin{bmatrix} 0 & e^{\gamma l_2} \\ e^{\gamma l_2} & 0 \end{bmatrix}, \quad T_{line} = T_{A2} = \begin{bmatrix} e^{-\gamma l_2} & 0 \\ 0 & e^{\gamma l_2} \end{bmatrix} \qquad (S\text{-}5)$$

$$\Gamma_{reflect} = 1 \qquad (S\text{-}6)$$

From the equations (S-1) and (S-2),

$$\left(T_{M2} T_{M1}^{-1}\right) T_X = T_X \left(T_{A2} T_{A1}^{-1}\right) \qquad (S\text{-}7)$$

Assuming:

$$M_A = T_{M2} T_{M1}^{-1} \qquad (S\text{-}8)$$

$$C_A = T_{A2} T_{A1}^{-1} \qquad (S\text{-}9)$$

Then, the equation (S-7) can be rewritten as:

$$M_A T_X = T_X C_A \qquad (S\text{-}10)$$

Assuming:

$$M_A = \begin{bmatrix} m_{11} & m_{12} \\ m_{21} & m_{22} \end{bmatrix}、\ T_X = \begin{bmatrix} x_{11} & x_{12} \\ x_{21} & x_{22} \end{bmatrix} \tag{S-11}$$

$$C_A = \begin{bmatrix} \dfrac{T_{A2,11}}{T_{A1,11}} & 0 \\ 0 & \dfrac{T_{A2,22}}{T_{A1,22}} \end{bmatrix} \tag{S-12}$$

Substitute (S-11) and (S-12) to (S-10), and erase $\dfrac{T_{A2,11}}{T_{A1,11}}$ and $\dfrac{T_{A2,22}}{T_{A1,22}}$ then,

$$m_{21}\left(\frac{x_{11}}{x_{21}}\right)^2 + (m_{22} - m_{11})\left(\frac{x_{11}}{x_{21}}\right) - m_{12} = 0 \tag{S-13}$$

$$m_{21}\left(\frac{x_{12}}{x_{22}}\right)^2 + (m_{22} - m_{11})\left(\frac{x_{12}}{x_{22}}\right) - m_{12} = 0 \tag{S-14}$$

These equations give same solutions. The solutions $\dfrac{x_{11}}{x_{12}}$ and $\dfrac{x_{21}}{x_{22}}$ are expressed

as:

$$\left(\frac{x_{11}}{x_{21}}\right) = a = \frac{-\Delta x}{-e_{11}} = e_{00} - \frac{e_{10}e_{01}}{e_{11}} \tag{S-15}$$

$$\left(\frac{x_{12}}{x_{22}}\right) = b = e_{00} \tag{S-16}$$

Generally, a > b in normal reflectometer. Thus,

$$\frac{x_{11}}{x_{12}} = a = \frac{-(m_{22} - m_{11}) + \sqrt{(m_{22} - m_{11})^2 + 4m_{21}m_{12}}}{2m_{21}} = e_{00} - \frac{e_{10}e_{01}}{e_{11}} \tag{S-17}$$

$$\frac{x_{12}}{x_{22}} = b = \frac{-(m_{22} - m_{11}) - \sqrt{(m_{22} - m_{11})^2 + 4m_{21}m_{12}}}{2m_{21}} = e_{00} \tag{S-18}$$

In same manner with the above, the error box *Y* also calculated as follow:

$$T_Y\left(T_{M1}^{-1}T_{M2}\right) = \left(T_{A1}^{-1}T_{A2}\right)T_Y \tag{S-19}$$

$$M'_A = T_{M1}^{-1}T_{M2} \tag{S-20}$$

$$C'_A = T_{A1}^{-1} T_{A2} \tag{S-21}$$

$$T_Y M'_A = C'_A T_Y \tag{S-22}$$

$$M'_A = \begin{bmatrix} m'_{11} & m'_{12} \\ m'_{21} & m'_{22} \end{bmatrix}, \quad T_Y = \begin{bmatrix} y_{11} & y_{12} \\ y_{21} & y_{22} \end{bmatrix} \tag{S-23}$$

$$C_A = \begin{bmatrix} \dfrac{T_{A2,11}}{T_{A1,11}} & 0 \\ 0 & \dfrac{T_{A2,22}}{T_{A1,22}} \end{bmatrix} \tag{S-24}$$

$$m'_{21}\left(\frac{y_{11}}{y_{21}}\right)^2 + \left(m'_{22} - m'_{11}\right)\left(\frac{y_{11}}{y_{12}}\right) - m'_{12} = 0 \tag{S-25}$$

$$m'_{21}\left(\frac{y_{21}}{y_{22}}\right)^2 + \left(m'_{22} - m'_{11}\right)\left(\frac{y_{21}}{y_{22}}\right) - m'_{12} = 0 \tag{S-26}$$

$$\left(\frac{y_{11}}{y_{12}}\right) = c$$
$$= \frac{-\Delta y}{e_{22}} = \frac{-\left(m'_{22} - m'_{11}\right) + \sqrt{\left(m'_{22} - m'_{11}\right)^2 + 4m'_{21} m'_{12}}}{2m'_{21}}$$
$$= \frac{e_{32} e_{23}}{e_{22}} - e_{33} \tag{S-27}$$

$$\left(\frac{y_{21}}{y_{22}}\right) = d$$
$$= \frac{-\left(m'_{22} - m'_{11}\right) - \sqrt{\left(m'_{22} - m'_{11}\right)^2 + 4m'_{21} m'_{12}}}{2m'_{21}} = -e_{33} \tag{S-28}$$

Next, executing reflect standards measurement at both ports.

$$\Gamma_3 = \frac{1}{e_{11}} \frac{b - \Gamma_{mx}}{a - \Gamma_{mx}} \tag{S-29}$$

$$\Gamma_3 = \frac{1}{e_{22}} \frac{d - \Gamma_{my}}{c - \Gamma_{my}} \tag{S-30}$$

Erase Γ_3 from the equations (S-29) and (S-30) then,

$$e_{22} = \frac{e^{2\gamma l_1}}{e_{11}} \frac{b - S_{11m}}{a - S_{11m}} \tag{S-31}$$

$$e_{11} = e^{\gamma l_1} \sqrt{\frac{b - \Gamma_{mx}}{a - \Gamma_{mx}} \frac{c + \Gamma_{my}}{d + \Gamma_{my}} \frac{b - S_{11m}}{a - S_{11m}}} \tag{S-32}$$

From the equation (S-27),

$$b - a = \frac{e_{10}e_{01}}{e_{11}} \tag{S-33}$$

$$c - d = \frac{e_{23}e_{32}}{e_{22}} \tag{S-34}$$

$$e_{10}e_{01} = e_{11}(b - a) \tag{S-35}$$

$$e_{23}e_{32} = e_{22}(c - d) \tag{S-36}$$

Here,

$$\gamma = j\beta = j\frac{2\pi}{\lambda} = j\frac{2\pi f}{c_0} \tag{S-37}$$

$$c - d = \frac{e_{23}e_{32}}{e_{22}} \tag{S-38}$$

Next, calculate $e_{10}e_{32}$ and $e_{23}e_{01}$ from a THRU standard measured results,

$$e_{10}e_{32} = S_{21m1}\left(1 - e_{11}e_{22}e^{-2\gamma l_1}\right)e^{\gamma l_1} \tag{S-39}$$

$$e_{23}e_{01} = S_{12m1}\left(1 - e_{11}e_{22}e^{-2\gamma l_1}\right)e^{\gamma l_1} \tag{S-40}$$

Finally, calculate T-parameter of DUT from the equation (13) in the chapter 2.

$$T_A = T_X^{-1}T_M T_Y^{-1} \tag{S-41}$$

Acknowledgements